THE UNIVERSITY OF CHICAGO

PROBING THE SPATIAL DISTRIBUTION OF ENTANGLEMENT IN MANY-BODY QUANTUM SYSTEMS

A DISSERTATION SUBMITTED TO
THE FACULTY OF THE DIVISION OF THE PHYSICAL SCIENCES
IN CANDIDACY FOR THE DEGREE OF
DOCTOR OF PHILOSOPHY

DEPARTMENT OF PHYSICS

BY
IAN MACCORMACK

CHICAGO, ILLINOIS
DECEMBER 2021

Dedicated to Papou

TABLE OF CONTENTS

LIST OF FIGURES

ACKNOWLEDGMENTS

First and foremost, I must thank my advisor Shinsei Ryu. I am extremely lucky to have found an advisor with such a breadth of interests and depth of knowledge so as to allow me to work on the variety of projects that I have. My gratitude extends further to his patience with my often scatterbrained ways of thinking and working. I would never have developed the ability to ask interesting research questions or appreciate the large body of work that I have without Shinsei as an advisor. I always walked away from our meetings brimming with enthusiasm for whatever project we were discussing.

I would also like to thank the current and former members of the Ryu research group. In particular Hassan Shapourian, Xueda Wen, Mao-Tian Tan, Jonah Kudler-Flam, Yuhan Liu, Laimei Nie, Anish Kulkarni, and Taozhi Guo. My other colleagues at the University of Chicago and elsewhere have also been a tremendous resource for learning and camaraderie: Kyle Kawagoe, Umang Mehta, Carolyn Zhang, Hart Goldman, Matt Dodelson, Paolo Glorioso, Matt Lapa, Luca Delacretaz, Harvey Hsiao, Gautam Satishchandran, Christian Ferko, Aurora Ireland, Professor Wendy Zhang. Thank you for being my peers and mentors.

Other friends and collaborators to whom I owe a tremendous debt include Venkatesh Chandresakaran, who is not only a great friend, but always helped me chip away at my persistent imposter syndrome. I thank Pawel Caputa for taking interest in some of my early work and working with me to develop an interesting extension of it. I am also very grateful to Alexey Galda for guiding me through my foray into the brave new world of quantum computing, and producing some great work as a result. Alexey was also invaluable in my job search process, and I look forward to many more years of fruitful collaboration with him.

I must also thank the members of my PhD committee — Jeffrey Harvey, Mark Oreglia, and Michael Levin — for taking valuable hours out of their schedules to ensure I was on the right track. In particular I thank Michael Levin for sage advice and guidance at the very early stages of my graduate school experience.

Outside of the physics world, I thank the numerous friends I have connected with throughout my life for keeping me grounded and taking my mind away from science from time to time. Charley Binkow, Zach Kay, Andre Vasilyev, Andrew Meyer, Johnny Armstrong, Kate Redford, Steven Durr, Brian Shin, Aislyn Dirisio, Caleb Balbera, Ethan and Emma Arnault, and many others. Thank you very much.

Last but certainly not least, I thank my immediate and extended family for reminding me of the important things in life outside of physics. Though many people in my family never attended college and none of them work in the STEM fields, they never scoffed at or questioned my decision to spend half a decade getting a degree in theoretical physics. As alien of a proposition as a physics PhD is to many of them, they always supported me and gave me the confidence I needed to continue. Visits with my family, North and South, reminded me that I would have people to love me unconditionally even if I failed miserably. I love you all.

ABSTRACT

Entanglement is the most unique and distinguishing feature of quantum mechanics, and is of fundamental importance not only to the theory of quantum information, but to the study of quantum phases of matter. While much work has been done to study the entanglement in the ground states of familiar systems like conformal field theories and gapped topological phases, slightly less attention has been paid to dynamical quantum systems and systems that lack translational invariance.

In this thesis, I will first introduce some basic formalism and intuition related to entanglement in many-body quantum systems. I will then discuss an elegant means of calculating entanglement entropy and other measures in conformal field theories on curved backgrounds via the Ryu/Takyanagi formula. Next, I will introduce a general formula for the calculation of the entanglement contour, a well-behaved entanglement density function. We will show the contour to be particularly useful for probing the dynamics of out-of-equilibrium quantum systems. With these dynamical systems in mind, I will present results from calculations of multipartite operator entanglement — a state-independent entanglement measure — in a many-body localized system.

Finally, I will conclude with a description of a new method to simulate two dimensional tensor network states on a quantum computer, as a means of realizing entangled quantum matter in a controlled, experimental setting. I also include results from an experimental proof-of-concept of this method.

CHAPTER 1

ENTANGLEMENT IN MANY-BODY QUANTUM SYSTEMS

1.1 Introduction

Starting in the 1920's and 1930's when the concept of entanglement was first understood as a consequence of the newly developed formalism of quantum mechanics, it baffled and frustrated many of the original pioneers in the field. Since then, although many of the original concerns about "spooky action at a distance" have been addressed, entanglement remains one of the most unique and consequential aspects of the quantum world.

Though there is no universal scheme for classifying and quantifying entanglement in quantum systems with many particles, in recent years the limited tools we do have for understanding entanglement have become increasingly important for practitioners in the fields of quantum information, condensed-matter, and high energy physics alike. Entanglement has been used to detect topological order [5, 6], an intrinsically quantum phenomenon beyond the Landau paradigm of phase transitions [7]. Measures of mixed-state entanglement have been used to classify topological insulators [8]. Entanglement measures have also been important in the study of chaos, scrambling and thermalization in out-of-equilibrium quantum systems [9]. The connection of gravity and quantum field theory via the AdS/CFT correspondence [10] has also been deepened by the Ryu-Takayanagi formula [11, 12], which relates geometric surfaces in a gravitational theory to Von Neumann entropy in a corresponding conformal field theory. This is but a small sample of the vast literature that has sought to better understand many-body quantum systems and quantum field theories through the lens of entanglement.

The study of many-body entanglement has opened up and answered many interesting questions about how different entanglement measures behave in different quantum systems. At the same time, these efforts have motivated the development of novel measures of entanglement, which probe aspects of quantum correlation that the established quantities like Von Neumann entropy fail to capture. The work in this thesis reflects a broad interest in both aspects of the study of many-body entanglement. This thesis will study the behavior of conventional entanglement measures in systems where they have not been fully examined — in particular, systems that break translational symmetry either through quenched disorder or curved background geometry. Though these systems are typically still local, changes to their background geometry will prove to have dramatic, non-local effects on the spatial distribution of entanglement. This thesis will also introduce work that further develops novel probes of entanglement, applying them to various systems and attempting to interpret the results.

To this end, we begin in this chapter by presenting necessary formalism for describing quantum many-body systems and quantifying entanglement. We will then use machinery from the AdS/CFT correspondence — namely the Ryu-Takayanagi formula — to introduce an elegant, geometric method for calculating Von Neumann entropy and related quantities in strongly coupled conformal field theories on curved backgrounds. We will demonstrate the efficacy of the method, both at zero and finite temperatures, using several cases relevant to condensed matter physics, in particular the rainbow chain and the sine-square deformation, which both have spatial distributions of entanglement very different from that of a CFT on a flat background. Motivated by this, we then turn to the entanglement contour, a quasi-local measure of entanglement, which probes the spatial distribution of entanglement at a finer resolution than non-local quantities like the Von Neumann entropy. We show that a previously introduced formula for a holographic entanglement contour is actually a valid entanglement contour in any system. We then use this formula to probe the spread of entanglement after quantum quenches in a holographic CFT and in a many-body localized system (MBL). Maintaining an eye towards dynamical phases of quantum matter, we present background information and previous results on operator mutual information and negativity — state independent measures of information spreading for a given Hamiltonian. We then compute multipartite measures of operator entanglement in MBL, and find that the delocalization of quantum information is suppressed relative to the total spread of information, which is not the case in typical interacting systems. Finally, we ask about how entangled quantum matter can be simulated and probed using near-term quantum devices, and we develop a method for doing so in a resource-efficient manner for certain PEPs tensor network states. Though this final chapter does not deal directly in the calculation or development of measures of entanglement, it draws heavily on intuition about quantum correlations in tensor network states, and motivates future use of noisy intermediate scale quantum (NISQ) computers in the study of entanglement in many-body quantum systems.

1.2 Lattice Quantum Systems

The simplest systems we will consider in this thesis are discrete chains of N qudits or spins. In this case, the Hilbert space of the system is the tensor product of N local d-dimensional qudit Hilbert spaces:

$$\mathcal{H}_{chain} = \bigotimes_{i=1}^{N} \mathcal{H}_d. \tag{1.1}$$

Overall, the Hilbert space dimension is d^N. In the case of qubit/spin-$\frac{1}{2}$ systems, we have $d = 2$. For now, we will focus on the qubit case while defining and giving examples of necessary quantities.

Pure states — normalized vectors in $\mathcal{H}_{chain}$ — can be represented by a sum over tensor products of orthonormal basis vectors in each local Hilbert space. That is, if we have the basis vectors $\{|0\rangle, |1\rangle\} \in \mathcal{H}_d$, such that $\langle 0|0\rangle = \langle 1|1\rangle = 1$ and $\langle 0|1\rangle = \langle 1|0\rangle = 0$, orthonormal basis vectors for $\mathcal{H}_{chain}$ can be written as

$$|\boldsymbol{s}\rangle = |s_1\rangle \otimes |s_2\rangle \otimes ... \otimes |s_{N-1}\rangle \otimes |s_N\rangle, \tag{1.2}$$

where $s_i \in \{0,1\}$. Thus, any pure state can be written in this basis:

$$|\psi\rangle = \sum_{s_1,s_2,...,s_N} \psi_{s_1,s_2,...,s_N} |s_1\rangle \otimes |s_2\rangle \otimes ... \otimes |s_{N-1}\rangle \otimes |s_N\rangle, \tag{1.3}$$

where $\psi_{s_1,s_2,...,s_N} = \langle s_1, s_2, ...s_N|\psi\rangle$ is complex and $\sum_{s_1,s_2,...,s_N} \psi^*_{s_1,s_2,...,s_N}\psi_{s_1,s_2,...,s_N} = 1$.

Operators on chains of qubits can be similarly decomposed into a basis using the Pauli matrices:

$$\hat{O} = \sum_{a_1,a_2,...,a_N} O_{a_1,a_2,...,a_N} \sigma^{a_1} \otimes \sigma^{a_2} \otimes ... \otimes \sigma^{a_N}, \tag{1.4}$$

with $\sigma^a \in \{I, \sigma^x, \sigma^y, \sigma^z\}$. Alternatively, we can write an operator in terms of outer products of orthogonal basis states:

$$\hat{O} = \sum_{\boldsymbol{s}',\boldsymbol{s}} O_{\boldsymbol{s}',\boldsymbol{s}} |s'_1, s'_2, ...s'_N\rangle\langle s_1, s_2, ...s_N|, \tag{1.5}$$

(Note that we will often omit hats from operators when context allows). In particular, we can define statistical ensembles of pure states on our chain using a density matrix:

$$\rho = \sum_i p_i |\psi_i\rangle\langle\psi_i|. \tag{1.6}$$

In order to have a valid state, we must have $tr\rho = 1$ and $\rho^\dagger = \rho$. When ρ is a pure state we have $tr\rho^2 = 1$, otherwise $0 \leq tr\rho^2 < 1$ and the state is mixed.

1.2.1 Fermions

In addition to spin systems, we will also often concern ourselves with systems of fermions on a discrete lattice. On the same N-site lattice, we can define the following spinless fermion operators, which have the following anticommutation relations:

$$\{c_i, c_j^\dagger\} = \delta_{ij}, \quad \{c_i^\dagger, c_i^\dagger\} = \{c_i, c_i\} = 0 \tag{1.7}$$

States on single sites are labeled as either $|0\rangle$ (unoccupied) or $|1\rangle$ (occupied), such that

$$c^\dagger|0\rangle = |1\rangle, \quad c|1\rangle = |0\rangle. \tag{1.8}$$

These states can be annihilated, in accordance with their anticommutation relations, as follows:

$$c^\dagger|1\rangle = 0, \quad c|0\rangle = 0. \tag{1.9}$$

Starting with the completely empty state on N sites, $|\mathbf{0}\rangle$, we can define totally antisymmetric many-body basis states labeled by the occupation numbers at each site, $n_i \in \{0, 1\}$:

$$|n_1 n_2 n_3 ... n_N\rangle = (c_1^\dagger)^{n_1}(c_2^\dagger)^{n_2}(c_3^\dagger)^{n_3}...(c_N^\dagger)^{n_N}|\mathbf{0}\rangle. \tag{1.10}$$

The above states are known as Slater determinant states, and are antisymmetric under the exchange of any two sites. This follows from the fermionic anticommutation relations.

It is often useful to map systems of spin-1/2's to systems of fermions. This is accomplished in one dimension via the Jordan-Wigner transformation. As an example, consider the spin-1/2 XY model with periodic boundary conditions (PBCs), with the Hamiltonian

$$H = \sum_{i=1}^{N} \left(\sigma_i^x \sigma_{i+1}^x + \sigma_i^y \sigma_{i+1}^y \right). \tag{1.11}$$

We can recast the above Hamiltonian in terms of free fermions using the Jordan-Wigner transformation:

$$c_i^\dagger = \frac{1}{2}\left(\sigma_i^x + i\sigma_i^y\right), \quad c_i = \frac{1}{2}\left(\sigma_i^x - i\sigma_i^y\right), \quad c_i^\dagger c_i = \frac{1}{2}\left(\sigma_i^z + 1\right), \tag{1.12}$$

where we have included the map for σ_i^z for completeness, even though it does not appear in the XY Hamiltonian. One can easily verify that the above Jordan-Wigner transformation preserves the algebra of the fermionic creation and annihilation operators. Using the transformation on the XY Hamiltonian, we arrive at the following free-fermion Hamiltonian:

$$H = \frac{1}{2}\sum_{i=1}^{N}\left(c_i c_{i+1}^\dagger - c_i^\dagger c_{i+1}\right). \tag{1.13}$$

This can now be solved exactly using well-known free fermion methods.

Finally, we will have some occasion to use Majorana fermions. These are purely real-valued fermionic operators, γ, which can be defined in terms of complex fermions as

$$c_i = \frac{1}{\sqrt{2}}(\gamma_{2i-1} + i\gamma_{2i}), \quad c_i^\dagger = \frac{1}{\sqrt{2}}(\gamma_{2i-1} + i\gamma_{2i}) \tag{1.14}$$

Thus, an N-site chain of complex fermions becomes a $2N$-site chain of Majorana fermions. From the above definition, one can show that the Majorana fermions are self-adjoint and anticommuting:

$$\gamma_i^\dagger = \gamma_i, \quad \{\gamma_i, \gamma_j\} = 2\delta_{ij} \tag{1.15}$$

1.2.2 Tensor Networks

We will sometimes make use of the tensor network (TN) formalism for describing many body quantum states. These are a set of ansätze that use prior knowledge of the entanglement structure of a state to reduce the complexity of its numerical representation. If, for example, we are interested in studying a 1D chain of N qubits (or qudits, or some other object) with local Hilbert space dimension 2 (or d), the total Hilbert space dimension is 2^N (or d^N) and thus, for any reasonably large N, the full space of states cannot be efficiently represented or manipulated on a classical computer. However, if we have some basic information about the state in which we are interested — namely, its entanglement structure — we can confine ourselves to the small corner of the Hilbert space where such states live. This is the basic motivation behind tensor network constructions of many-body quantum states. We impose a basic skeleton of the entanglement structure in the form of a network of tensors contracted in a particular topology, and then use some form of variational optimization to find the components of these tensors to yield e.g. the ground state of a Hamiltonian.

Let us continue with the 1D spin chain example. Any state of a 1D chain of N qubits can be written as

$$|\psi\rangle = \sum_{i_1, i_2, ..., i_N \in [0,1]} \Psi_{i_1, i_2, ..., i_N} |i_1, i_2, ..., i_N\rangle \tag{1.16}$$

where the indices i_j correspond to the i^{th} state of the j^{th} qubit. In this case they take two possible values. The large tensor Ψ is an array of 2^N complex numbers corresponding to the coefficients of each basis state. This allows us to parameterize any state in the full Hilbert space. However, an important fact about the ground states many physical (local) 1D Hamiltonians is that they have short ranged, "area-law" entanglement. As a reminder, the Von Neumann entanglement entropy (which will be explained in further detail in upcoming sections of this chapter) S_A of an interval A in the above state is calculated as follows

$$S_A = -\mathrm{tr}\left(\rho_A \log \rho_A\right) \tag{1.17}$$

where $\rho_A = \mathrm{tr}_{A^c} \rho$ is the reduced density matrix of $\rho = |\psi\rangle\langle\psi|$, obtained by tracing out the states of the spins in the complement of A, A^c. An area-law entanglement means that S_A remains constant as we increase the size of the interval A. Thus, if we are interested in an area-law ground state, then we should only need to represent short-ranged quantum correlations, and we do not need the full representational power of the Hilbert space. We can instead restrict ourselves to big tensors Ψ consisting of an array of smaller tensors contracted in a 1D line:

$$\Psi_{i_1,i_2,\ldots,i_N} = A_{i_1}^{\mu_1\mu_2} A_{i_2}^{\mu_2\mu_3} \ldots A_{i_N}^{\mu_N\mu_1} \tag{1.18}$$

In the above, we retain the i_j "physical" indices, and these are the same as before, enumerating the states on a particular physical site. The additional indices μ_j are "virtual" or "bond" indices (summation on repeated indices is implied), and they range from 1 to χ, where χ is the "bond dimension", a number we may choose. This bond dimension determines the representational ability of the tensors, and bounds the amount of entanglement between neighboring sites. In using the above ansatz, we have gone from a Hilbert space of dimension 2^N, to one of dimension $2N\chi^2$, which, for typical χ, will be much smaller than the former. One can achieve additional compression by imposing translational invariance, and setting all of the A tensors to be the same. The above choice of tensor decomposition is known as a matrix product state or MPS [13], and is widely used for simulations of 1D systems. We can represent the above state and operations on it by a convenient diagrammatic formalism depicted in Fig. 1.1. In the formalism, a tensor is represented by a circle, and each leg extending from the circle corresponds to an index. Connecting two legs together corresponds to contracting or summing over the indices. Thus, the MPS described above can be depicted by a line of 3-legged tensors, as depicted in Fig. 1.2a [1]. The free legs are the physical indices and the contracted lines are the bond indices.

Heuristically, one can think of bounding the entanglement between two subregions of a tensor network by cutting the lines representing the bond indices in order to separate the two regions. One then would count the number of legs cut and multiply it by the associated bond dimensions to obtain an upper bound on the (exponent of) the entanglement entropy between the two regions. Thus, for MPS, this bound is always constant in the length of the subregions, and MPS are thus best-suited for representing area-law 1D states. One can use this heuristic

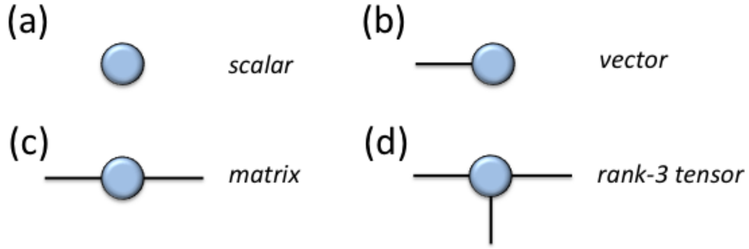

Figure 1.1: Diagrammatic representation of tensors. Each circle corresponds to a tensor, and each bond emanating from the circle corresponds to an index. Figure from [1] (reused with permission from publisher).

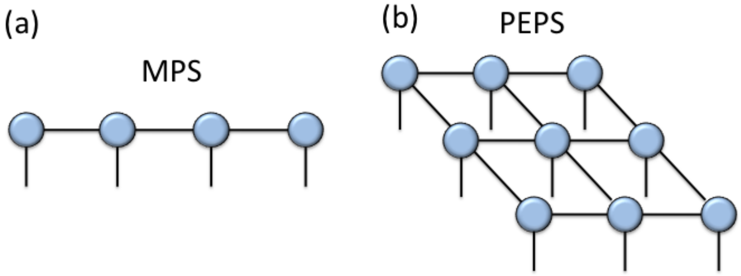

Figure 1.2: (a) A matrix product state in the diagrammatic formalism. (b) A projected entangled pair state. Figure from [1] (reused with permission from publisher).

to understand some of the other tensor network architectures, which are also built upon the underlying entanglement structure of the states they seek to represent. For example, projected entangled pair states (PEPs) [14], can be thought of as a 2D generalization of MPS, where 5 index tensors are contracted in a 2D array (see Fig. 1.2b). Another common TN architecture is the multiscale entanglement renormalization ansatz (MERA) [15], which represents scale invariant 1D states by adding an extra "renormalization" direction, which encodes long range correlations. MERA network states typically have entanglement entropy that grows logarithmically with the size of a subsystem, a characteristic feature of conformal field theories, which describe quantum critical points.

1.3 Measures of Entanglement in Pure States

Describing entanglement in many-body quantum systems is the central task of this thesis, so we must first define entanglement, and then introduce means to quantify it. We will first focus on entanglement in closed quantum systems, which are described by pure states. When encoded in a density matrix, ρ, a state is pure if $\mathrm{tr}\rho^2 = 1$. Thus, we can simply denote pure states with ket vectors.

At the most basic level, entanglement is a consequence of two basic features of quantum mechanics: superposition and the tensor product structure of multi-particle Hilbert spaces. If we have a system of N particles (or spins, or qudits, etc.), one can construct *product states* by taking tensor products of single particle states:

$$|\psi\rangle = |\phi_1\rangle \otimes |\phi_2\rangle \otimes ... \otimes |\phi_{N-1}\rangle \otimes |\phi_N\rangle, \tag{1.19}$$

where each $|\phi_j\rangle$ is an arbitrary state in the Hilbert space of the j^{th} particle. In the case of a two qubit system, for example, one can construct the following basis of product states:

$$\{|00\rangle, |01\rangle, |10\rangle, |11\rangle\}. \tag{1.20}$$

Now, the tensor product structure of the multi-particle Hilbert space allows us to decompose an arbitrary multi-particle state into a linear combination of product states. In general, however, these linear combinations will not also be product states. That is, no change of basis acting independently on each particle's Hilbert space can put the state in the form of 1.19. This feature — the inability to factorize a quantum state — is known as entanglement.

The simplest examples of entangled states are the Bell states of two qubits:

$$|B_1\rangle = \frac{1}{\sqrt{2}}\left(|00\rangle + |11\rangle\right) \tag{1.21}$$

$$|B_2\rangle = \frac{1}{\sqrt{2}}\left(|00\rangle - |11\rangle\right) \tag{1.22}$$

$$|B_3\rangle = \frac{1}{\sqrt{2}}\left(|01\rangle + |10\rangle\right) \tag{1.23}$$

$$|B_4\rangle = \frac{1}{\sqrt{2}}\left(|01\rangle - |10\rangle\right). \tag{1.24}$$

These states cannot be factorized into product states. On the other hand, the state

$$\frac{1}{2}\left(|00\rangle + |11\rangle + |10\rangle + |01\rangle\right) \tag{1.25}$$

may appear to be entangled at first glance, but upon further examination, it is clear that it can be factorized into the following form:

$$\frac{1}{2}\left(|0\rangle + |1\rangle)(|0\rangle + |1\rangle\right), \tag{1.26}$$

so it is not entangled.

Beyond these simple cases, how does one determine if two quantum systems in a pure state are entangled? To answer this, let's consider the physical consequences of entanglement. Consider the Bell state $|B_1\rangle$. If we perform a measurement in the Z-basis on the first qubit, the outcome will be either 0 or 1, with equal probability. Subsequent measurement outcomes of the second qubit will be fully determined by the outcome of the first. i.e. Measuring the first qubit in state 0 (1) guarantees that measuring the second qubit will yield 0 (1). The statistical ensemble of possible states of the second qubit after measurement of the first can then be expressed by the following density matrix:

$$\rho_2 = \frac{1}{2}\left(|0\rangle\langle 0| + |1\rangle\langle 1|\right). \tag{1.27}$$

This density matrix, which is referred to as the *reduced density matrix* on qubit 2, can be systematically obtained by taking a trace over an orthonormal basis supported only on qubit 1, while keeping only the matrix elements supported on qubit 2. Formally, this *partial trace* is denoted as follows:

$$\rho_2 = \mathrm{tr}_1 \rho, \tag{1.28}$$

where the subscript 1 indicates a partial trace over the Hilbert space of qubit 1, and ρ is the full density matrix of the Bell state $\rho = |B_1\rangle\langle B_1|$. For a general bipartite system consisting of subsystems A and B, with basis vectors $|\phi_A^i\rangle$ and $|\phi_B^j\rangle$, with the density matrix $\rho_{AB} = \sum_{i,j,k,l} \rho_{i,j,k,l} |\phi_A^i\rangle |\phi_B^j\rangle \langle \phi_A^k| \langle \phi_B^l|$, we can obtain the reduced density matrix on subsystem B by performing the partial trace over A via

$$\rho_B = \mathrm{tr}_A \rho_{AB} = \sum_m \sum_{i,j,k,l} \rho_{i,j,k,l} \langle \phi_A^m | \phi_A^i \rangle \langle \phi_A^k | \phi_A^m \rangle |\phi_B^j\rangle \langle \phi_B^l|. \tag{1.29}$$

Returning to the case of the two qubits in the Bell state. While the state of the full system is pure, once we trace out qubit 1, we obtain a mixed state on qubit 2. This can be seen by taking

$$\mathrm{tr}\left(\rho_2^2\right) = \frac{1}{2} \neq 1, \tag{1.30}$$

which indicates that the state is mixed. If after tracing out one party of a pure state of a bipartite system we obtain a mixed state, then the two parties are entangled. The extent to which these two components are entangled can be quantified by measuring the deviation of the reduced density matrix from a pure state. Thus, we introduce the Rényi entanglement entropies:

$$S^n(\rho_A) = \frac{1}{1-n} \log \mathrm{tr} \rho_A^n. \tag{1.31}$$

Where n indexes the different entropy measures (colloquially called the Rényi-n entropies). In the case of $n = 2$, we have a quantity that is proportional to the log of the purity. In the case of the Bell state this is $S^2(\rho_2) = \log 2$. When the state is pure, $S^2(\rho_2)$ clearly goes to zero.

The most interesting case of the above series of Rényi entropies occurs when we take the $n \to 1$ limit, in which case we obtain the Von Neumann entropy:

$$S_{VN}(\rho_A) = -\mathrm{tr}\left(\rho_A \log \rho_A\right). \tag{1.32}$$

As we will be using the Von Neumann Entropy ubiquitously throughout this thesis, let us first digress and discuss the behavior of the this quantity and provide physical interpretations so as to build intuition.

1.3.1 Von Neumann Entropy

Before explaining the features of the Von Neumann entropy, let us take a step back into classical information theory to describe the quantity's predecessor, the Shannon entropy,

$$H(p) = -\sum_i p_i \log_2 p_i. \tag{1.33}$$

which is defined for a classical probability distribution p, with probability for event i, p_i. Intuitively, the Shannon entropy quantifies either the uncertainty of outcome *before* observing an event from the distribution p, or the average amount of information gained *after* the observation of an event. That is, for a high entropy probability distribution, observing a particular event yields a large amount of information about the distribution. For a distribution of minimal entropy ($p_j = 1$ and $p_i = 0\ \forall i \neq j$), we learn nothing from an observation of the event j, as it is guaranteed to occur. For a discrete probability distribution over N events, the maximal entropy distribution is $p_i = \frac{1}{N}\ \forall i$. This, on average, yields the most information when we observe an event.

More specifically, the Shannon entropy quantifies the minimal information storage requirements (in units of bits) needed on average to store the outcome of an observation of an event from the distribution p, without incurring any information losses [16]. The maximal entropy flat distribution, $p_i = \frac{1}{N}$ requires that we have $\log_2 N$ bits on hand in order to record the outcomes (which are labeled 1 through N) in binary format. If, on the other hand, we are sampling from a distribution with certain events that are far more likely than others, we can use a binary representation consisting of $\log_2 \frac{1}{p_i}$ bits to store the occurrence of each event i. This will be a shorter binary string for the likely events and a longer string for the unlikely events, but on average, the string will be shorter than $\log_2 N$ if the entropy is not maximal.

Armed with some intuition about the classical Shannon entropy, we can now discuss the Von Neumann entropy in the context of quantum information theory. Once again, the Von Neumann entropy of a density matrix ρ takes the form

$$S_{VN}(\rho) = -\mathrm{tr}\left(\rho \log \rho\right), \tag{1.34}$$

which is very reminiscent of the form of the Shannon entropy. Indeed, expressed in terms of the eigenvalues of ρ, λ_i (which are all non-negative), the Von Neumann entropy reduces to the Shannon entropy:

$$S_{VN}(\rho) = -\sum_i \lambda_i \log \lambda_i. \tag{1.35}$$

As with the Shannon entropy, the Von Neumann entropy is maximized for the maximally mixed state — the density matrix of d dimensions consisting of the d-dimensional identity matrix multiplied by $\frac{1}{d}$. The quantity is minimized when there is a single unit eigenvalue, and the remaining eigenvalues are 0 (since $\mathrm{tr}\rho = \sum_i \lambda_i = 1$) — a pure state.

We will be using the Von Neumann entropy to quantify entanglement, so we must present an operational interpretation of this quantity in that light. The interpretation of the Shannon entropy as a measure of the number of bits required to store information cannot exactly be mapped onto the case of entanglement. In order to discuss this, we first note an important feature of measures of bipartite entanglement. If we compute the Von Neumann entropy of the reduced density matrix of party A in the total system $A \cup B$, we find that S_{VN} can only remain the same or be reduced under local operations and classical communication. That is, Alice can perform any valid quantum operations (unitary rotations, measurements, or other trace preserving completely positive (TPCP) maps) on her subsystem, A. Bob can do the same to B, and the two can communicate with classical information. However, they may not apply non-local operators that cannot be factorized into independent operators on A and B, respectively. Using only LOCCs, Alice and Bob can only reduce the entanglement of their two systems (in the extreme case, by performing local projective measurements), or maintain it. In particular, the Von Neumann entropy is invariant under local unitary transformations. That is, for a density matrix of a full system ρ_{AB}:

$$\rho'_{AB} = U\rho_{AB}U^{\dagger} \tag{1.36}$$

$$U = U_A \otimes U_B \tag{1.37}$$

$$S_{VN}(\rho'_A) = S_{VN}(\rho_A) \tag{1.38}$$

$$S_{VN}(\rho'_B) = S_{VN}(\rho_B). \tag{1.39}$$

With these basic facts in hand, how do we then go about making sense of the value of the Von Neumann entropy of entanglement computed for a particular bipartite pure state? We will use as our basic unit of bipartite entanglement measure the Bell state, for which

$S_{VN} = \log 2$, as this is the maximally entangled two-qubit state. Now we ask, given two entangled parties A and B in a pure state $|\psi_{AB}\rangle = \sum_i \sqrt{\lambda_i}|\phi_i^A\rangle|\phi_i^B\rangle$, how many Bell pairs of entanglement do they share? Since entanglement will in general will not exist in integer units of Bell pairs, we will be sharpening our question to ask how many, n, high fidelity Bell pairs we can produce with m copies of $|\psi_{AB}\rangle$, as $m \to \infty$. In this limit, the ratio n/m is called the distillable entanglement — the number of Bell pairs we can create using only LOCC from m copies of the state $|\psi_{AB}\rangle$. As we make m larger, the ratio converges to approximately $n/m \to S_{VN}(\rho_A)n/\log 2$ (where the division by $\log 2$ is a consequence of us using the natural logarithm, rather than the base two logarithm). To the quantum information theorist, this tells us how many individual qubits we can teleport from A to B using the state $|\psi_{AB}\rangle$. To the condensed matter theorist, this helps us bound the behavior of correlation functions. To this end, we define the mutual information of A and B:

$$I(A:B) = S_{VN}(A) + S_{VN}(B) - S_{VN}(A \cup B). \tag{1.40}$$

The mutual information is a non-negative quantity that upper bounds the value of properly normalized two-point correlation functions. That is, consider a state ρ with subregions A, B, and C, where $C = (A \cup B)^c$ (note that this is no longer necessarily a purely bipartite state). Given two operators, O_A and O_B, supported entirely within regions A and B, we can define the connected correlation function

$$\mathcal{C}(O_A, O_B) = \langle O_A O_B \rangle - \langle O_A \rangle \langle O_B \rangle, \tag{1.41}$$

where $\langle \cdot \rangle = \operatorname{tr}(\rho\, \cdot)$. Using properties of the trace [17], one can show the following bound:

$$I(A:B) \geq \frac{\mathcal{C}(O_A, O_B)^2}{2||O_A||^2||O_B||^2}, \tag{1.42}$$

where $||O||$ is the maximal eigenvalue of O. Thus, the mutual information, derived from the Von Neumann entropy, upper bounds the amount of *total* bipartite correlation between two systems A and B, which may or may not be in a pure state. In the case where ρ is a pure state consisting only of components A and B, then $I(A:B) = 2S_{VN}(\rho_A) = 2S_{VN}(\rho_B)$. In the case of a Bell pair, for example, we have $I(A:B) = 2\log 2$. Consider, however, Alice performing the following LOCC on her qubit, A [18]:

$$E_1 = \frac{1}{2}\mathbb{1}, \quad E_2 = \frac{1}{2}\sigma^z, \tag{1.43}$$

where these are Kraus operators in Alice's qubit's Hilbert space acting on the total density matrix like

$$\rho \to \rho' = E_1 \rho E_1^\dagger + E_2 \rho E_2^\dagger. \tag{1.44}$$

Given the initial density matrix of the two qubits, $\rho = |B_1\rangle\langle B_1|$, the resulting state after Alice's application of her operation is

$$\rho' = \frac{1}{2}\left(|00\rangle\langle 00| + |11\rangle\langle 11|\right). \tag{1.45}$$

The initial state ρ had mutual information $I(A:B) = 2\log 2$, and each qubit had $S_{VN} = \log 2$. Alice's operation produces a mixed state, ρ', with a lower mutual information of $I(A:B) = \log 2$, since $S_{VN}(\rho'_{AB}) = \log 2$. One can verify that this mixed state can still produce nonzero correlations, but it cannot act as a quantum resource by e.g. teleporting a qubit. Thus it is not entangled, which compels us to offer a broader definition of entanglement for mixed states. The Von Neumann entropy (and the mutual information based on it) cannot distinguish between quantum and classical correlations — correlations arising from entanglement vs. correlations arising purely from the probability distribution over a statistical ensemble of states. Thus, we are motivated to introduce entanglement criteria and measures for mixed states.

1.4 Measures of Entanglement in Mixed States

We have seen that Von Neumann entropy is an adequate measure of entanglement for pure states — that is, it quantifies the total number of Bell pairs distillable from a particular state. However, it fails to distinguish between classical, statistical correlations and quantum entanglement in mixed states. We will often want to quantify the bipartite correlations between two parties A and B that are in a mixed state, either because they have been mixed by external operators or because A and/or B are entangled with a complementary system, C. We thus introduce the separability criterion for entanglement in mixed states. A bipartite mixed state ρ is not entangled if it can be written as a separable state [19]:

$$\rho = \sum_i \lambda_i \rho_i^A \otimes \rho_i^B, \tag{1.46}$$

where λ_i are all non-negative, $\sum_i \lambda_i = 1$ and ρ_i^A and ρ_i^B are states on systems A and B, respectively.

How do we determine if a particular density matrix is separable? A necessary condition for separability of a density matrix is the positivity of the partial transpose [20]. That is, for a density matrix to be separable, it is necessary (but not sufficient) for its partial transpose to have only non-negative eigenvalues. Before discussing why, we first define the partial transpose. Consider decomposing a (possibly mixed) density matrix on $A \cup B$ into a basis:

$$\rho = \sum_{a,\beta,b,\gamma} \rho_{a\beta,b\gamma} |\phi_a^A\rangle|\phi_\beta^B\rangle\langle\phi_b^A|\langle\phi_\gamma^B|, \tag{1.47}$$

where we use Roman letters for system A and Greek letters for B. Taking the matrix elements, $\rho_{a\beta,b\gamma}$, the partial trace of ρ with respect to subsystem A is defined as

$$\left(\rho^{T_A}\right)_{a\beta,b\gamma} = \rho_{b\beta,a\gamma}. \tag{1.48}$$

Note that ρ^{T_A} is still Hermitian, so its eigenvalues are still real. However, the transformation does not necessarily leave the eigenvalues positive. However, one way in which the eigenvalues can remain non-negative is if our density matrix is separable. That is, if

$$\rho = \sum_i \lambda_i \rho_i^A \otimes \rho_i^B, \tag{1.49}$$

then

$$\rho^{T_A} = \sum_i \lambda_i (\rho_i^A)^T \otimes \rho_i^B. \tag{1.50}$$

Since both $(\rho_i^A)^T$ and ρ_i^B are still valid, Hermitian density matrices, each of which have non-negative eigenvalues, and λ_i are non-negative, then ρ^{T_A} is guaranteed to have non-negative eigenvalues.

Using the positive partial transpose (PPT) criterion, we can introduce the entanglement negativity as an entanglement measure. This quantity measures the extent to which the PPT criterion is violated in a particular density matrix. Specifically, we will use the logarithmic negativity in this thesis:

$$\mathcal{E} = \log |\rho^{T_A}|. \tag{1.51}$$

Here $|\cdot|$ indicates the trace norm, defined as

$$|M| = \mathrm{tr}\sqrt{MM^\dagger}. \tag{1.52}$$

$\mathcal{E}$ is zero when ρ^{T_A} has no negative eigenvalues.

Operationally, the logarithmic negativity measures the asymptotic number of distillable Bell pairs from a bipartite state, much like the Von Neumann entropy. Unlike the Von Neumann entropy, however, it distinguishes between classical and quantum correlations, and so can measure entanglement in states that are overall mixed.

1.5 Measures of Multiparty Entanglement

We have so far discussed entanglement of two component systems. In that case, we are able to quantify entanglement for a particular bipartite system with a single number, either Von Neumann entropy or negativity. However, qualitatively different types of entanglement emerge when we introduce more than two parties. That is, when we divide a system into more than two parts, there are entangled states that cannot be converted to Bell pairs via LOCC. The number of different types of entanglement grows with the number of components of a system, and there is no universal way to classify or quantify each type, beyond the case of a very small number of qubits [21]. Here we will only provide a few examples of multipartite entanglement in three and four body systems, to provide some intuition for the complexity of the problem, and for multipartite operator entanglement measures introduced later in this thesis. We will also focus only on pure states, as the story involving mixed states is even more complicated.

Let's first recall that bipartite pure states can always be Schmidt decomposed using local unitary operators:

$$|\psi\rangle = \sum_i \sqrt{\lambda_i} |\phi_i^A\rangle |\phi_i^B\rangle. \tag{1.53}$$

The Schmidt eigenvalues $\sqrt{\lambda_i}$ (whose squares are the reduced density matrix eigenvalues) fully encode the bipartite correlations of the state. Von Neumann entropy, Rényi entropies and negativity can all be expressed as functions of these values. On the other hand, three party states cannot in general be written in the following form using only local unitary operations (although some can):

$$|\psi\rangle = \sum_i \sqrt{\lambda_i} |\phi_i^A\rangle |\phi_i^B\rangle |\phi_i^C\rangle. \tag{1.54}$$

Thus, whatever entanglement measures we devise, they will not be functions of a single array of Schmidt eigenvalues, but rather functions of a tensor of coefficients.

To provide a simple example of a tripartite state that cannot be Schmidt decomposed, consider the three-qubit W-state:

$$|W\rangle = \frac{1}{\sqrt{3}} \left(|100\rangle + |010\rangle + |001\rangle \right). \tag{1.55}$$

Try as one might, using local unitary operators of the form $U_A \otimes U_B \otimes U_C$, there is no way to write this state as a tripartite Schmidt decomposition. Indeed, in a sense, this state is "maximally non-decomposable" in that its density matrix cannot be written in terms of fewer than three separable states. This gives rise to interesting features distinct from those seen in bipartite entanglement. Tracing out any one of the three qubits gives rise to an entangled mixed state on the remaining two qubits (though not a maximally entangled state). Observing a 0 result from the measurement of a qubit yields a Bell pair on the remaining two, while a 1 measurement result yields a product state. The W state can be further generalized to N-qubits following an obvious pattern.

The other distinct class of tripartite entanglement is GHZ-type entanglement. The paradigmatic GHZ state is

$$|GHZ\rangle = \frac{1}{2} \left(|000\rangle + |111\rangle \right). \tag{1.56}$$

While the W-state is somewhat robust to measurements, tracing out any two qubits in a GHZ state yields a maximally mixed state on the remaining qubit. Indeed, 0 or 1 projective measurements on any single qubit yield product states on the remaining two qubits. On the other hand, a projective measurement in the x-basis on any single qubit yields a Bell state on the remaining two. GHZ entanglement is thus, in some sense less robust but more distributed than W-type entanglement. The two states, unlike the four Bell states, cannot be transformed into each other by LOCC, and are thus qualitatively different from each other. We thus need multiple measures to quantify the amount of each type of entanglement. One can fully classify the amount of bipartite, W, and GHZ-type entanglement by constructing local unitary invariant functions on the tensor of coefficients Γ^{ijk} of the state [22]

$$|\psi\rangle = \sum_{ijk\in\{0,1\}} \Gamma^{ijk}|i\rangle|j\rangle|k\rangle. \tag{1.57}$$

These functions take the form of generalizations of the matrix determinant. We will not discuss the quantities that arise from this sort of analysis (like the three-tangle) any further in this thesis. We allude to them only to express the complexity of multipartite entanglement. We will instead provide a few examples of how quantities derived from Von Neumann entropy and logarithmic negativity behave in different three and four-qubit states, as a primer for interpreting tripartite operator mutual information and negativity values.

Starting with the GHZ state on three qubits, one can make attempt at understanding its correlations by computing the mutual information between two of the three qubits. One will find

$$I(A:B)_{GHZ} = \log 2, \tag{1.58}$$

indicating that qubits A and B are correlated with each other. However, computing the logarithmic negativity yields

$$\mathcal{E}(A:B)_{GHZ} = 0. \tag{1.59}$$

This tells us that there is no distillable bipartite entanglement between qubits A and B, although the GHZ state is clearly itself entangled. The mutual information was only detecting classical correlations introduced by tracing out qubit C. This motivates us to generalize these quantities. We first introduce the tripartite information (or the tripartite mutual information):

$$I_3(A:B:C) = I(A:B) + I(A:C) - I(A:B\cup C). \tag{1.60}$$

Computing I_3 for a three qubit GHZ state, however, yields 0, indicating that it is not sensitive to GHZ-type entanglement. Indeed, I_3 is zero for any three party pure state, but will be useful for mixed states and four party states. We thus generalize negativity in a similar way and introduce tripartite logarithmic negativity [23]:

$$\mathcal{E}_3(A:B:C) = \mathcal{E}(A:B) + \mathcal{E}(A:C) - \mathcal{E}(A:B\cup C). \tag{1.61}$$

Computing $\mathcal{E}_3$ for the GHZ state yields $-\log 2$. Negative values indicate, roughly, that there are quantum correlations stored in the entire system that cannot be accessed by any subsystem alone. In the case of the W state, I_3 is of course still 0. On the other hand, $\mathcal{E}_3$ is positive for W-like states.

1.6 Conformal Field Theory and AdS/CFT

We will be using results from the AdS/CFT correspondence in this thesis as a means to the end of studying entanglement in strongly correlated quantum field theories. Thus, we will only introduce the basic tools necessary to do this, namely the Ryu-Takayanagi formula. The topic of AdS/CFT is far too expansive to cover thoroughly in this thesis, let alone this chapter. For a thorough reference on conformal field theory, one can look to [24]. For reviews on the AdS/CFT correspondence, one can look to e.g. [25], among many other resources.

For our purposes, it suffices to state simply that the AdS/CFT correspondence establishes an equivalence (in an appropriate limit) between the partition functions of a theory of gravity on a $d+1$-dimensional, asymptotically Anti-de Sitter space (the “bulk”) and a conformal field theory on the d-dimensional asymptotic boundary of this space:

$$Z_{AdS_{d+1}} = Z_{CFT_d}. \tag{1.62}$$

We will be interested in the limiting case where the bulk gravity theory is classical (that is, where G_N is very small). This corresponds to a very strongly coupled CFT with a large central charge $c \gg 1$. In this case, where $d = 2$ (the only case we will be using), the bulk metric takes the form

$$ds^2 = \left(1 + \frac{r^2}{L^2}\right) dt^2 + \frac{dr^2}{1 + \frac{r^2}{L^2}} + r^2 d\phi^2 \tag{1.63}$$

for the vacuum state of the CFT. In the above L is the radius of curvature. One can show using the stress-energy tensor that the central charge of the boundary CFT is

$$c = \frac{3L}{2G_N}, \tag{1.64}$$

indicating that weaker gravitational forces correspond to larger central charges.

Our main result is the Ryu-Takayanagi formula, which takes the following form:

$$S_{VN}(A) = \frac{\text{Area}(\gamma_A)}{4G_N}. \tag{1.65}$$

This equation states that the Von Neumann entropy of a subregion A of the boundary CFT is proportional to the area (length in the case of $d = 2$) of the minimal length surface (geodesic) γ_A in the bulk that is homologous to the boundary region A (that is $\partial\gamma_A = \partial A$).

A full derivation of this result is beyond the scope of this section, and we point the interested reader to [26] for more details. For the purposes of this thesis, the Ryu-Takayanagi formula will serve as a way to calculate entanglement entropy in certain strongly coupled (holographic) CFTs.

CHAPTER 2

BENDING AND CURVING ENTANGLEMENT IN HOLOGRAPHIC CFTS

Spatial inhomogeneity is ubiquitous in quantum many-body systems realized, e.g., in solid states and cold atomic gases. One source of inhomogeneity is impurities or randomness, but it can also be introduced intentionally, for example via a harmonic trap confining cold atomic gas. Inhomogeneity can have a dramatic effect in quantum many-body systems, e.g., it can alter the ground states completely – we will discuss some examples momentarily. On the theoretical side, the vast majority of past work has focused on homogeneous systems, and we need to develop new tools to deal with inhomogeneous ones.

2.1 Introduction

In this chapter (in work based on [27]), we study a series of inhomogeneous quantum many-body systems in (1+1) dimensions constructed in the following way: Let us start from a homogeneous quantum many-body Hamiltonian

$$H = \int dx \, \mathcal{H}(x) \tag{2.1}$$

where $\mathcal{H}$ is the Hamiltonian density, given by the 00 component of the energy-momentum tensor, $\mathcal{H} \sim T_{00}$. The spatial manifold here can be non-compact (i.e., infinite line $x \in [-\infty, +\infty]$) or compact (i.e., circle of a finite circumference L, $x \in [0, L]$). Similarly, for a homogeneous system defined on a one-dimensional lattice, one can consider the Hamiltonian $H = \sum_i \mathcal{H}_i$, where $\mathcal{H}_i$ is the Hamiltonian density at a given lattice site i. By "deforming"

H by an envelope function $f(x)$, we then consider an inhomogeneous system

$$H[f] = \int dx\, f(x)\, \mathcal{H}(x), \tag{2.2}$$

or $H[f] = \sum_i f(x_i)\mathcal{H}_i$ for lattice systems.

Of central focus in this chapter are the fundamental properties of the deformed Hamiltonians, mainly the scaling of the bipartite Von Neumann entropy both at zero and finite temperatures. In this work, we will focus on the cases where the original, homogeneous, Hamiltonians are those of (1+1)d conformal field theories (CFTs).

2.1.1 Rainbow chains

One deformation of central interest is the so-called rainbow chain. [28–33] The rainbow chain is an inhomogeneous (1+1)d quantum lattice model, in which the envelope function $f(x)$ decays exponentially away from a central site,

$$f(x) = e^{-h|x|}, \tag{2.3}$$

where h is a parameter. For example, for the free fermion hopping model, we consider

$$\begin{aligned} H &= \sum_{i,j=1}^{N} t_{ij} c_i^\dagger c_j, \\ t_{ij} &= -f_i \delta_{i-j,1} - f_i \delta_{i-j,-1}, \end{aligned} \tag{2.4}$$

where $c_i^\dagger / c_i$ are the fermion creation/annihilation operators at site i, N is the total number of lattice sites, and

$$f_j = e^{-h|j-N/2|} \tag{2.5}$$

(where the center has been shifted to $j = N/2$). The homogeneous counterpart (where $f_j = const.$) realizes, at half-filling (partial filling), the $c = 1$ free fermion CFT in the continuum limit.

An interesting feature of this model is that the entanglement entropy shows volume law scaling; It was found that the entanglement entropy of the reduced density matrix, when the chain is bipartitioned at the center and the half of the chain is traced out, grows linearly with respect to the subsystem size. The properties of the rainbow chain on the lattice in the strong inhomogeneity (large h) limit, can be accurately captured using a version of Dasgupta and Ma's strong disorder renormalization group [34]. In this limit, the ground state of the chain consists of concentric singlets, centered around the middle of the chain. This is the origin of the volume law entanglement for intervals on either side of the central bond.

It has been also understood that, in the continuum, introducing the rainbow chain deformation is equivalent to putting the CFT on a curved spacetime with the metric: [31]

$$ds^2_{AdS_2} = -e^{-2h|x|}dt^2 + dx^2. \tag{2.6}$$

This is the metric of AdS_2. Here, h is the curvature scale (the inverse radius) of AdS_2. By a change of the coordinates to

$$\eta = \operatorname{sgn}(x)\frac{e^{h|x|}}{h}, \tag{2.7}$$

the metric can also be written as

$$ds^2_{AdS_2} = \frac{1}{h^2\eta^2}\left(d\eta^2 - dt^2\right), \tag{2.8}$$

which is the Poincaré patch of AdS_2.

2.1.2 Möbius and SSD deformations

Another interesting class of deformations are Möbius deformations and the sine-square deformation (SSD) [35–47, 47–52]. Starting from the uniform system defined on a spatial circle of circumference L, the Möbius evolution is given by

$$f(x) = 1 - \tanh(2\gamma)\cos\frac{2\pi x}{L}. \tag{2.9}$$

Here, γ is a parameter; $\gamma = 0$ corresponds to the uniform Hamiltonian, whereas when $\gamma \to \infty$,

$$f(x) = 1 - \cos\frac{2\pi x}{L} = 2\sin^2\frac{\pi x}{L}. \tag{2.10}$$

The resulting evolution operator is called the sine-square deformation (SSD) of the original Hamiltonian. Correspondingly, one can consider the lattice Hamiltonian (2.4), now with the hopping amplitude $f_j = 2\sin^2(j\pi/N)$.

The initial interest in the SSD comes from the observation that the ground state of the SSD Hamiltonian on an open chain (when the system is described by CFT), is equal to the ground state of the uniform Hamiltonian on a finite circle with periodic boundary conditions. This feature makes the SSD useful for removing edge effects in finite-size DMRG calculations.

Similar to the rainbow deformation, the Möbius/SSD deformations can also be understood by putting CFTs on a curved background with the metric [50]

$$ds^2_{Mobius} = -\left(1 - \tanh 2\gamma\cos\frac{2\pi x}{L}\right)^2 dt^2 + dx^2. \tag{2.11}$$

In addition to the rainbow and Möbius/SSD deformations, various other examples of inhomogeneous systems include entanglement Hamiltonians, [53–55] the square root deformation (known in the context of perfect state transfer), [48] free fermions in harmonic traps and other potentials, [56] hyperbolic deformations, and others. [57–62]

In this chapter, we will discuss a series of inhomogeneous (1+1)d systems, which are given as deformations of uniform CFTs. Of particular interest is the scaling of entanglement entropy at zero and finite temperatures, which we obtain by combining field theory, holographic, and numerical approaches.

As for the holographic approach, we develop holographic duals of inhomogeneous (1+1)d CFTs by finding appropriate foliations (slicings) of the bulk AdS_3. The simplest example would be to foliate AdS_3 by (1+1)d flat Minkowski spaces, which, at the asymptotic boundary, gives rise to CFT on a flat space. Other foliations are also possible, realizing CFT put on different metrics. For example, AdS_3 can be foliated by AdS_2, [63–65] which, as we will discuss, realizes the rainbow chain at the boundary.

We will also discuss holographic duals of inhomogeneous CFTs at finite temperatures, by starting from the bulk spacetime with the BTZ black hole, and following the same strategy as the zero temperature case mentioned above. We will show that sensible foliations, valid for low temperatures, can easily be constructed by a brute force application of the coordinate transformations that we use to construct the foliations for the corresponding zero-temperature geometry. This naive approach, however, breaks down at higher temperatures, and better foliations must be constructed to capture the full temperature dependence of entanglement entropy.

In order to systematically derive suitable finite temperature geometries, we must solve Einstein's equations in the bulk with a constant, negative cosmological constant, with our curved $2d$ metric of interest given as a boundary condition. Finding solutions of the Einstein equation with a prescribed boundary metric is a well-studied problem. See for example, Ref. [66]. Our strategy as presented above differs from the one in the aforementioned reference, but yields finite temperature results that agree very well with numerics. We will however, remark briefly on the more systematic approach, which involves solving Einstein's equations exactly for a given boundary metric. The advantage of our foliation-based approach, is that we need not find new geodesics in our bulk geometry; we can simply use the geodesics from the BTZ spacetime, being sure to implement an appropriate UV cutoff.

Finally, We will also look briefly at a larger class of deformations known as "solution-generating diffeomorphisms". In particular, we will discuss a holographic description of these inhomogeneous systems, and their entanglement properties.

2.2 Different foliations in AdS/CFT and entanglement entropy

In this section, we collect necessary ingredients to describe the holographic duals of rainbow and SSD deformations, and the calculations of entanglement entropy.

2.2.1 Different foliations in AdS/CFT

In the AdS/CFT correspondence, the CFT is defined ("lives") on an asymptotic boundary of AdS. What concerns us in developing our holographic description of inhomogeneous systems is the fact that the AdS spacetime can be foliated (sliced) in various different ways. Different foliations (slicings) give rise to different asymptotic boundaries, and hence correspond to different situations on the CFT side. (See below, in particular Sec. 2.2.1.)

For example, consider the Poincaré patch of AdS described by the metric:

$$ds^2_{AdS_3} = R^2 \frac{dz^2 + dx^2 - dt^2}{z^2}, \tag{2.12}$$

where $z > 0$ and $-\infty < t, x < +\infty$, and R is the radius of AdS. (This coordinate patch covers only half of AdS_3.) In these coordinates, AdS_3 is foliated by $(1+1)$d flat spacetimes described by the coordinate (t, x) (Fig. 2.1). Realized at the asymptotic boundary $z \to 0$ is the CFT in its ground state defined on the infinite line $-\infty < x < +\infty$. Here, as usual, the central charge of the CFT is $c = 3R/(2G_N)$ where G_N is the Newton constant.

Rindler evolution

AdS_3 has foliations other than the one suggested by the Poincaré metric. Let us consider the Rindler-AdS foliation, [67–70] which can be obtained from the Poincaré metric by the z-independent coordinate transformation,

$$t = u \sinh(ht'), \quad x = u \cosh(ht'), \tag{2.13}$$

where $u > 0$ and $-\infty < t' < \infty$. This coordinate covers half of the original space, so that the system is at a finite Unruh temperature. The metric in this coordinate is

$$ds^2_{AdS_3} = \frac{R^2}{z^2}\left[(-h^2u^2dt'^2 + du^2) + dz^2\right]. \tag{2.14}$$

It is also instructive to introduce a tortoise coordinate $x' \in [-\infty, +\infty]$ by $u =: h^{-1}e^{hx'}$. The metric is

$$ds^2_{AdS_3} = \frac{R^2}{z^2}\left[e^{2hx'}(-dt'^2 + dx'^2) + dz^2\right]. \tag{2.15}$$

Here,

$$ds^2_{Rindler} = e^{2hx'}\left(-dt'^2 + dx'^2\right) \tag{2.16}$$

is the line element of the 2d Rindler space. From Eq. (2.14), we read off the Rindler Hamiltonian,

$$H_{Rindler} \sim \int_0^\infty du\, u\, \mathcal{H}(u). \tag{2.17}$$

This is nothing but the entanglement Hamiltonian of the half space, starting from the vacuum of CFT. (The entanglement Hamiltonian of the finite interval can be discussed similarly.

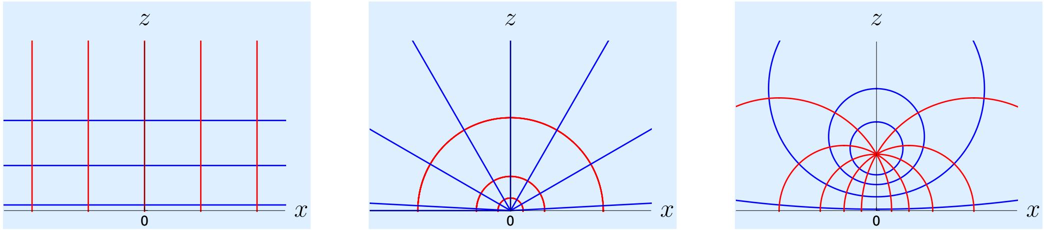

Figure 2.1: Three different foliations of AdS_3 by flat Minkowski spaces (Left), AdS_2 (Middle), and 2d spaces with the metric (2.11) (Left). (Middle) Lines of constant η (red) and Θ (blue) for the rainbow coordinate transformation (2.18); (Right) Lines of constant v (red) and u (blue) for the SSD coordinate transformation (2.21) with $a = 1$. Both are plotted in the original Poincaré spatial coordinates, x and z.

[55, 71])

In the Rindler foliation, the coordinate system (2.13) covers only the half of the boundary. In other words, observers in the coordinate patch (2.13) cannot access the other half. The observers are hence effectively at finite temperature.[72] Correspondingly, in the bulk, there is a topological black hole. [71] Other foliations of AdS_3 lead to other inhomogeneous field theories on the boundary.

Rainbow chain

To realize the rainbow chain, we foliate AdS_3 by AdS_2. [63–65] The corresponding metric can be obtained from the Poincaré metric (2.12) by the following t-independent coordinate transformation:

$$z = \eta \cos(h\Theta), \quad x = \eta \sin(h\Theta), \tag{2.18}$$

where $\eta > 0$ and $-\pi/2h < \Theta < \pi/2h$. Contours of constant η and Θ are plotted in Fig. 2.1. The metric is given by

$$ds^2_{AdS_3} = \left[\frac{h^2 R^2}{\cos^2(h\Theta)}\right] \left[d\Theta^2 + ds^2_{AdS_2}\right], \tag{2.19}$$

where $ds^2_{AdS_2}$ is given by (2.8). There are *two* asymptotic boundaries, one at $\Theta = +\pi/2h$ and the other at $\Theta = -\pi/2h$. There are two CFTs, one for each boundary, which are put on AdS_2. These two CFTs are not decoupled, but are connected at the boundary of AdS_2. The ground state is highly entangled between the two CFTs.

Möbius and SSD evolution

The prescription of generating the holographic dual of the rainbow chain can be generalized, by considering different t-independent coordinate transformations than (2.18). Let us now consider a coordinate map

$$u + iv = \log(z + ix + a) - \log(z + ix - a), \tag{2.20}$$

where a is a real parameter. Inverting this and separating the real and imaginary parts, we have:

$$z = \frac{a \sinh u}{\cosh u - \cos v}, \quad x = \frac{-a \sin v}{\cosh u - \cos v}, \tag{2.21}$$

where $u \in [0, \infty)$ and $v \in [0, 2\pi)$. This coordinate transformation is plotted in Fig. 2.1. Our Poincaré metric thus becomes

$$ds^2_{AdS_3} = \frac{1}{\sinh^2 u}\left[du^2 + dv^2 - a^{-2}(\cosh u - \cos v)^2 dt^2\right] \tag{2.22}$$

and our conformal boundary now occurs as $u \to 0$. Near the boundary $u \to u_0$, the boundary metric is given by

$$ds^2 = \left[\frac{1}{a \tanh u_0}\right]^2 \left[-\left(1 - \frac{\cos v}{\cosh u_0}\right)^2 dt^2 + \frac{a^2 dv^2}{\cosh^2 u_0}\right] \tag{2.23}$$

where u_0 is the UV cutoff. To make contact with (2.10), we introduce a parameter γ by

$$\tanh 2\gamma = \frac{1}{\cosh u_0}. \tag{2.24}$$

By further introducing L by

$$\frac{L}{2\pi} = \frac{a}{\cosh u_0} \overset{u_0 \to 0}{\longrightarrow} a, \tag{2.25}$$

and the change of variable $v = 2\pi x/L$, we arrive at

$$ds^2 = \left[\frac{\cosh 2\gamma}{a}\right]^2 ds^2_{Mobius}, \tag{2.26}$$

where ds^2_{Mobius} is given by (2.11). In our metric (2.23), the UV cutoff u_0 plays the role of γ; one can then see that our foliation realizes a regularized version of the SSD.

Dipolar limit It is also interesting to take the limit $a \to 0$, while keeping z/a and x/a finite; this is the dipolar limit. We then consider the coordinate transformation:

$$u + iv = \frac{a}{z + ix}. \tag{2.27}$$

Separating into real and imaginary parts, we have,

$$x = \frac{-av}{u^2 + v^2}, \quad z = \frac{au}{u^2 + v^2}. \tag{2.28}$$

The metric is then given by

$$ds^2_{AdS_3} = \frac{R^2}{u^2}\left[dv^2 - a^{-2}(u^2 + v^2)^2 dt^2 + du^2\right], \tag{2.29}$$

where $u \to 0$ corresponds to the conformal boundary. Near the boundary $u \sim u_0$, the metric for a given slice is

$$ds^2 = \frac{R^2}{u_0^2}\left[-a^{-2}(v^2 + u_0^2)^2 dt^2 + dv^2\right]. \tag{2.30}$$

Foliations and UV cutoff

For each of the different coordinate transformations we considered above, we have an associated "natural" foliation; For example, in (2.19), we have a family of surfaces with AdS_2 metric parameterized by Θ. To properly define CFTs in the asymptotic boundaries, we further need to introduce a UV cut off. We do so by taking our cutoff surface, i.e., the surface where we define our CFTs, to be one of the slices located near (but away from) the boundary (boundaries). This is the UV cutoff which is "consistent" or "natural" for a given foliation. In terms of the Poincaré coordinate (2.12) that we started with, this means that our the cutoff is position-dependent (x-dependent). Assuming our bulk foliation is dictated by a coordinate transformation, $z = z(u, v)$ and $x = x(u, v)$ (where u and v are our new radial and transverse coordinates, respectively), we replace the UV cutoffs with their curvilinear counterparts:

$$\epsilon \to z(u = \epsilon, v(x)) \simeq \left.\frac{\partial z(u, v)}{\partial u}\right|_{\substack{u=0\\ v=v(x)}} \epsilon. \tag{2.31}$$

It is worth emphasizing that it is because of the cutoff that we realize a "different CFT" as mentioned, e.g., in Ref. [68]. For example, the metric of the type (2.19) was previously used to discuss holographic duals of boundary CFTs (BCFTs) [73, 74]; In the $AdS/BCFT$ correspondence, one realizes a BCFT on AdS_2 which has a boundary (or boundaries). There, however, one imposes the "original" cutoff using the flat Minkowski cutoff surfaces.[73]

Solution generating diffeomorphisms (SGDs)

We can construct a family of locally AdS_3 spacetimes with the appropriate asymptotic behavior (i.e. that preserve the form of the Fefferman-Graham metric, up to gauge transformations) by acting on the vacuum metric with a certain class of diffeomorphisms.[70, 75] Applying one of these transformations corresponds to exciting a state in the CFT.[76–78] We say therefore that they are "solution-generating diffeomorphisms".

Using light cone coordinates for the boundary, $x_\pm = t \pm x$, we can parameterize the transformations as follows:

$$x_\pm = f_\pm(\tilde{x}_\pm), \quad z = \tilde{z}\sqrt{f'_+(\tilde{x}_+)f'_-(\tilde{x}_-)}. \tag{2.32}$$

Starting from the Poincaré metric (2.12), we obtain the following bulk metric in the new coordinates:

$$ds^2_{AdS_3} = \frac{d\tilde{z}^2 - d\tilde{x}_+ d\tilde{x}_-}{\tilde{z}^2} + (A_+ d\tilde{x}_+ + A_- d\tilde{x}_-)^2 + \frac{2d\tilde{z}}{\tilde{z}}(A_+ d\tilde{x}_+ + A_- d\tilde{x}_-) \tag{2.33}$$

where $A_\pm = -(1/2)f''_\pm(\tilde{x}_\pm)/f'_\pm(\tilde{x}_\pm)$.

Although these diffeomorphisms preserve the form of the metric and are therefore trivial gauge transformations from the perspective of the bulk, they are nontrivial at the asymptotic boundary. This nontriviality can be understood by observing that the SGDs result in nonzero contributions to the boundary stress tensor from the Schwarzian derivative:

$$T_{\pm\pm} = \frac{c}{48\pi f'_\pm(\tilde{x}_\pm)^2}\left[3f''_\pm(\tilde{x}_\pm)^2 - 2f'_\pm(\tilde{x}_\pm)f'''_\pm(\tilde{x}_\pm)\right], T_{+-} = 0.$$

With the stress-tensor in hand, we can write the metric (2.33) in Fefferman-Graham form:

$$ds^2_{AdS_3} = \frac{dz^2}{z^2} - \frac{1}{z^2}\left[dx_+dx_- + \frac{z^2}{4}\left(L(x_+)dx_+^2 + \bar{L}(x_-)dx_-^2\right) + \frac{z^4}{16}L(x_+)\bar{L}(x_-)dx_+dx_-\right], \tag{2.34}$$

where $L(x_+) = \frac{48\pi}{c}T_{++}$ and $\bar{L}(x_-) = \frac{48\pi}{c}T_{--}$ [66]. The nonzero energy-momentum tensor means that we are in an excited state of the original CFT. Indeed, we can write this state explicitly by finding a unitary representation of our diffeomorphisms. For a diffeomorphism (written in complex coordinates $z = x + it$) $f(z) = \sum_{n=-\infty}^{\infty} \epsilon_n z^{-n+1}$, this state is given by $|\Omega\rangle_f = U(\epsilon)|0\rangle$, where[78] $U(\epsilon) = \exp\left(\sum_{n=-\infty}^{\infty} \epsilon_n L_{-n}\right)$, where, L_{-n} are the standard Virasoro generators in an appropriate representation.

Note that z and $x_\pm$ in (2.34) are *not* the same as the original Poincaré coordinates; they are chosen specifically to put the metric in Fefferman-Graham form. In this gauge, the metric has a horizon located at $z = z_H = 2(L(x_+)\bar{L}(x_-))^{-1/4}$. As $z \to 0$, we see that we recover the flat Minkowski metric. To investigate our excited state, we must use a constant $\tilde{z} = \epsilon$ cutoff corresponding to the curvilinear cutoff

$$z = \epsilon\sqrt{f'_+(\tilde{x}_+)f'_-(\tilde{x}_-)}. \tag{2.35}$$

The essential physics in both the SGD protocol and the prescription we have outlined in this chapter is the same. In both cases, we pick a UV cutoff for our bulk spacetime that depends on the transverse Poincaré coordinates. In our prescription, we arrive at the curvilinear cutoff by performing a particular time-independent coordinate transformation, while in the SGD case, the cutoff emerges as a natural result of extending a conformal transformation into the bulk. A key difference between the two is that SGDs are in general time-dependent, since they are formulated in terms of light-cone coordinates. Indeed, the class of Weyl transformations that the SGDs induce on the UV cutoff surface is limited to those of the form $\exp(2\phi(\tilde{x}_+, \tilde{x}_-)) = f'_+(\tilde{x}_+) f'_-(\tilde{x}_-)$, while in our prescription, the Weyl transformations depend purely on the transverse spatial coordinate (e.g. $\exp(2\phi(u)) = 1/u^2$ for the rainbow chain). Nevertheless, SGDs can be used to construct many interesting foliations of AdS_3. Examples include the Rindler foliation mentioned previously, the Hopf fibration[79], and various two-sided geometries mentioned in Ref. [77].

2.2.2 Entanglement entropy

Zero temperature

Once we have obtained a foliation of AdS_3 corresponding to our inhomogeneous system of interest, we can use the Ryu-Takayanagi procedure to compute the bipartite entanglement entropy of a particular interval on the boundary. [11, 12, 80] We start by using the known result for the zero temperature holographic entanglement entropy for an interval $[x_1, x_2]$ on the asymptotic boundary of the Poincaré patch:

$$S_A^{holo}(x_1, x_2) = \frac{c}{3} \log \left[\frac{x_2 - x_1}{\sqrt{\epsilon_1}\sqrt{\epsilon_2}} \right]. \tag{2.36}$$

As before, assuming our bulk foliation is dictated by a coordinate transformation, $z = z(u, v)$ and $x = x(u, v)$ (where u and v are our new radial and transverse coordinates, respectively), we replace the UV cutoffs, ϵ_1 and ϵ_2 with their curvilinear counterparts:

$$\epsilon_i \to z(u = \epsilon, v(x_i)) = \left. \frac{\partial z(u, v)}{\partial u} \right|_{\substack{u=0 \\ v_i = v(x_i)}} \epsilon. \tag{2.37}$$

Equation (2.36) then becomes

$$S_A^{holo}(v_1, v_2) = \frac{c}{3} \log \left[\frac{x(u = 0, v_2) - x(u = 0, v_1)}{\epsilon \sqrt{\frac{\partial z(u=0, v_1)}{\partial u} \frac{\partial z(u=0, v_2)}{\partial u}}} \right]. \tag{2.38}$$

For example, in the dipole foliation, where $z = \frac{au}{u^2+v^2}$, the UV-cutoff and transverse coordinate transform as

$$\epsilon_i = \frac{a}{v_i^2}\epsilon, \quad x_i = x(u=0, v_i) = \frac{-a}{v_i}. \tag{2.39}$$

We can plug these into (2.36) to find the holographic entropy of the dipole foliation. Similarly, for metric (2.33), using the cutoff (2.35), we can compute the entanglement entropy of an interval in the $\tilde{x}_\pm$ coordinates: [76, 81]

$$S_A(x_1, x_2) = \frac{c}{12} \log \left[\frac{\mathcal{L}(\tilde{x}_{1+}, \tilde{x}_{2+})^2 \mathcal{L}(\tilde{x}_{1-}, \tilde{x}_{2-})^2}{\epsilon^4 f'_+(\tilde{x}_{1+}) f'_+(\tilde{x}_{2+}) f'_-(\tilde{x}_{1-}) f'_-(\tilde{x}_{2-})} \right], \tag{2.40}$$

where $\mathcal{L}(\tilde{x}_{1\pm}, \tilde{x}_{2\pm})$ is the proper length on the boundary between $\tilde{x}_{1\pm}$ and $\tilde{x}_{2\pm}$.

Finite temperature

Computing holographic entanglement entropy for inhomogeneous systems at finite temperature is a less trivial matter than the zero temperature case; we need to find a proper foliation of the BTZ black hole solution with a given metric on the boundary. While this procedure can be implemented in certain cases (as described below), we will use a different approach in the bulk of the chapter, in which we cut off the BTZ black hole spacetime with the same curvilinear UV cutoff used in the previous section. Although approximate, this approach allows us to use known results for geodesic lengths of entangling surfaces in the BTZ spacetime. This will allow us to avoid solving for potentially complicated geodesics that the bulk metrics from the exact treatment would yield.

Let us first outline the exact approach following the results in Ref. [66]. We begin by specifying an arbitrary static (1+1)d boundary metric on the $x-t$ plane:

$$ds_{\partial}^{2} = -h(x)dt^{2} + \frac{dx^{2}}{h(x)}. \tag{2.41}$$

Note that any (1+1)d static metric can be written this way, up to a spatial coordinate transformation. We can solve the resulting Dirichlet problem in the Fefferman-Graham gauge in terms of two undetermined constants, J and B. Assuming $J=0$ (to avoid a cross term in the metric), the resulting bulk metric is

$$ds^{2} = \frac{R^{2}dz^{2}}{z^{2}} + \frac{1}{z^{2}}\left[-h\left(1+\frac{R^{2}}{16}\frac{h'^{2}-B^{2}}{h}z^{2}\right)^{2}dt^{2} + \frac{1}{h}\left(1+\frac{R^{2}}{4}h''z^{2} - \frac{R^{2}}{16}\frac{h'^{2}-B^{2}}{h}z^{2}\right)^{2}dx^{2}\right]. \tag{2.42}$$

For $h(x)=1$, the above reduces to the Fefferman-Graham form of the BTZ metric[82] with a horizon at $z_{H}=4/RB$. The parameter B thus corresponds to temperature in the boundary CFT.

For a more general $h(x)$, a more interesting horizon will be present. For example, if we start with the AdS_2 boundary metric (2.8) making the coordinate change $x=1/\eta$ puts the metric in the form of (2.41) with $h(x)=x^{2}$ (here we set the curvature scale h in (2.8) to be 1 for simplicity). Plugging this into (2.42) and transforming back to the original η coordinate gives us the following bulk solution:

$$ds^{2} = \frac{dz^{2}}{z^{2}} + \frac{1}{z^{2}\eta^{2}}\left[\left(1+R^{2}(1+B^{2}\eta^{2})z^{2}\right)^{2}d\eta^{2} - \left(1+R^{2}(1-B^{2}\eta^{2})z^{2}\right)^{2}dt^{2}\right], \tag{2.43}$$

which appears to have an interesting horizon at $z=1/(R\sqrt{B^{2}\eta^{2}-1})$. Note that as $z\to 0$, we see our bulk metric reduce to the AdS_2 foliation that we expect from the rainbow chain dual.

Computing the entanglement entropy would entail picking two boundary points, η_1 and

η_2, on a fixed time slice of (2.43), and computing the length of the spacelike geodesic between them. This would of course require a UV cutoff, which we would choose to be a constant $z = \epsilon$. Solving the Euler-Lagrange equations for the spacelike geodesics of (2.43) is nontrivial, and will be different for each inhomogeneous system of interest. It is for this reason that we use the approximate approach in this chapter.

This approximation for finding the finite temperature entanglement entropy in inhomogeneous systems requires two inputs. The first is the well-known result for the finite temperature holographic entanglement entropy[80], which in Poincaré coordinates takes the form

$$S_A^{holo}(x_1, x_2; \beta) = \frac{c}{3} \log \left[\frac{\beta}{\pi \sqrt{\epsilon_1} \sqrt{\epsilon_2}} \sinh \left(\frac{\pi (x_2 - x_1)}{\beta} \right) \right]. \tag{2.44}$$

For reference, in Poincaré coordinates the BTZ black hole metric is

$$ds^2_{BTZ} = R^2 \left[-\frac{f(z) dt^2}{z^2} + \frac{dz^2}{f(z) z^2} + \frac{dx^2}{z^2} \right], \quad f(z) = 1 - \frac{z^2}{z_H^2}, \tag{2.45}$$

where z_H is related to the inverse temperature β at the boundary via $\beta = 2\pi z_H$.

With (2.44) in hand, we can add the second ingredient, and replace ϵ_1 and ϵ_2 with appropriate curvilinear cutoffs. As in the previous subsection, we can find these cutoffs from the bulk coordinate change that produced our zero temperature foliation. We should emphasize, however, that the use of these same UV cutoffs is the core of the approximation. In the BTZ spacetime, the cutoff surfaces will not exactly reproduce a 2D theory with the desired curved metric, as the presence of the black hole will distort the intrinsic geometry of the cutoff surfaces as the cutoff surface moves closer to the horizon. Far away from the horizon, however, the geometry of the boundary theory will be very close to the zero temperature geometry, and our approximation (2.44) will remain valid. More specifically, if we transform spatial coordinates from x and z to u and v according to $x = x(u, v)$

and $z = z(u, v)$, where u is our new radial coordinate, the following must be true for our approximation to hold:

$$z(u = \epsilon, v) \ll z_H. \tag{2.46}$$

This condition ensures that our UV cutoff surface avoids the black hole horizon. For high temperatures and/or large entanglement intervals, the cutoff surface becomes distorted by the black hole, and eventually crosses the horizon. Keeping the boundary interval and the temperature sufficiently small, however, ensures the validity of our approximation in estimating the entanglement entropy at finite temperature.

Combining (2.37) and the coordinate transformations on the boundary with (2.44) yields a result for the finite temperature bipartite entanglement entropy in an inhomogeneous CFT:

$$S_A^{holo}(v_1, v_2; \beta) = \frac{c}{3} \log \left[\frac{\beta}{\pi \epsilon} \frac{\sinh\left(\frac{\pi}{\beta}(x(u = 0, v_2) - x(u = 0, v_1))\right)}{\sqrt{\frac{\partial z(u=0,v_1)}{\partial u} \frac{\partial z(u=0,v_2)}{\partial u}}} \right].$$

The above can be considered our finite temperature master formula for entanglement entropy, and we will use it throughout the chapter. The limitations of (2.47) will be apparent when discussing high temperatures or large subsystem sizes. For most of the physics in which we are interested, however, (2.46) will hold and the formula will agree quite well with numerics.

2.2.3 CFT on curved spacetime

The connection between the entanglement scaling of inhomogeneous and homogeneous CFTs can be also seen without using holography. Recall that the entanglement entropy for a single interval is given by the 2-point function of twist operators located at two points u_1 and u_2 at a fixed time. Let us consider the correlators of arbitrary operators, $O_i(x_i)$, of CFT put on the flat Euclidean metric $ds_0(x)^2 = dx^2 + d\tau^2$, and the correlators of the same CFT put on the curved metric

$$ds^2 = e^{2\sigma(x)} ds_0^2 = e^{2\sigma(x)} d\bar{z}dz = e^{2\sigma(x(u))} \left[\left(\frac{dx}{du} \right)^2 du^2 + d\tau^2 \right], \tag{2.47}$$

where $z = x + i\tau$ and u is a spatial coordinate appropriate for the curved metric. CFT gives us the following relationship between correlation functions under Weyl and coordinate transformations:

$$\begin{aligned} &\langle O_1(u_1) O_2(u_2) \cdots \rangle_{ds^2} \\ &= e^{-\sum_i \Delta_i \sigma(u_i(x_i))} \langle O_1(x_1) O_2(x_2) \cdots \rangle_{ds_0(x)^2} \\ &= e^{-\sum_i \Delta_i \sigma(u_i)} \langle O_1(u_1) O_2(u_2) \cdots \rangle_{ds_0(u)^2}, \end{aligned} \tag{2.48}$$

where Δ_i are the scaling dimensions of the operators, which for the n-fold twist operators are

$$\Delta^{(n)} = \frac{c}{12} \left(n - \frac{1}{n} \right). \tag{2.49}$$

Since $ds_0(x)^2$ is just the Euclidean metric, we can write down the known result for the two-point function of the twist operators at a fixed time (assuming we are on the infinite complex plane):

$$\mathrm{Tr}\,(\rho_A^n)\big|_{ds_0^2} = \langle \sigma_n(x_1, \tau = 0) \sigma_{-n}(x_2, \tau = 0) \rangle_{ds_0^2} = c_n \left[\frac{x_1 - x_2}{\epsilon} \right]^{-2\Delta^{(n)}}, \tag{2.50}$$

where c_n is a constant coefficient that will make an $\mathcal{O}(1)$ contribution to the entanglement entropy. The (Renyi) entanglement entropy in the curved background follows from this expression by multiplying the Weyl factor and transforming back to the original coordinates.

2.3 Holographic dual of the rainbow chain

We now discuss the holographic dual of the rainbow chain, (2.19), in some detail. In particular, we study the entanglement entropy for a given connected region A of the boundary. As the system is inhomogeneous, not only the size of the subregion, but also its location matters. Here, we mainly consider two situations:

- "Defect entanglement": where we consider an entangling cut that separates the origin ("defect") from the rest of the system.
- "Half chain entanglement": where we consider an entangling cut that emanates from the origin (defect). This entangling cut thus splits the original system into two halves.

In addition, both of these two situations can be studied at finite temperature.

2.3.1 Defect entanglement at zero temperature

Let us first discuss the defect entanglement. Recall the metric (2.19) for the AdS foliation. We choose, in the Poincare coordinates, $x \in [-\eta_0, +\eta_0]$ on the boundary as the region of our interest. The geodesic Γ anchored at $(\eta, \Theta) = (\eta_0, \pm\pi/2h)$ is a semi-circle on the z-x plane, i.e., $\eta(\Theta) = const. = \eta_0$. The length of Γ, $Len(\Gamma) = \int_\Gamma ds$, is given by

$$Len(\Gamma) = hR \int_{-\pi/2h}^{\pi/2h} \frac{d\Theta}{\cos(h\Theta)} \sqrt{1 + \frac{1}{h^2\eta^2}\left(\frac{d\eta}{d\Theta}\right)^2}. \tag{2.51}$$

This integral is divergent, and one has to introduce a cutoff, $\pm\pi/2h \to \pm(\pi/2h - \epsilon)$, where ϵ is an η-independent constant. The regularized length is a constant independent of η_0 (i.e., independent of the size of the subsystem):

$$S_A(\eta_0) = \frac{c}{3} \log\left(\frac{2}{\epsilon h}\right) + \mathcal{O}(1), \tag{2.52}$$

This agrees with the known behavior of the defect entanglement entropy in the rainbow chain. It does, however, depend on $1/h$, the length scale introduced by the rainbow defect (i.e., the AdS_2 radius). One can check that this is the same result we would have obtained using (2.36).

The "defect entanglement" (2.52) we have just encountered resembles the constant "boundary entanglement" found in a BCFT. The latter, however, is an $\mathcal{O}(1)$ constant correction to the logarithmically divergent leading order term, whereas the defect entanglement is constant, but $\mathcal{O}(\log(\epsilon))$. Indeed, in $AdS/BCFT$, a zero tension brane anchored at a boundary point of AdS_3 is dual to a half-space BCFT on the conformal boundary of the spacetime. [74] This particular $AdS/BCFT$ setup strongly resembles our effective holographic description of the rainbow chain, and indeed, AdS_2 foliation of the bulk captures the breakdown of the global symmetry group from $SO(2,2)$ to $SO(2,1)$. However, a zero tension brane (which is just an artifact of a coordinate transformation) yields zero boundary entropy, and the defect entanglement simply reflects the contributions of the ends of our entanglement interval to the entropy. A boundary entropy would reflect the entropy due to the presence of a tensionful brane. Adding such a brane could prove to be an interesting extension of the rainbow chain.

2.3.2 Defect entanglement at finite temperature

We can bring this metric back to the one we want to work with, Eq. (2.18). For reference, the geodesic in these coordinates takes the form

$$\sqrt{1-\frac{\eta^2\cos^2(h\Theta)}{z_H^2}}=\sqrt{1-\frac{z_*^2}{z_H^2}}\cosh\left[\frac{\eta\sin(h\Theta)}{z_H}\right]. \tag{2.53}$$

In Fig. 2.2, we have plotted the geodesic for several values of z_* in blue, with the black hole horizon plotted in red. We will cut our spatial slice off at a constant $\Theta_\epsilon = \pi/2h - \epsilon$.

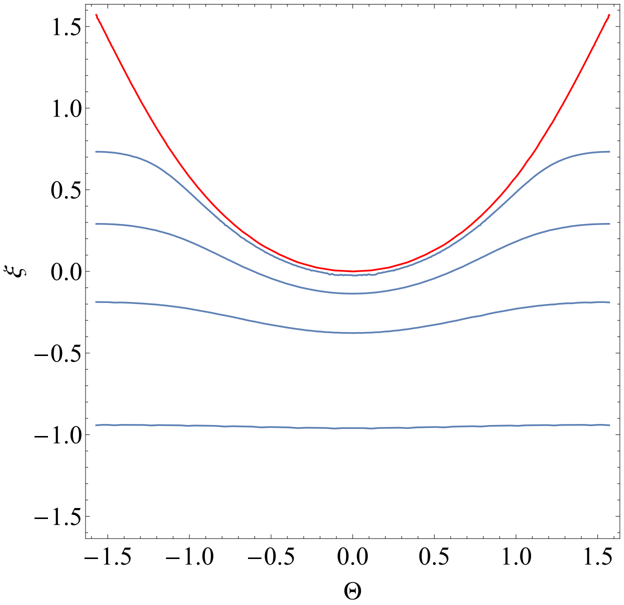

Figure 2.2: The black hole horizon (red) and several defect-crossing geodesics (blue) plotted in ξ and Θ coordinates where $d\xi/\cos\xi = d\eta/\eta$ (see Eq. (2.59)).

Expressed as a cutoff in the z coordinate, the cutoff now depends on $x_0 = \eta_0$ as follows:

$$\epsilon_z = \eta_0 \cos(h\Theta_\epsilon) \approx \eta_0 h\epsilon. \tag{2.54}$$

Thus, using our master formula, (2.47), our defect entanglement entropy reduces to

$$S_A(\eta_0;\beta) = \frac{c}{3}\log\left[\frac{\beta}{\pi\epsilon h\eta_0}\sinh\left(\frac{2\pi\eta_0}{\beta}\right)\right]. \tag{2.55}$$

Taking the zero temperature limit, $\beta \to \infty$, we recover (2.52). The proper length of the boundary interval

$$\ell = \frac{2}{h}\int_\epsilon^{\eta_0}\frac{d\eta}{\eta}. \tag{2.56}$$

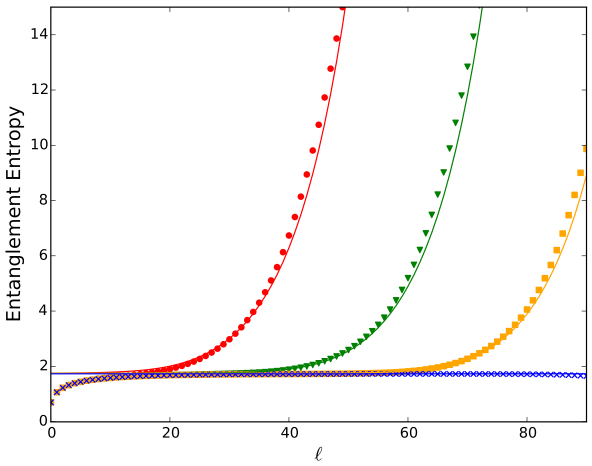

Figure 2.3: The numerically computed "defect" entanglement entropy as a function of the proper length of the interval about the defect at $h = 0.1$ and $\epsilon = 0.5$ and at finite temperatures $\beta = 100, 1000, 10000, \infty$ from the top. The numerical data are fitted to (2.57), where we treat the non-universal constant part (independent of ℓ and β) as a fitting parameter. The numerics were done with free fermions on a lattice of 200 sites.

In terms of the proper length, the defect entanglement entropy is :

$$S_A(x;\beta,\epsilon) = \frac{c}{3}\log\left[\frac{\beta}{\pi h e^{h\ell}}\sinh\left(\frac{2\pi\epsilon e^{h\ell}}{\beta}\right)\right] + \cdots , \tag{2.57}$$

where $\cdots$ is a non-universal part depending on the UV cutoff.

Comparison with numerics To verify the finite temperature entanglement results for the rainbow chain, we can numerically compute the entanglement entropy of an interval of space at a given temperature for the Hamiltonian (2.4). All numerical computations were done with open boundary conditions. In Fig. 2.3 we have plotted the numerically-computed entanglement entropy for an interval symmetric about the defect at the origin of the chain. We can confirm the rapid asymptote at zero temperature of this entropy to a constant, independent of the length of the interval, but dependent upon h, the rainbow curvature scale. Also plotted in Fig. 2.3 is the defect entanglement for several different temperatures, fitted with the analytic result (2.57).

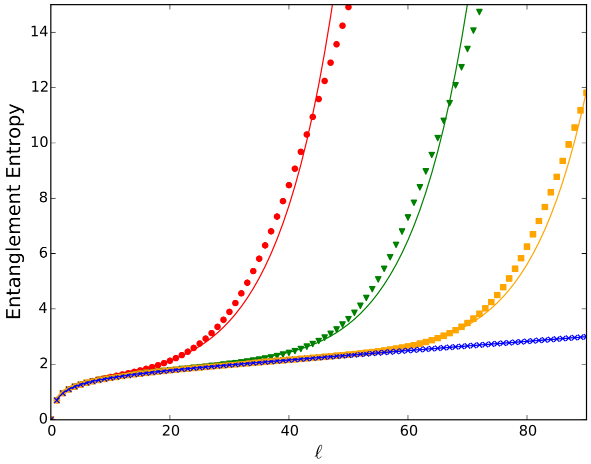

Figure 2.4: The numerically computed “half-chain” entanglement entropy at finite temperature at $h = 0.1$ for $\beta = 100, 1000, 10000, \infty$ from the top. The numerical data is fitted to Eq. (2.62), where we treat the non-universal constant part (independent of ℓ and β) as a fitting parameter. The numerics were done with free fermions on a lattice of 200 sites.

2.3.3 Half-chain entanglement at zero temperature

Let us now discuss the half-chain entanglement. For this purpose, it is convenient to use the global coordinate:

$$ds^2_{AdS_3} = \frac{h^2 R^2}{\cos^2(h\Theta)} \left(d\Theta^2 + ds^2_{AdS_2} \right), \tag{2.58}$$

where $ds^2_{AdS_2}$ is the metric of AdS_2 which will be described below. There are two asymptotic boundaries located at $\Theta = \pm\pi/2h$, where two CFTs, one for each boundary, are defined. As for $ds^2_{AdS_2}$, it is also given in terms of the global coordinate

$$ds^2_{AdS_2} = \frac{1}{h^2 \cos^2 \xi} (-d\tau^2 + d\xi^2), \tag{2.59}$$

$\tau \in (-\infty, +\infty)$ and $\xi \in (-\pi/2, \pi/2)$. There are two asymptotic boundaries at $\xi = \pm\pi/2$. The two CFTs are connected at the boundaries of AdS_2.

Combining the coordinate transformation (2.18) with (2.36), we obtain the half-chain entanglement entropy. We can express this in terms of the proper length via $\ell = \frac{1}{h}\int_{\eta_1}^{\eta_2}\frac{d\eta}{\eta} \rightarrow \eta_2 = \eta_1 \exp(h\ell)$:

$$S_A(\ell) = \frac{c}{3}\log\left[\frac{2}{\epsilon h}\sinh\left(\frac{h\ell}{2}\right)\right]. \tag{2.60}$$

The most striking feature about this zero temperature result is that it demonstrates a volume law growth for larger values of ℓ, with h acting as an effective temperature. This is consistent with results from previous work on the rainbow chain,[30, 31] where it was found that the rainbow phase strongly resembles a thermofield double state.

2.3.4 Half-chain entanglement at finite temperature

We can apply the same procedure of cutting off the geodesics in the BTZ spacetime at $\epsilon_z = \eta_{1,2}h\epsilon$. Here, we consider a geodesic anchored at arbitrary $\Theta = \pi/2h$ boundary points η_1 and η_2, where $\eta_2 > \eta_1$. Combining these cutoffs with our finite temperature master formula (2.47) yields

$$S_A(\eta_1, \eta_2; \beta) = \frac{c}{3}\log\left[\frac{\beta}{\epsilon\pi h\sqrt{\eta_1\eta_2}}\sinh\left(\frac{\pi(\eta_2 - \eta_1)}{\beta}\right)\right]. \tag{2.61}$$

In terms of the proper length ℓ, the half-chain entanglement is

$$S_A(\ell; \beta, \eta_1) = \frac{c}{3}\log\left[\frac{\beta}{\epsilon\pi h\eta_1 e^{h\ell/2}}\sinh\left(\frac{\pi\eta_1(e^{h\ell} - 1)}{\beta}\right)\right]. \tag{2.62}$$

The low temperature $\beta \rightarrow \infty$ limit agrees with (2.60).

We have also computed numerical results for the half-chain entanglement in Fig. 2.4, using the lattice model (2.4) with the hopping amplitudes (2.5). There, we choose two points η_1 and η_2, both located to the right of the defect, and set $\eta_1 = 12$ and increase ℓ by changing η_2. We use ℓ rather than the coordinates (2.7) We can see that the agreement between the numerical and holographic results is excellent at low temperatures.

2.4 Holographic dual of SSD

2.4.1 Zero temperature

Now let us compute the holographic entanglement entropy of the SSD at zero temperature using the metric (2.22). Let us first consider an interval $[v_1, v_2]$ (where $0 \leq v_1, v_2 \leq 2\pi$). Cutting off at $u = \epsilon$ corresponds to a $v-$dependent z cutoff of $\epsilon_z = \frac{a\epsilon}{1-\cos(v)}$. Using (2.36) and the above cutoff, we find that the zero temperature entanglement entropy is

$$S_A(v_1, v_2) = \frac{c}{3} \log \left[\frac{2}{\epsilon} \sin \left(\frac{1}{2} |v_2 - v_1| \right) \right]. \tag{2.63}$$

The result (2.63) is just the entanglement entropy for a CFT on a finite length space with periodic boundary conditions and is what we expect from the SSD model.[36]

The above holographic results can be readily reproduced by a CFT calculation. The metric on our conformal boundary ($u = 0$) in imaginary time, τ, is

$$ds^2 = dv^2 + \frac{4}{a^2} \sin^4 \left(\frac{v}{2} \right) d\tau^2. \tag{2.64}$$

We factor out the $\frac{4}{a^2} \sin^4 \left(\frac{v}{2} \right)$ and define a new variable

$$dx = \frac{a dv}{2 \sin^2 \left(\frac{v}{2} \right)} \longrightarrow x = -a \cot \left(\frac{v}{2} \right) \tag{2.65}$$

to write our metric as

$$ds^2 = e^{2\sigma} ds_0^2, \quad e^{\sigma} = \frac{2}{a} \sin^2 \left(\frac{v}{2} \right) = \frac{2a}{a^2 + x^2}, \tag{2.66}$$

where $ds_0^2 = dx^2 + d\tau^2$. Since $x \in (-\infty, \infty)$, we can use the twist 2-point function on the full complex plane to compute the entanglement entropy (2.50). Then,

$$
\begin{aligned}
&\mathrm{Tr}\,(\rho_A^n)\big|_{ds^2}\\
&= c_n e^{-\Delta^{(n)}[\sigma(u_1)+\sigma(u_2)]}\left[\frac{a\cot\left(\frac{v_2}{2}\right)-a\cot\left(\frac{v_1}{2}\right)}{\epsilon}\right]^{-2\Delta^{(n)}}\\
&= c_n\left[2\sin\left(\frac{1}{2}\left(v_2-v_1\right)\right)\right]^{-2\Delta^{(n)}}. \qquad (2.67)
\end{aligned}
$$

Taking the log and taking $n \to 1$, we reproduce the holographic result (2.63).

2.4.2 Finite temperature

We can once again use the cutoff $\epsilon_z = \frac{a\epsilon}{1-\cos(v)}$. This time we will plug it into (2.47) in order to obtain finite temperature results for the SSD. For the interval $[v_1, v_2]$, we obtain the following entanglement law:

$$
\begin{aligned}
S_A(v_1, v_2; \beta) &= \frac{c}{3}\log\left[\frac{2}{a}\sin\left(\frac{v_1}{2}\right)\sin\left(\frac{v_2}{2}\right)\right]\\
&+\frac{c}{3}\log\left[\frac{\beta}{\pi\epsilon}\sinh\left(\frac{\pi a}{\beta}\frac{\sin\left(\frac{1}{2}(v_2-v_1)\right)}{\sin\left(\frac{v_1}{2}\right)\sin\left(\frac{v_2}{2}\right)}\right)\right]. \qquad (2.68)
\end{aligned}
$$

We can confirm that at zero temperature, $S_A(v_1, v_2; \beta \to \infty)$ agrees with the result from the previous section (2.63). Note, unlike the zero temperature result (2.63), (2.68) depends on a. If we center the interval about π, so that $v_1 = \pi - v_0$ and $v_2 = \pi + v_0$ (where $v_0 \in [0, \pi)$),

$$
\begin{aligned}
&S_A(\pi - v_0, \pi + v_0; \beta)\\
&= \frac{c}{3}\log\left[\frac{2\beta}{\pi a\epsilon}\cos^2\left(\frac{v_0}{2}\right)\sinh\left(\frac{2\pi a}{\beta}\tan\left(\frac{v_0}{2}\right)\right)\right]. \qquad (2.69)
\end{aligned}
$$

For comparison with the SSD model put on a line of finite length L, we rescale $v_i \to x_i = Lv_i/2\pi$ and recall that the parameter a and L are related by (2.25), $a = L/2\pi$. The

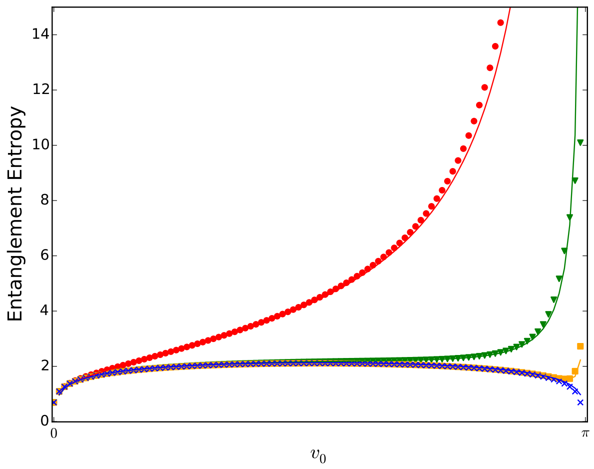

Figure 2.5: Finite temperature entanglement entropy in the SSD model, for an interval centered about $v = \pi$, and for $\beta = 10, 100, 1000, \infty$ (from top to bottom). The dotted plots are numerical results from exact diagonalization and solid lines are the fitted analytic result (2.71) where we treat the non-universal constant part (independent of v_0 and β) as a fitting parameter. The numerics were done with free fermions on a lattice of 200 sites.

entanglement entropy is then given by

$$\begin{aligned} S_A(x_1, x_2; \beta) &= \frac{c}{3} \log \left[\frac{4\pi}{L} \sin\left(\frac{x_1}{\pi}\right) \sin\left(\frac{x_2}{\pi}\right) \right] \\ &+ \frac{c}{3} \log \left[\frac{\beta}{\pi\epsilon} \sinh\left(\frac{L}{2\beta} \frac{\sin\left(\frac{1}{\pi}(x_2 - x_1)\right)}{\sin\left(\frac{x_1}{\pi}\right)\sin\left(\frac{x_2}{\pi}\right)} \right) \right] . \end{aligned} \tag{2.70}$$

Once again, if we center the interval about π, so that $v_1 = \pi - v_0$ and $v_2 = \pi + v_0$ (where $v_0 \in [0, \pi)$),

$$\begin{aligned} &S_A(\pi - v_0, \pi + v_0; \beta) \\ &= \frac{c}{3} \log \left[\frac{4\beta}{L\epsilon} \cos^2\left(\frac{v_0}{2}\right) \sinh\left(\frac{L}{\beta} \tan\left(\frac{v_0}{2}\right) \right) \right] . \end{aligned} \tag{2.71}$$

In Fig. 2.5 we have plotted the entanglement entropy for several values of β, computed numerically from the Hamiltonian (2.4) with

$$f_j = \frac{2}{a}\sin^2\left(\frac{j\pi}{N}\right) = \frac{4\pi}{N-1}\sin^2\left(\frac{j\pi}{N}\right). \tag{2.72}$$

Here, we put the over all factor $2/a = 4\pi/(N-1)$ since the boundary metric of our holographic setup is not ds^2_{Mobius} itself, but ds^2_{Mobius} multiplied by the factor $(\cosh 2\gamma/a)^2 \to (2/a)^2$; See Eq. (2.11). The N-dependent multiplicative factor serves to compress the density of states of the SSD model. This quantity only becomes relevant to the entanglement entropy at finite temperature, as higher energy states become populated.

2.4.3 Dipolar limit

The dipolar limit of our holographic SSD model (2.29) can be studied analogously to the holographic duals of the rainbow and SSD models.

Zero temperature A geodesic in these coordinates terminates at $u = 0$, $v_0 = -1/x_0$, where $x_0 = x(z = 0)$ is the anchor point of the geodesic in the original Poincaré coordinates. We introduce a UV cutoff ϵ in the radial, u-direction. In terms of the boundary anchor point, the z coordinate cutoff is

$$\epsilon_z = \frac{a\epsilon}{v_0^2 + \epsilon^2} \approx \frac{a\epsilon}{v_0^2}. \tag{2.73}$$

Using (2.36) we have the following entanglement entropy:

$$S_A(v_0) = \frac{c}{3}\log\left(\frac{2v_0}{a\epsilon}\right). \tag{2.74}$$

As we can see, the holographic entanglement entropy is unchanged by the dipolar coordinate transformation in the bulk time slice.

The holographic result (2.74) can be readily reproduced from CFT calculations. From the previous subsection, we saw that the conformal boundary of the Poincaré metric in $u-v$ coordinates has the following metric:

$$ds^2 = -a^{-2}v^4dt^2 + dv^2. \tag{2.75}$$

Switching to imaginary time, τ, and defining $x = -1/v$, or metric can be written as a Weyl-transformed flat metric in the $x-\tau$ coordinates, $ds^2 = e^{2\sigma(x)}ds_0^2 = e^{2\sigma(x)}d\bar{z}dz$ where $z = x + i\tau$ and

$$e^{2\sigma(x)} = a^{-2}v^4 = \frac{1}{a^2x^4}. \tag{2.76}$$

Using (2.48) as before, we can compute the correlator on this particular curved background:

$$\mathrm{Tr}\,(\rho_A^n)|_{ds^2} = c_n e^{-\Delta^{(n)}[\sigma(v_1)+\sigma(v_2)]}\left[\frac{1}{a\epsilon v_1} - \frac{1}{a\epsilon v_2}\right]^{-2\Delta^{(n)}} = c_n\left[\frac{a\epsilon}{v_2 - v_1}\right]^{-2\Delta^{(n)}}. \tag{2.77}$$

Taking the log, multiplying by the appropriate factor, and taking the replica limit $n \to 1$, we recover (2.74).

Finite temperatures As for the entanglement entropy at finite temperatures, plugging the v_0-dependent, constant u, cutoff, $\frac{\epsilon}{v_0^2}$ into (2.47), we have

$$S_A = \frac{c}{3}\log\left[\frac{\beta v_0^2}{\pi a\epsilon}\sinh\left(\frac{2\pi a}{\beta v_0}\right)\right], \tag{2.78}$$

which at any temperature, $1/\beta$, asymptotes to the same logarithmic growth for large values of v_0. For generic endpoints, v_1 and v_2, we have

$$S_A = \frac{c}{3}\log\left[\frac{\beta|v_1v_2|}{2\pi a\epsilon}\sinh\left(\frac{2\pi a}{\beta}\left|\frac{v_2 - v_1}{v_1v_2}\right|\right)\right]. \tag{2.79}$$

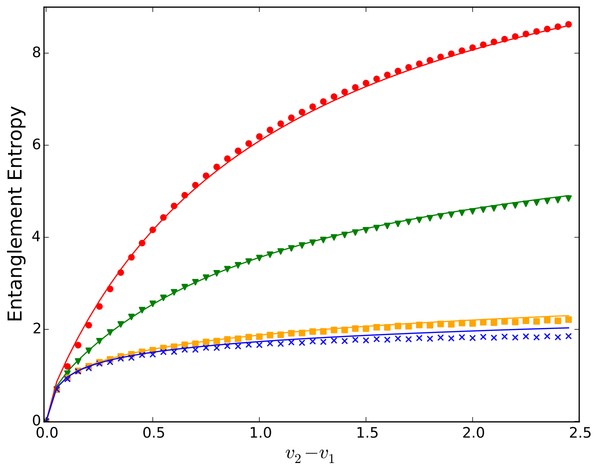

Figure 2.6: Finite temperature entanglement entropy for the boundary theory of the dipole-foliated AdS_3 for an interval starting at $v = 1.0$, for $\beta = 1, 2, 10, \infty$ (from top to bottom). The plots are fit to (2.79). where v_1 and v_2 are the left and right boundaries of the interval, respectively, c is the central charge, and b is a fitting parameter related to the lattice cutoff. This is just the small v limit of the function in Fig. 2.5. The numerics were done with free fermions on a lattice of 200 sites.

In Fig. 2.6, we compare (2.79) with numerical results obtained from the Hamiltonian (2.4) with $f_j = (10j/N - 5)^2$.

2.5 Application: Particles in a Potential Well

The entanglement properties of nonrelativistic free fermions trapped in a potential well $V(x)$ can be described by a $c = 1$ CFT on the following curved metric: [56]

$$ds^2 = dx^2 - v^2(x)dt^2 \tag{2.80}$$

where, using the local density approximation, $v(x)$ is given by the local density as $v(x) = \langle \rho(x) \rangle = \sqrt{\frac{2}{m}(\mu - V(x))}$ where μ is the chemical potential and m is the mass of non-relativistic fermions. [56, 83] This is a semiclassical approximation in which the potential couples directly to the energy density, allowing for an easy application of our methods. Similar methods were also used in Ref. [84] to study the density matrix of a 1D Tonks-

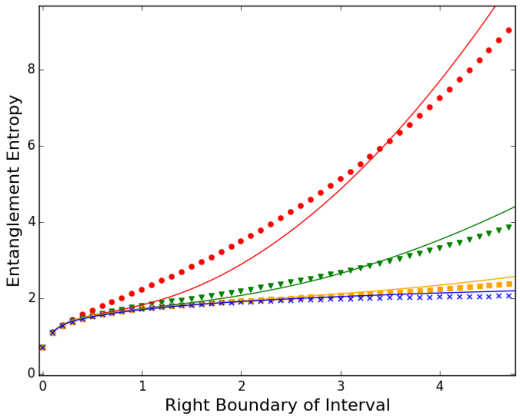

Figure 2.7: Numerically computed entanglement entropy for free fermions in a Lorentzian potential well plotted at various temperatures, $\beta = 10,\ 30,\ 100,\ \infty$ plotted in dotted lines. (2.84) Plotted for the same temperatures in continuous lines. The numerics were performed on a lattice of 200 sites.

Girardeau gas. Once we have this metric, we are implicitly using this approximation, and are no longer dealing directly with the nonrelativistic fermionic system. Henceforth, we use (2.80) as our starting point for numerical and holographic calculations. Our holographic results are therefore not compared directly with the trapped fermion system, only with free fermions on the curved background given by (2.80).

Starting with the Poincaré metric on AdS_3, $ds^2_{AdS_3} = \frac{1}{z^2}\left[dz^2 + dy^2 - dt^2\right]$, we can induce the metric (2.80) on the conformal boundary with the appropriate coordinate transformation

$$z = \frac{u}{v(x)}, \quad y = \int^x \frac{dx'}{v(x')}. \tag{2.81}$$

To leading order near the $u = 0$ conformal boundary, our Poincaré metric takes the form

$$ds^2 = \frac{1}{u^2}\left[du^2 + dx^2 - v(x)^2 dt^2\right] + \mathcal{O}(1) \tag{2.82}$$

Consider the example of a Lorentzian potential well, $V(x) = \frac{-1}{1+(x/a)^2}$, where a controls the width of the well. We will set $\mu = 0$. A lower chemical potential would result in an average particle density, $\langle \rho(x) \rangle$ that is zero outside of some finite region, requiring us to use BCFT methods. [83] (Note, μ is *not* the chemical potential in our relativistic fermion system; it is better thought of as an input parameter for our metric). Our new coordinates are thus defined by (setting $m = 2$ for convenience)

$$\begin{aligned} z &= u\sqrt{1+(x/a)^2}, \\ y &= \frac{1}{2}\left(x\sqrt{1+(x/a)^2} + a\sinh^{-1}(x/a)\right) + const. \end{aligned} \tag{2.83}$$

This coordinate transformation implies a radial bulk cutoff of $\epsilon_z = \epsilon\sqrt{1+(x/a)^2}$. The finite temperature entanglement entropy for an interval between $-x_0$ and x_0 is thus

$$S_A = \frac{c}{3}\log\left[\frac{\beta}{\pi\epsilon\sqrt{1+(x_0/a)^2}}\right] + \frac{c}{3}\log\left[\sinh\left(\frac{\pi}{\beta}\left(x_0\sqrt{1+(x_0/a)^2} + a\sinh^{-1}(x_0/a)\right)\right)\right]. \tag{2.84}$$

The zero temperature limit of (2.84) is

$$S_A = \frac{c}{3}\log\left(\frac{1}{\epsilon}\left(x_0 + \frac{a\sinh^{-1}(x_0/a)}{\sqrt{1+(x_0/a)^2}}\right)\right) \tag{2.85}$$

In Fig. 2.7 we have plotted (2.84) for several temperatures alongside numerical results for the Lorentzian well. The agreement is qualitatively quite good. The noticeable discrepancies are likely due to the limitations of the bulk transformation we have used, and the resulting $\mathcal{O}(1)$ contributions to the metric that we are ignoring. It should be noted once again that we have not directly simulated nonrelativistic fermions in a potential well; we have assumed that the metric (2.80) is a valid description of the physics in this potential, and simulated free fermions living on this background geometry.

2.6 Discussion

In this chapter we have used the Ryu-Takayanagi formula to compute the Von Neumann entropy for strongly interacting CFTs on curved backgrounds, both at zero and finite temperature. We have seen dramatic, global changes in entanglement structure resulting from local deformations in background geometry. An interesting next step would be to use this method to probe multipartite measures of entanglement (e.g. tripartite negativity) that are computable in holography. Another interesting direction would be to introduce quasi-periodic background geometries in order to simulate disorder, to see if this results in any sort of localization.

CHAPTER 3

LOCAL PROBES OF ENTANGLEMENT AND THE ENTANGLEMENT CONTOUR

3.1 Introduction

We have so far focused on computing bipartite measures of entanglement for subregions of larger systems. This is of course a worthwhile and interesting pursuit. Von Neumann entropy and similar measures have been used for characterizing quantum critical systems [85] and topological order [5, 6] and are key ingredients for understanding the emergence of bulk spacetime in gauge-gravity duality [11, 12, 86]. Furthermore, it is a useful probe of thermalization in many-body systems. The Von Neumann entropy is of course, though, a highly nonlocal quantity associated with an entire subregion of space (or codimension-1 subregion of spacetime, from a high energy physicist's perspective). Likewise, its holographic dual is the area, $\mathcal{A}$, of the extremal surface in the bulk that is homologous to the boundary subregion of interest [11, 12, 80]

$$S_{vN} = \frac{\mathcal{A}}{4G_N}. \tag{3.1}$$

It is interesting to ask about the finer structure of entanglement, and to seek a well-behaved quasi-local probe of the quantum correlations in a many-body system. This would act as a quantitative measure complementing the geometric picture of real space entanglement seen in tensor networks. For instance, a suitable fine-grained measure would show the dominance of the entropy for ground states of gapped Hamiltonians near the entangling surface, and a constant entropy density for thermal states. Progress on decomposing entropy into a fine-grained quantity was made with the introduction of the entanglement contour [87][1].

---

[1] We note that a similar construction was studied earlier in Ref. [88].

The entanglement contour at a point x in subregion A, $s_A(x)$, is non-uniquely defined through five conditions:

1. Positivity: $s_A(x) \geq 0 \quad \forall \quad x \in A$.

2. Normalization: $\int_A s_A(x) d^d x = S(A)$ where $S(A)$ is the von Neumann entropy of A.

3. Invariance under spatial symmetry transformations: If T is a symmetry of the reduced density matrix, ρ_A, that exchanges two sites $i, j \in A$, then $s_A(i) = s_A(j)$.

4. Invariance under local unitary transformations: If $\rho'_A = U_X \rho_A U_X^\dagger$, where U_X is a local unitary supported on $X \subseteq A$, then $s_A(X)$ is equal for both ρ_A and ρ'_A. Here,

$$s_A(X) = \int_X s_A(x) d^d x. \tag{3.2}$$

5. Upper bound: If $\mathcal{H}_A = \mathcal{H}_\Omega \otimes \mathcal{H}_{\bar{\Omega}}$ and $\mathcal{H}_X$ is contained within $\mathcal{H}_\Omega$, then

$$s_A(X) \leq S(\Omega). \tag{3.3}$$

It is an open program where more conditions may need to be defined. Contour functions have previously been constructed for free fermions, harmonic lattices, single intervals in 1+1d holographic CFTs, and 1+1d inhomogeneous critical systems [33, 87, 89–91], with each having a unique construction. We find that bit threads [92], an alternative description of holographic entanglement entropy, elucidate the non-uniqueness of the entanglement contour[2].

We organize the chapter as follows: In section 3.2, we unify the entanglement contour for generic 1+1d systems and compute the contour for a range of static systems with distinct entanglement structures, including thermal systems and defect CFTs. In section 3.3, we

---

[2] We also thank Erik Tonni for directing us to his slides from It from Qubit Bariloche where a connection between bit threads and the entanglement contour was originally discussed.

use bit threads to propose a holographic realization of the entanglement contour for any dimension and entangling surface geometry. In section 3.4, we tie together the notions of the entanglement contour, entanglement density, and bit threads with kinematic space. We then introduce dynamics in section 3.5 with both local and global quantum quenches. The contour proves to be particularly useful in characterizing non-equilibrium dynamics and clarifies the interpretation of the entanglement tsunami picture in ergodic CFTs [93–96]. The work in this chapter was derived from [97] and [98].

3.2 Entanglement contour for 1+1d systems

In order to construct an entanglement contour for generic quantum systems, let us partition a subregion A into n degrees of freedom $\{A_i\}$. The entropy of A can be expanded in terms of conditional entropies

$$S(A) = \frac{1}{2}\sum_{i=1}^{n}\Big[S(A_i|A_1\cup\cdots\cup A_{i-1}) + S(A_i|A_{i+1}\cup\cdots\cup A_n)\Big], \tag{3.4}$$

where conditional entropy is defined as

$$S(A|B) = S(A\cup B) - S(B). \tag{3.5}$$

For conciseness, we replace the first and last terms of (3.4), $S(A_1|A_1)$ and $S(A_n|A_n)$, with $S(A_1)$ and $S(A_n)$, respectively. This leads us to a natural entanglement contour

$$s_A(A_i) = \frac{1}{2}\Big[S(A_i|A_1\cup\cdots\cup A_{i-1}) + S(A_i|A_{i+1}\cup\cdots\cup A_n)\Big]. \tag{3.6}$$

We stress that this choice of a contour function is not the only function that may satisfy the requirements. Technically, this is an entanglement contour for any dimension, though for higher dimensions there will be an ambiguity regarding the ordering of $\{A_i\}$. Therefore, we restrict our current focus to 1+1d systems and return to higher dimensions in Section 3.3. In [90], an entanglement contour was proposed for single intervals in 1+1d holographic CFTs

$$s_A(A_2) = \frac{1}{2}\left[S(A_1 \cup A_2) + S(A_2 \cup A_3) - S(A_1) - S(A_3)\right], \tag{3.7}$$

where $A_1 \cup A_2 \cup A_3 = A$. This was derived using natural slicings of the Ryu-Takayanagi surface arising from the bulk extension of the modular flow. (3.6) generalizes this formula to multiple intervals and generic quantum systems. We will now prove that (3.6) satisfies all five conditions for an entanglement contour completely generally, without any reference to holography or quantum field theory.

1. Positivity: This follows directly from the strong subadditivity of von Neumann entropy [99].

2. Normalization: By construction, normalization is satisfied.

3. Symmetry: We take a spatial symmetry that exchanges $i, j \in A$, $T\rho^A T^\dagger = \rho^A$. Each component of (3.6) is invariant under such a transformation, so $s_A(i) = s_A(j)$.

4. Invariance under local unitary transformations: As stated in [90], the causal property of entanglement entropy ensures that all components of (3.6) are stationary under unitaries acting nontrivially only on A_i.

5. Upper bound: We take a subregion $A_2 \subset A$ that is contained in a factor space Ω_A. We must then prove that $s_A(A_2) \leq S(\Omega_A)$. By the additivity of the contour and subadditivity of von Neumann entropy,

$$s_A(A_2) \leq s_A(\Omega_A) \leq S(\Omega_A). \tag{3.8}$$

3.2.1 Static examples

We reproduce results derived in [90, 100], so that we can refer to them later on. For the vacuum, the contour for the 1+1d subinterval, $(-l/2, l/2)$, is

$$s_A(x) = \frac{c}{6}\left(\frac{l}{\frac{l^2}{4} - x^2}\right) \tag{3.9}$$

and for a thermal state with inverse temperature β,

$$s_A(x) = \frac{c\pi}{6\beta}\left(\coth\left(\frac{\pi(x+\frac{l}{2})}{\beta}\right) + \coth\left(\frac{\pi(\frac{l}{2}-x)}{\beta}\right)\right). \tag{3.10}$$

It was also shown in [100] that for the warped CFT dual to AdS_3 with chiral boundary conditions [101],

$$s_A(x) = \frac{c}{12}\left(1 + \frac{l}{\frac{l^2}{4} - x^2}\right). \tag{3.11}$$

Interestingly, this is identical to the regular CFT result with an additional "thermal" term.

Defect CFTs

Using a simplified version of the Randall-Sundrum model, we can model the holographic dual of a defect CFT (dCFT) as two copies of AdS_3 with a deficit angle [73, 102] with the metric

$$ds^2 = d\rho^2 + \cosh^2 \frac{\rho}{l_{AdS}}\left(\frac{dy^2 - dt^2}{y^2}\right). \tag{3.12}$$

Above, l_{AdS} is the AdS curvature radius, ρ is the radial coordinate (with asymptotic boundaries at $\rho = \pm\infty$), and y is the transverse spatial coordinate. The two copies of the deficit angle AdS are glued together at a tensionful brane, which models the defect. For a brane of tension λ, the radial coordinate ρ ranges between $-\infty$ and

$$\rho_* = l_{AdS} \tan^{-1}(l_{AdS}\lambda). \tag{3.13}$$

To consider the dCFT, we double the domain by attaching $\rho \in (-\rho_*, \infty)$. Using (3.6), we find

$$s_A(x) = \frac{c}{6}\left(\frac{l}{\frac{l^2}{4} - x^2} + \rho_* \delta(x)\right). \tag{3.14}$$

Naturally, all of the boundary entropy is localized on the defect brane.

Black hole microstates

Black hole microstates are dual to high-energy eigenstates of the CFT, which can be formed by the operator-state mapping of local heavy operators, ψ, with conformal dimensions $h_\psi = \bar{h}_\psi$. The entanglement entropy is calculated by the four-point function

$$S_\psi(x_1, x_2) = \lim_{n\to 1} \frac{1}{1-n} \log \langle\psi|\, \sigma_n(x_1)\bar{\sigma}_n(x_2)\, |\psi\rangle\,. \tag{3.15}$$

Leveraging progress in the calculation of conformal blocks for "heavy-heavy-light-light" correlation functions [103], the entropy is found to be [104, 105]

$$S_A = \frac{c}{3} \log\left(\frac{\beta_\psi}{\pi\epsilon} \sinh\left(\frac{l\pi}{\beta_\psi}\right)\right), \tag{3.16}$$

where l is the length of the interval and β_ψ is an effective temperature

$$\beta_\psi = \frac{2\pi}{\sqrt{24h_\psi/c - 1}}. \tag{3.17}$$

We then find the entanglement contour for the high-energy eigenstate

$$s_A(x) = \frac{c\pi}{6\beta_\psi}\left(\coth\left(\frac{\pi x}{\beta_\psi}\right) + \coth\left(\frac{\pi(l-x)}{\beta_\psi}\right)\right), \tag{3.18}$$

analogous to a truly thermal state. While these states clearly obey the Eigenstate Thermalization Hypothesis [106], the contour may be particularly useful for understanding systems whose eigenstates do not thermalize, e.g. many-body localized phases and scar states [107].

Massive deformation

We perturb our CFT by a massive deformation as was done in [11, 12]. This is crudely done by capping off the bulk IR geometry with characteristic correlation length ξ. For small intervals, we still have the critical vacuum entropy

$$S = \frac{c}{3}\log\frac{l}{a}, \tag{3.19}$$

but for large intervals,

$$S = \frac{c}{3}\log\frac{\xi}{a}. \tag{3.20}$$

In order to probe the IR region, we work with a large interval $(-l/2, l/2)$ with $l \gg \xi$. It is then clear that the contour is trivial away from the entangling surfaces, and is universal and independent of l near the entangling surfaces

$$s_A(x) = \begin{cases} \dfrac{c}{6(x-\frac{l}{2})} & -\frac{l}{2} < x < -\frac{l}{2}+\xi \\ \\ 0 & -\frac{l}{2}+\xi < x < \frac{l}{2}-\xi \\ \\ \dfrac{c}{6(\frac{l}{2}-x)} & \frac{l}{2}-\xi < x < \frac{l}{2} \end{cases} . \tag{3.21}$$

This is the area law behavior we would hope for the contour to capture, though the polynomial decay of the contour is most likely due to our crude setup. We expect that more realistic gapped theories will have exponentially decaying entanglement contours. We bring the reader's attention to [108] where a similar quantity named the "entropy density" is introduced to study the structure of entanglement entropy around the entangling surface in gapped phases. Similarly, the contour may be interesting to study in higher dimensional gapped phases.

3.3 Higher dimensional contours, asymmetric subregions, and bit threads

It is clearly of interest to generalize the notion of an entanglement contour to arbitrary dimensions and entangling surface geometries. We address these issues in this section with motivations from the construction of holographic entanglement entropy from bit threads [92]. A bit thread construction involves a divergenceless vector field, v, whose norm is bounded by $(4G_N)^{-1}$. We sketch a bit thread configuration in Fig. 3.1. The Ryu-Takayanagi formula for a boundary region, A, can then be reformulated as a maximization problem

$$S(A) = \max_v \int_A v, \tag{3.22}$$

where the maximization is over all bit thread configurations. By comparing to the normalization condition, we immediately see how this notion of bit threads is useful for constructing entanglement contours. For any maximal bit thread configuration respecting the spatial symmetries of the boundary region, we can define the contour function

$$s_A(x) = |v(x)|. \tag{3.23}$$

We now prove this obeys the conditions from [87]:

1. Positivity: The contour is non-negative because the norm is non-negative.
2. Normalization: The work of [92] explicitly proved the normalization of the contour over a boundary region using the max-flow min-cut theorem.
3. Symmetry: We have imposed symmetry in the definition by only allowing bit thread configurations which respect the spatial symmetries of the region.
4. Invariance under local unitaries: As before, this is ensured by causality.
5. Upper bound: If the interval is a union of disconnected regions, there exist nontrivial factorizations of the Hilbert space. We take a disconnected region A and a subregion $X \subset A$. The flux of bit threads at X is bounded by the maximum flux of bit threads for all of A over all bit thread configurations, which is equivalent to the von Neumann entropy of A. Therefore, the upper bound is satisfied.

The degeneracy of extremal bit thread configurations is enormous. Given that these configurations respect the spatial symmetry of the boundary subregion, each provides a distinct contour function. This is a clear way of understanding the non-uniqueness of the entanglement contour. The only universal parts of the contour are the divergent pieces near the entangling surface. Far from the entangling surface, one can always choose a bit thread configuration for which the local contour function is trivial. However, the bit threads can be rearranged so that the local contour function is finite at the same point at which it was trivial for the other configuration. This is an unsettling phenomenon for a fine-grained entropy. We are willing to accept that the entanglement contour is not uniquely defined, but wish to impose additional constraints that would enforce the following property for any two contours, s^1_A and s^2_A: If $s^1_A(x) < s^1_A(y)$ for $x, y \in A$, then $s^2_A(x) < s^2_A(y)$.

Fortunately, recent work on bit threads [109] has provided explicit constructions of bit thread configurations which satisfy our conditions for the contour. We begin with what the authors refer to as "geodesic flows," where the bit threads follow bulk geodesics.

In d spatial dimensions, for boundary regions with spherical entangling surfaces of radius R, the following norm of the geodesic flow was found

$$|v| = \frac{c}{6}\left(\frac{2Rz}{\sqrt{(R^2+r^2+z^2)-4R^2r^2}}\right)^d , \tag{3.24}$$

where z is the bulk radial coordinate and r is the distance from the center of the ball-shaped region on the boundary. Note that all angular dependence has dropped out. The contour is defined at the boundary, so we find

$$s_A(r) = \frac{c}{6}\left(\frac{2R}{R^2-r^2}\right)^d . \tag{3.25}$$

The dimensional dependence clearly shows that only for the 1+1d case are there significant entanglement contributions away from the entangling surface, displaying the logarithmic violation to the area law. Interestingly, for 1+1d, this is the exact ground state contour function that is found using the bulk modular flow (3.6). This means that the bit threads

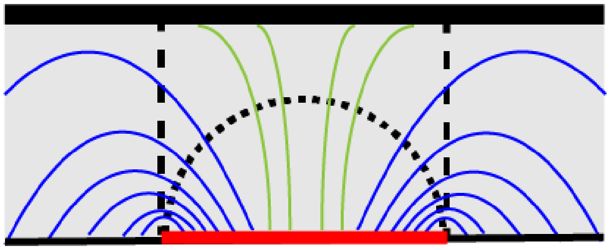

Figure 3.1: In the black hole geometry (subspace shown), there are two configurations for the minimal entanglement wedge cross section, the standard minimal surface (short dashed lines) and the disconnected surface reaching the horizon (longer dashes). For the entanglement entropy, bit threads can terminate on the black hole horizon, so both the green and blue bit threads contribute. For LN/EoP, only the blue bit threads will contribute.

following geodesics have matched boundary points to points on the RT surface identically to the matching from the modular flow.

3.3.1 Entanglement wedge cross sections

We would now like to restrict the bit threads to the entanglement wedge, which is the bulk dual of the CFT density matrix ρ_{AB} [110]. The entanglement wedge is a codimension-1 bulk region whose boundary is the union of the RT surface and $A \cup B$. Using the formalism for holographic logarithmic negativity (LN) from [111] where the negativity is related to the area of the minimal entanglement wedge cross section, we can concoct a contour for negativity [3]. Minimal entanglement wedge cross-sections for general entangling surface geometries have also been studied in connection to entanglement of purification (EoP) [114–124], so our contour can be interpreted in that context as well. Both LN and EoP are useful measures for mixed state entanglement.

We define a holographic entanglement contour for LN and EoP much in the same way as we did for the contour for the entanglement entropy. Again, we need a divergenceless vector

---

[3] An interesting attempt at constructing a negativity contour can be found in [112], and a more recent construction of a negativity contour inspired by the work in this chapter can be found in [113]

field, v, whose norm is now bounded by $\mathcal{X}_d(4G_N)^{-1}$ for LN and $(4G_N)^{-1}$ for EoP, where

$$\begin{aligned}\mathcal{X}_d &= \frac{1}{2}x_d^{d-2}\left(1+x_d^2\right)-1, \\ x_d &= \frac{2}{d}\left(1+\sqrt{1-\frac{d}{2}+\frac{d^2}{4}}\right),\end{aligned} \tag{3.26}$$

for spherical entangling surfaces. For less symmetric set-ups of LN, nontrivial backreactions in the bulk must be accounted for [111]. However, the formula for EoP is still valid for asymmetric set-ups. Guaranteed by the max-flow min-cut theorem, the entanglement wedge cross-section and hence the LN and EoP are calculated as

$$\mathcal{E}(A,B) = \max_v \int_A v = \max_v \int_B v, \tag{3.27}$$

where each bit thread must start and end on A and B. This leads us to the LN/EoP contour

$$e_A(x) = |v(x)|, \quad e_B(x) = |v(x)|. \tag{3.28}$$

In order to construct valid bit thread constructions restricted to the entanglement wedge, we need to use the notion of "maximally packed flows" [109]. For a single interval $(-l/2, l/2)$ at inverse temperature β, there are two configurations for the entanglement wedge cross-section. The cross-over from the standard extremal surface to the one connected to the horizon occurs around $l/\beta \sim 0.28$ (Fig. 3.1). In the connected regime, the LN/EoP contour is simply proportional to the thermal entropy contour (3.10)

$$e_A(x) = \frac{c\pi}{\xi\beta}\left(\coth\left(\frac{\pi(\frac{l}{2}+x)}{\beta}\right)+\coth\left(\frac{\pi(\frac{l}{2}-x)}{\beta}\right)\right), \tag{3.29}$$

where $\xi = 4$ for LN and $\xi = 6$ for EoP. More interestingly, when the cross-section is disconnected, thermal contributions are subtracted and we find that the LN/EoP contour is only

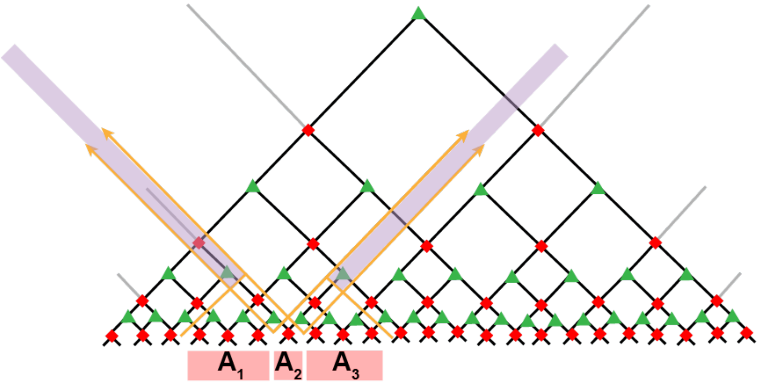

Figure 3.2: In kinematic space, the conditional mutual information is computed by the "bulk" volumes. The left and right shaded lavender regions are $I(A_2, \bar{A}|A_1)$ and $I(A_2, \bar{A}|A_3)$ respectively. Interpreting MERA as kinematic space, the entanglement contour is computed by the number of isometries (green triangles) in the shaded lavender regions.

nontrivial (and divergent) near the entangling surface

$$e_A(x) = 0, \quad \frac{l}{2} - |x| > \frac{\beta}{4\pi} \log 5 \tag{3.30}$$

clearly showing that β plays the role of the quantum correlation length in thermal systems.

3.4 Connection to kinematic space

Starting from a time slice of AdS (or any other Euclidean surface), one can define an auxiliary Lorentzian manifold known as *kinematic space* [125]. This manifold corresponds to the space of geodesics on the original space. In AdS/CFT, kinematic space encodes a number of important quantum information theoretic quantities related to the boundary CFT state in an elegant geometric fashion [125]. Here we describe how the entanglement contour can be encoded. Computationally, this may be useful for investigating the local entanglement structure in MERA tensor networks, which have been interpreted as a discretized version of kinematic space [126]. It also may be a useful local quantity for reconstructing bulk geometry in AdS/CFT.

The length of a geodesic, γ is computed by an integral over kinematic space, K

$$\gamma = \int_K \omega(u,v) m_\gamma(u,v), \tag{3.31}$$

where $\omega(u,v)$ is the Crofton form and $m_\gamma(u,v)$ is the number of intersections between γ and the geodesic anchored on lightcone coordinates (u,v). Another quasilocal measure of entanglement called the *entanglement density* is defined as [127]

$$n(u,v) \equiv \frac{1}{2}\frac{\partial^2 S(u,v)}{\partial u \partial v}. \tag{3.32}$$

This serves as the natural form for kinematic space [125]

$$\omega(u,v) = \frac{\partial^2 S(u,v)}{\partial u \partial v} du \wedge dv. \tag{3.33}$$

Restricting ourselves to an overall pure state with periodic spatial boundary conditions, the entanglement contour is then an appropriate volume of kinematic space

$$s_A(x) = \frac{1}{2}\int_{\substack{\{(u,v)=(u,x)|u\in(x',x_1)\}\\ \cup\{(u,v)=(x,v)|v\in(x_2,x')\}}} \omega, \tag{3.34}$$

with x' unconstrained because the continuum version of (3.7) can be found by integrating the entanglement density

$$\int_{x'}^{x_1} n(x,y)dx + \int_{x_2}^{x'} n(x,y)dy = \frac{1}{2}\left(\frac{\partial S(x_1,x)}{\partial x} - \frac{\partial S(x,x_2)}{\partial x}\right). \tag{3.35}$$

To choose a natural x', we rewrite the entanglement contour in terms of conditional mutual information

$$s_A(A_2) = \frac{1}{2}\left[I(A_2,\bar{A}|A_1) + I(A_2,\bar{A}|A_3)\right], \tag{3.36}$$

agreeing with our initial construction of (3.6). Conditional mutual information is encoded in kinematic space by volumes of appropriate causal diamonds (multiplied by factors of $\log \chi$, where χ is the bond dimension). In MERA tensor networks, volumes are equivalent to the number of isometries in the region. We demonstrate this in Fig. 3.2.

The relation between the entanglement contour and conditional mutual information completes the circle of connections between the contour, entanglement density, bit threads, and kinematic space. It may be illuminating to study these connections further in the context of quantum bit threads in MERA [128].

3.5 Quantum quenches

The entanglement contour is particularly suited to dynamical settings because it can locally quantify how quantum information flows in time. We use quantum quenches to model out-of-equilibrium processes. Using (3.6) for the contour, we follow the formalism developed in [129] in which the Riemann surface corresponding to a given quantum quench is mapped to the half plane. From there, the holographic entanglement entropy can be computed by geodesics in AdS with a spacetime boundary. For global and local (Calabrese-Cardy) quenches [130, 131], these conformal maps are

$$w^{\pm}_{glob}(x^{\pm}) = e^{2\pi x^{\pm}/\beta}, \quad w^{\pm}_{loc}(x^{\pm}) = \frac{x^{\pm}}{\epsilon} + \sqrt{\left(\frac{x^{\pm}}{\epsilon}\right)^2 + 1}, \tag{3.37}$$

where ϵ is a regulator. The contour for global quenches provides an excellent visual representation of the entanglement tsunami proposed in [93]. This includes an early time quadratic growth and late time linear growth (see Fig. 3.3). However, there is an important distinction between our picture and the tsunami. The tsunami velocity, v_E, for 1+1d CFTs is 1 in units of the speed of light. Similar to the discussion in Ref. [87], we find that the entanglement propagates in real space at a *contour velocity* of

$$v_c = 2. \tag{3.38}$$

This is not a violation of causality because entanglement should not be thought of as a local object propagating from the entangling surface, as in the original tsunami picture. Rather, it can heuristically be thought of as a set of non-local waves generated at every point in space, analogous to the quasi-particle picture [132]. This leads to the larger "velocity" of entanglement (3.38). Furthermore, the contour waves move through each other at $t = l/4$ and only halt once they have reached the opposite entangling surface at $t = l/2$. On the contrary, in the original tsunami picture, the waves stop once they have reached each other. This presents a significant difference when investigating the spatial structure of entanglement. The tsunami predicts that there is no entanglement between the center of the interval and the interval's complement when $t < l/2$ while the contour predicts nontrivial entanglement at the interval center for $t > l/4$. While the tsunami velocity accurately predicts the growth of the entanglement entropy non-locally (i.e. of the entire subsystem), the contour velocity captures the real-space velocity at which the entanglement spreads in real space. The contour velocity will generally depend on spacetime dimensions and its relation to the tsunami velocity will be less trivial than the factor of 2 that was found in $1 + 1$d. It would be fascinating to find effective equations of motion for the entanglement contour analogous to those which have been studied for entanglement entropy and out-of-time-ordered correlators [133–137]. These may directly address the question of how quantum information locally flows in time. We expect different equations of motion for integrable and ergodic theories.

For the local (Calabrese-Cardy) quench, the tsunami picture does not apply, though we find a transient contour wave propagating at $v_c = 1$. (see Fig. 3.4). After the wave passes, the contour relaxes to its ground state value.

An additional way to induce a local quench is by inserting a local heavy operator of

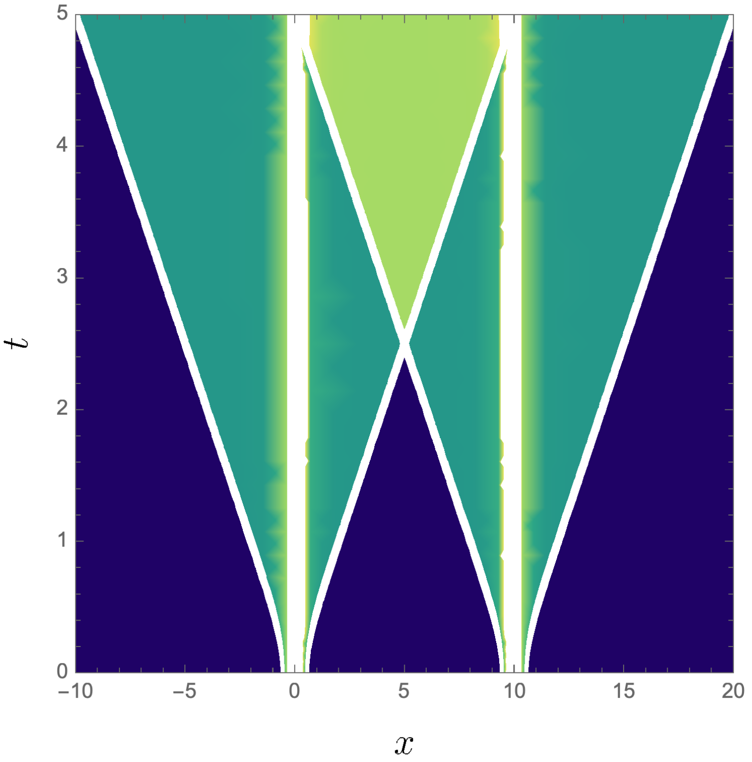

Figure 3.3: The entanglement contour following a global quench with $c = 1$ and $\beta = 2$. After initial quadratic growth, the contour waves propagate at $v_c = 2$ and cross one another at $t = l/4$, only to halt at $t = l/2$. The contour for the interval saturates at its thermal value.

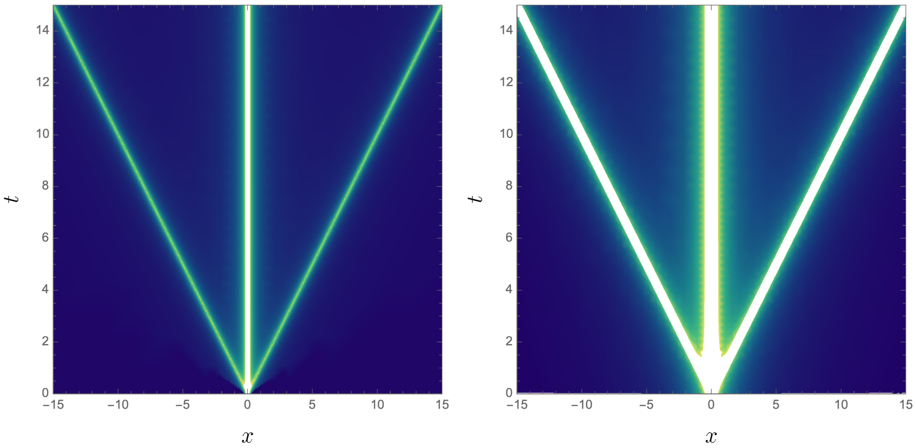

Figure 3.4: (left) The entanglement contour following a local (Calabrese-Cardy) quench for semi-infinite intervals with $c = 1$ and $\epsilon = 1/10$. (right) Local heavy operator quench with central charge $c = 1$, $\alpha_\psi = 1/2$, and $\delta = 1$. Now, $v_c = 1$. Once the wave front passes, the contour relaxes to its ground state value.

weight h_ψ at the origin. The gravity dual to this protocol was shown to be a boosted black hole [127]. The entanglement entropy for an interval (l_1, l_2) away from the origin for a time $t > 0$ is found [104]

$$S_A^{out} = \begin{cases} \dfrac{c}{3}\log\left[\dfrac{l_2 - l_1}{\epsilon}\right] & t < l_1 \text{ or } t > l_2 \\ \dfrac{c}{6}\log\left[\dfrac{(l_2-l_1)(t-l_1)(l_2-t)}{\epsilon^2\delta}\dfrac{\sin(\pi\alpha_\psi)}{\alpha_\psi}\right] & \\ & l_1 < t < l_2 \end{cases}, \tag{3.39}$$

where δ is a regulator for the operator insertion and $\alpha_\psi = i\beta_\psi/2\pi$. We find an entanglement contour for semi-infinite intervals

$$s_A(x) = \begin{cases} \dfrac{c}{12}\dfrac{(2x-t)}{x(x-t)} & 0 < t < x \\ \dfrac{c}{6}\log\left[\dfrac{\sin(\pi\alpha_\psi)}{\delta\alpha_\psi}\right]\delta(x-t) & t = x \\ \dfrac{c}{6x} + \dfrac{c}{12}\dfrac{1}{t-x} & x < t \end{cases}. \tag{3.40}$$

The late time behavior is a combination of the vacuum value and a relaxation term. The contour following the operator quench is contrasted with the (Calabrese-Cardy) quench in Fig. 3.4.

For an interval that contains the origin, the entanglement entropy is

$$S_A^{in} = \begin{cases} \frac{c}{3}\log\left[\frac{l_2 - l_1}{\epsilon}\right] & t < |l_1|, t > l_2 \\ \\ \frac{c}{6}\log\left[\frac{(l_2 - l_1)(l_1 + t)(l_2 + t)}{\epsilon^2 \delta}\frac{\sin(\pi\alpha_\psi)}{\alpha_\psi}\right] & \\ & |l_1| < t < \sqrt{-l_1 l_2} \\ \\ \frac{c}{6}\log\left[\frac{(l_2 - l_1)(t - l_1)(l_2 - t)}{\epsilon^2 \delta}\frac{\sin(\pi\alpha_\psi)}{\alpha_\psi}\right] & \\ & \sqrt{-l_1 l_2} < t < l_2 \end{cases} . \tag{3.41}$$

An interesting feature of the contour can be seen from an interval containing the origin. As we would expect from causality, the total entanglement entropy of the interval is constant at early times. However, the contour is able to detect the rearrangement of entangled degrees of freedom within the interval. That is, the distribution of entanglement between the local degrees of freedom inside of the interval and the complement of the interval changes, but the total entanglement entropy of the interval remains the same.

3.6 Logarithmic Light Cones from the Entanglement Contour

As another example of the utility of the entanglement contour, we study the entanglement contour after a global quench in two paradigmatic non-thermalizing phases: many-body localization (MBL) and the random singlet phase (RSP).

3.6.1 Many-Body Localization

Many-body localization is perhaps the best known example of ergodicity-breaking in many-body quantum systems. Broadly speaking, it occurs in interacting lattice systems when an on-site potential is tuned to be sufficiently spatially disordered. MBL has been a subject of intense study in recent years. See, for example, the recent review Ref. [138] and references there within. As the strength of the on-site disorder is increased relative to the interaction strength, more and more of the system's high energy eigenstates turn from typical volume-law entanglement states (as the eigenstate thermalization hypothesis would imply), to short-range entangled area-law states [139]. Once the localization transition is passed, all eigenstates of the system become area-law entangled, and the system is fully many-body localized. Before reaching the transition, it is possible to have a mobility edge, separating area-law states from volume-law states. In addition to the area-law eigenstates, MBL systems display a number of interesting features. In the localized phase, the systems contain an extensive number of emergent local integrals of motion (LIOMs, sometimes called "l-bits"), with exponentially decaying spatial support. One can write an effective Hamiltonian for the MBL system in terms of these LIOMs [139, 140].

MBL systems are also fascinating from a dynamical perspective. Generic interacting many-body quantum systems are thought to be ergodic in the sense that after sufficiently long time evolution, expectation values of local operators become exponentially close to their corresponding thermal expectation values. Thus, memory of the initial state becomes inaccessible to local measurements and any subsystem can be described by a small number of thermodynamic quantities. MBL systems, on the other hand, do not thermalize. The conserved LIOMs serve to retain memory of the initial state, precluding a description of the late-time state by a thermal ensemble. MBL provides an important counterexample to the eigenstate thermalization hypothesis (ETH) and motivates us to further understand when and how closed quantum systems fail to thermalize. We additionally note that MBL phases and their non-ergodic properties have been directly observed in a number of experimental settings [141–143].

Despite their lack of energy and particle transport, MBL systems nevertheless produce nontrivial long-range entanglement in far-from-equilibrium scenarios. For example, if we quench into an MBL Hamiltonian starting from a product state, the entanglement entropy grows logarithmically in time for a time that scales exponentially with the system size [144, 145]. After this time, the saturated entanglement entropy in finite systems displays a volume-law, though with a smaller multiplicative coefficient than the volume-law for the thermal state [145]. In some sense, this volume-law indicates a partial thermalization of finite size MBL systems [139]. We are motivated to study this unusual entanglement growth more deeply. In particular, we would like to understand how the entanglement spreads at a local level and if/how the information becomes delocalized.

To ensure that we capture universal features of the MBL phase, and not artifacts of a particular model, we use the phenomenological MBL fixed point Hamiltonian constructed from the local integrals of motion

$$H_{LIOM} = -\sum_i h_i \sigma_i^z - \sum_{i<j} J_{ij}^{(2)} \sigma_i^z \sigma_j^z - \sum_{i<j<k} J_{ijk}^{(3)} \sigma_i^z \sigma_j^z \sigma_k^z + \cdots \tag{3.42}$$

Here, the Pauli operators σ_i^z denote emergent local integrals of motion, which are exponentially localized in the physical lattice. For our purposes, we treat them as perfectly localized, for the sake of computation. The interaction terms are defined as

$$J_{ij}^{(2)} = \frac{J_{ij}}{2} \exp(-|i-j|/\xi), \quad J_{ijk}^{(3)} = \frac{J_{ijk}}{6} \exp(-|i-k|/\xi), \tag{3.43}$$

where J_{ij} and J_{ijk} are drawn randomly (from a uniform distribution $[-J_0, J_0]$, with $J_0 = 100$ in our case, but other distributions can be used) and ξ is a dimensionless localization length (which we pick to be 0.5). We also draw h_i from the same distribution. This model was used to compute the OTOC in [146, 147].

Before turning to numerics, we motivate an analytical prediction for the form of the entanglement contour in MBL using the language of the emergent LIOMs. The effective interaction between two "l-bits" separated by a distance d is given by [148]

$$J^{\mathit{eff}} \sim \mathcal{J} \exp(-d/\xi), \tag{3.44}$$

where $\mathcal{J}$ is a characteristic interaction strength. Using the effective interaction of the dressed spins, one can obtain an estimate for the amount of time it takes for two unentangled l-bits a distance d apart to become entangled. This happens when $J^{\mathit{eff}} t \geq 1$, so

$$t \sim \frac{1}{\mathcal{J}} \exp(-d/\xi). \tag{3.45}$$

We now consider an MBL system on a chain of total length L, with a subinterval $[0, \ell]$. Picking a point $x < \ell$ within this subinterval, we can count the number of l-bits outside of the interval with which the l-bit at point x is entangled at a particular time t. This is precisely what the entanglement contour should describe. The result (up to proportionality constants) is

$$s_A(x,t) \propto \begin{cases} 0 & t < \frac{e^{\frac{\ell - x}{\xi}}}{J_0} \\ \\ \frac{1}{L}\big(\xi \log(\mathcal{J}t) + x - \ell\big) & \frac{e^{\frac{\ell - x}{\xi}}}{\mathcal{J}} \leq t \leq \frac{e^{\frac{L - x}{\xi}}}{\mathcal{J}} \\ \\ 1 - \frac{\ell}{L} & t > \frac{e^{\frac{L - x}{\xi}}}{\mathcal{J}} \end{cases} \tag{3.46}$$

The form of a logarithmic light cone is clear; the wave front of the contour arrives at a time exponential in the distance from the entangling surface $t = \frac{1}{\mathcal{J}} \exp\left(\frac{\ell - x}{\xi}\right)$. Once this time

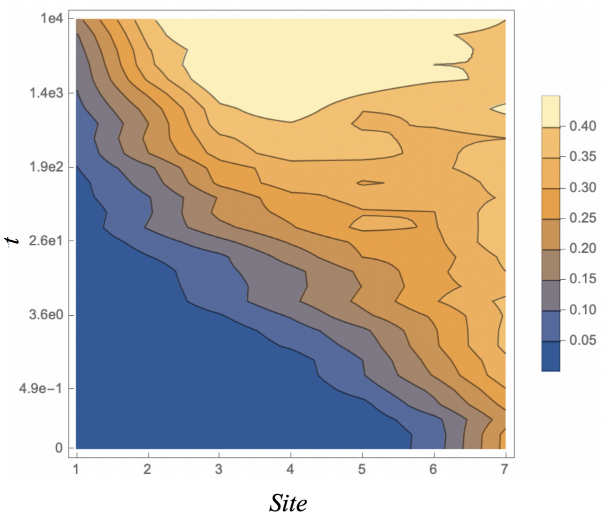

Figure 3.5: The entanglement contour after a global quench into H_{LIOM} averaged over 40 disorder realizations, normalized by $\log 2$, and smoothed out to remove pixelation. The quench was performed from random product states on 14 sites using a disorder strength of $J_0 = 100$. The contour depicted describes the seven leftmost sites. The level sets make the logarithmic entanglement light cone clear (modulo the edge effects occurring at sites 1 and 2).

has passed, the magnitude of the contour increases linearly, saturating at a constant value. This agrees with the observation that entanglement entropy grows logarithmically with time in MBL, eventually reaching a volume-law in the long time limit in a finite system. Let us now turn to numerics in order to verify (3.46).

We select a subinterval consisting of the leftmost 7 sites of our 14 site chain and compute the entanglement contour of this interval after the global quench using H_{LIOM}. We observe a distinct logarithmic light cone in the entanglement contour in Fig. 3.5. A similar logarithmic light cone has previously been observed in out-of-time-order correlators (OTOCs) of certain local operators in the MBL phase [149]. These are related but distinct light cones.

The authors of Ref. [149] computed the OTOC as a function of space and time in the disordered Heisenberg model. Defining the butterfly velocity, v_B, as

$$j_\epsilon \sim v_B \log_{10} t, \tag{3.47}$$

where j_ϵ is the site at which the wave front of the OTOC has increased past the threshold value of $\epsilon \in (0, 1)$ at time t, they find that v_B depends on both temperature and ϵ, with a slower speed of propagation for lower temperatures. In Refs. [146, 150], the authors show that in the MBL LIOM model, the position of the wavefront (up to additive constants and for some suitably defined cutoff) of the OTOC after disorder averaging is given by

$$j_{LIOM} \propto \xi \log(t)\,. \tag{3.48}$$

Our numerical checks for the zero temperature OTOC, indicate that the butterfly velocity for the LIOM model with $\xi = 0.5$, for the initial all $|+\rangle$ product state and for a suitably defined cutoff of 0.5, is $v_B = \frac{\xi}{\log_{10} e} \sim 1.15$.

We can analogously define the contour velocity

$$j_c \sim v_c^\epsilon \log_{10} t \tag{3.49}$$

where j_c is the site that the contour wave front of value $\epsilon \times \tilde{s}^\beta$ has reached. $\tilde{s}^\beta$ is the equilibrium entropy density at effective temperature β which is fixed by the energy of the quench. Using the cutoff $\epsilon = 0.075$, and fitting a line to the wave front in Fig. 3.5, we arrive at a contour velocity of $v_c^\epsilon \sim 1.5$. Like the butterfly velocity, this result is somewhat dependent on the choice of cutoff ϵ, and may also depend on the choice of initial state. It therefore seems that the contour velocity is larger than the butterfly velocity, but perhaps only marginally so, unlike the case of CFT where we have the very distinct result $v_c = 2v_B$. More comprehensive numerical study of the entanglement contour after a global quench in MBL is warranted in future work, and could yield a more precise understanding of the relationship between v_B and v_c in MBL.

3.6.2 The Random Singlet Phase

As another example of a non-thermalizing system, we study the dynamics of a disordered free fermion model that admits a random singlet phase [151] as its ground state for sufficiently strongly disordered hopping. The random singlet phase (RSP) infinite-disorder critical point has a number of interesting features, including CFT-like logarithmic scaling of entanglement entropy [152–155], with an effective central charge equal to $\log 2$ times the central charge of the clean theory. The RSP is the fixed point of the strong disorder real space renormalization group (SDRG) [34], and can be seen in e.g. the antiferromagnetic random bond Heisenberg model [151]. It should be noted, however, that the universal features of the RSP ground state seen at the SDRG fixed point do not necessarily extend to excited states in interacting models. Indeed, while the RSP-like critical behavior extends to the excited states of a non-interacting model like the one we use here (resulting in a so-called "quantum critical glass"[156, 157]), small interactions can drive these excited states to an MBL spin glass phase. Studying the dynamics of an interacting model with a RSP ground state using the entanglement measures in this chapter presents an interesting future problem. Some work in this direction has recently been done [158], and it is found that the resulting particle-hole symmetric MBL phase exhibits entanglement growth behavior whose functional form depends on interaction strength, unlike conventional MBL.

Additional work has been done to investigate the dynamics of the random singlet phase. For example, Ref. [159] studied the late-time growth of entanglement entropy in the RSP after a global quench using numerical methods and found it to be doubly logarithmic in time. Other works have studied entanglement growth in disordered critical phases e.g. Refs. [160, 161]. We build upon this work by characterizing the spread and delocalization of information in the RSP.

We use a single band, free fermion model with disordered hopping to yield the random singlet phase. The Hamiltonian is

$$H = \sum_i J_i \left(c_i^\dagger c_{i+1} + c_{i+1}^\dagger c_i \right), \tag{3.50}$$

where $J_i \in [0, 1]$ at each bond is drawn independently from the known fixed-point distribution $P(J) = \frac{1}{\delta} J^{-1+1/\delta}$. The parameter δ corresponds to disorder strength. $\delta \to 0$ corresponds to the clean limit, and we approach the infinite randomness fixed-point as $\delta \to \infty$. For the purpose of numerics, $\delta = 2.5$ corresponds to sufficiently strong disorder to yield the desired properties of the random singlet phase, and this is the value we use in our simulations.

We now use the contour to investigate finer-grained aspects of the entanglement entropy growth at long timescales after a quench into the random singlet phase. For our initial state, we use the ground state of the Hamiltonian

$$H_0 = \sum_i J \left(c_i^\dagger c_{i+1} + c_{i+1}^\dagger c_i \right) + \sum_j m_0 (-1)^j c_j^\dagger c_j, \tag{3.51}$$

which has a gap controlled by the magnitude of m_0. Also note that J is not random in H_0. We use $m_0 = 0.5$ for the initial state of our quench. At $t = 0$, after preparing the ground state at half filling of (3.51), we begin to time evolve with (3.50). We then compute the entanglement contour at each site, for each timestep thereafter. This constitutes our quantum quench.

The entanglement contour generated by the quantum quench described above on a 200 site chain can be seen in Fig. 3.6. Though the production of entanglement is weaker than it is in the clean limit, the contour demonstrates nontrivial spreading. The smallest discernible values of the entanglement contour (0.001) appear to carve out a logarithmic light cone, consistent with the infinite dynamical critical exponent of the random singlet phase [159].

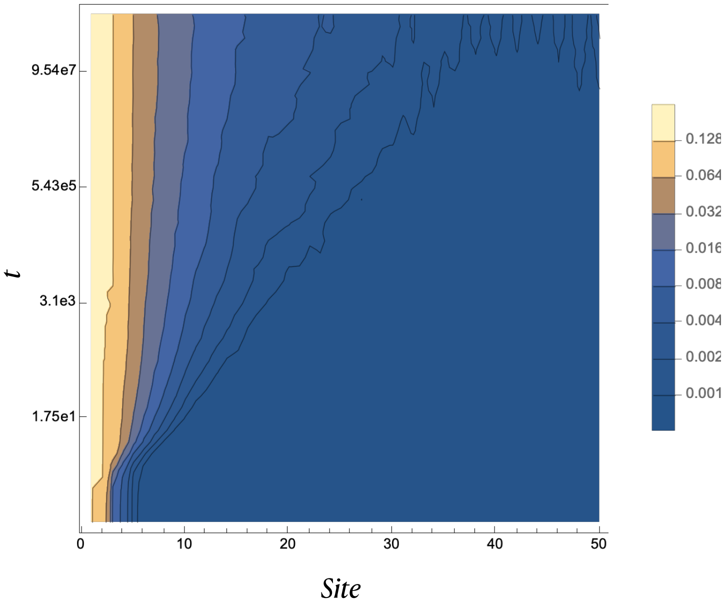

Figure 3.6: The entanglement contour for sites 150 to 200 in an open chain of 200 sites averaged over 5000 disorder realizations and normalized by $\log 2$ on a semilog plot. We use $m_0 = 0.5$ and a clean hopping for our initial state, and quench into the Hamiltonian (3.50) with $\delta = 2.5$ and $t = 0$. We see the emergence of a logarithmic light cone for the smaller-valued level sets, consistent with the infinite critical exponent known to occur in the RSP. At very late times ($\sim 10^8$ units of time), we see some deviation from the log light cone in the upper-right hand corner of the plot, likely as a result of finite size effects.

Between the times 1.75×10^1 and 5.45×10^5, the 0.001 contour fits very well with the function

$$x(t) \sim v_c \log_{10}(t) + x_0, \tag{3.52}$$

where we find $v_c \sim 3.56$ for the contour velocity.

We also include a plot of the early time entanglement entropy in Fig. 3.7 for the above quench configuration. This early time entanglement entropy growth fits very well with the quasi-particle calculation detailed in App. B. The late time entanglement entropy growth, as computed by summing the contour over its subinterval, is doubly logarithmic, as shown in previous works [159]. We omit this result here and include only the novel, early time behavior.

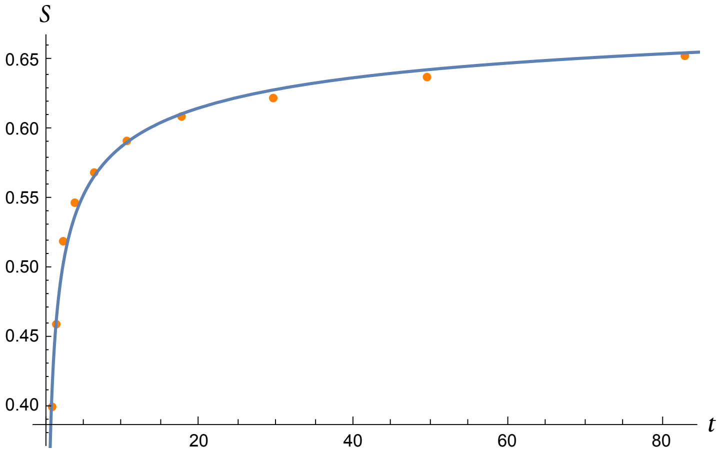

Figure 3.7: The quarter chain entanglement entropy for early times after a global quench into the random singlet phase for a system of 200 sites. After an initial linear increase, the entropy grows approximately as a power law before transitioning to a sub-logarithmic regime at very long times (not depicted). The numerical results (dots) are averaged over 5000 disorder realizations. The analytic estimate for the entanglement entropy is displayed as blue line. We fit using $\beta_{eff} = 0.1972$. The analytic estimates derived from the quasi-particle picture show excellent agreement with the numerics.

3.7 Discussion

In this chapter, we have introduced an entanglement contour for generic 1+1d systems and proposed a generalization to arbitrary dimensions and entangling surface geometries for holographic CFTs using the notion of bit threads. We emphasize that the entanglement contour, as specified by the five requirements, is generically a non-unique quantity, and our proposed form of the contour selects one particular contour function out of a possibly infinite number. States whose entanglement structure is purely bipartite (e.g. a completely dimerized state) are the only ones with a unique entanglement contour. We have found that the entanglement contour is particularly enlightening when studying dynamical situations and clarifies the physical picture associated to the entanglement tsunami. We argue that the tsunami velocity is the velocity of nonlocal entanglement growth for an interval while the contour velocity captures the real-space velocity of entanglement propagation in real space. It may be fascinating to study higher dimensional quantum quenches to determine how the contour velocity is affected. A covariant description of bit threads will play a key role. Furthermore, generalizations to higher curvature gravity (à la [162]), gauge theories, and tensor network states other than MERA are exciting avenues for understanding quantum entanglement at an even finer-grained level. Indeed, a "negativity contour" was fully developed soon after the work in this chapter was done [113]. Hopefully, this will lead to further insights about the fine-grained structure of quantum entanglement.

CHAPTER 4

MULTIPARTITE OPERATOR ENTANGLEMENT IN NON-THERMALIZING SYSTEMS

In the previous chapter, we explored the entanglement contour and used it to probe the spatial evolution of entanglement in MBL, among other systems. Computing the entanglement contour after a quantum quench of course requires choosing an initial state. Since it is possible to choose spurious or unrepresentative initial states that will not reveal much about the dynamics of the system in question, it is worthwhile to look for state-independent probes of entanglement and classical correlations. To this end, we will introduce operator entanglement, which seeks to quantify the intrinsic ability of a quantum system's Hamiltonian to spread information, without reference to a particular state. After defining several operator entanglement measures, we review prior results comparing chaotic and free systems from the perspective of operator entanglement. Finally, we present results for multipartite operator mutual information and negativity — measures of scrambling — in an MBL system, finding that quantum information spreading is suppressed relative to total information spreading. The work in this chapter was derived from [98].

4.1 Defining Operator Entanglement

To define the operator entanglement [163], we first map the time evolution operator, $U(t)$, to a state in a doubled Hilbert space, $\mathcal{H}_1 \otimes \bar{\mathcal{H}}_2$, under the channel-state duality [164, 165]. We can do this by first explicitly expanding the time evolution operator in its energy eigenbasis:

$$U(t) = e^{-iHt} \sum_i |i\rangle \langle i| . \tag{4.1}$$

We can then dualize the bra vector to define the state

$$|U(t)\rangle = \mathcal{N} e^{-iH_1 t} \sum_i |i\rangle_1 \, |i^*\rangle_2 \, , \tag{4.2}$$

where we take the CPT conjugate and $\mathcal{N}$ is a normalization factor. The Hamiltonian acts only on the first copy of the Hilbert space. We then compute entanglement measures within this state as we would in any other state. Throughout this chapter, we let A be a subsystem in the "input" Hilbert space, $\mathcal{H}_1$, and B, C be subsystems in the "output" Hilbert space, $\mathcal{H}_2$, with $B \cup C = \mathcal{H}_2$. Using this partitioning, we can compute the bipartite operator mutual information (BOMI) using the standard definition of mutual information in terms of operator entanglement entropies

$$I(A, B) = S(A) + S(B) - S(A \cup B), \tag{4.3}$$

and tripartite operator mutual information (TOMI) by a taking linear combination of BOMIs

$$I_3(A, B, C) = I(A, B) + I(A, C) - I(A, B \cup C). \tag{4.4}$$

The TOMI is symmetric about the three regions and diagnoses the extent to which information is delocalized in the quantum channel [166]. More specifically, the first two terms reveal the amount of total information from region A accessible by measurements in either region B or C, respectively. The third term is the amount of information from the input subsystem A that can only be accessed by non-local measurements in the total output system $B \cup C$ — initially localized information that has been spatially spread out. Therefore, negative values of I_3 indicate that most of A's information has been delocalized, and that it cannot be accessed by separate measurements in B or C.

One disadvantage of the mutual information is that it is sensitive to both quantum and classical correlations, as discussed in 1.3.1. To attempt to isolate the quantum information that is scrambled, we compute bipartite operator logarithmic negativity (BOLN) i.e. the logarithmic negativity, $\mathcal{E}(A,B) \equiv \log(|\rho_{AB}^{T_B}|_1)$, in the operator state. In analogy to TOMI, we also study the tripartite operator logarithmic negativity (TOLN)

$$\mathcal{E}(A:B,C) = \mathcal{E}(A,B) + \mathcal{E}(A,C) - \mathcal{E}(A,B \cup C). \tag{4.5}$$

The TOLN characterizes the amount of purely quantum information scrambled by the quantum channel. Negative values of TOLN indicate information delocalization similarly to those of TOMI.

4.2 Operator Entanglement in Example Systems

To build some intuition for operator entanglement, we will present two extreme examples of its behavior. First, we will BOMI and TOMI in a free fermionic system, which — though it spreads bipartite entanglement — is manifestly non-scrambling. On the other extreme, we will present similar results from a holographic CFT, which we use as a paradigm of a strongly interacting system. Here we find maximal scrambling, as demonstrated by negative values of TOMI.

4.2.1 Free Fermions

The behavior of operator entanglement in free systems can be intuited using the quasiparticle picture [2]. We can compute it explicitly using free fermions (see Appendix A for details). In a symmetric configuration of input A and output B subsystems (where they overlap in space, but B is larger), we see that the BOMI of A and B decreases from an initial maximum according to the quasiparticle velocities. We can see this in Fig. 4.1.

Applying the same quasiparticle analysis to other BOMI configurations, one finds that

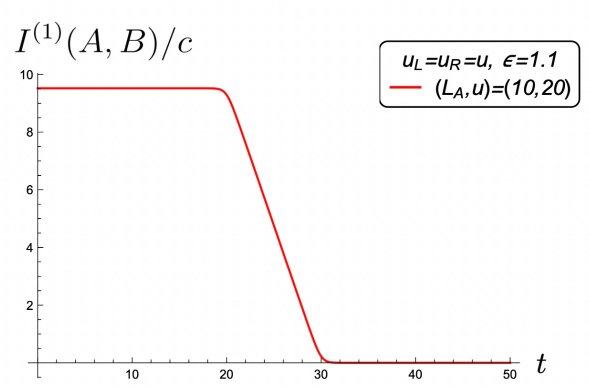

Figure 4.1: Bipartite operator mutual information for symmetric input and output subregions (i.e. the same spatial subregions) for a $c = 1$ free-fermion CFT. Figure from [2], reused with permission of the author.

the tripartite operator mutual information for free fermions is identically zero. Indeed, any free system — or more generally, any system with localized quasiparticles — yields trivial TOMI, as both classical and quantum information travel in discrete packets and do not delocalize.

4.2.2 Holographic CFTs

On the other end of the scrambling spectrum, we have holographic CFTs, which strongly delocalize information. One can use the Ryu-Takayanagi (RT) formula to compute BOMI and TOMI in these systems to see this scrambling. In Fig. 4.1, we see that BOMI begins to decrease immediately.

Using the RT formula to compute TOMI for a holographic CFT, we see that it saturates to a maximally negative value in a time linear in the subsystem size. This indicates the maximum possible scrambling of classical and quantum information (at least asymptotically).

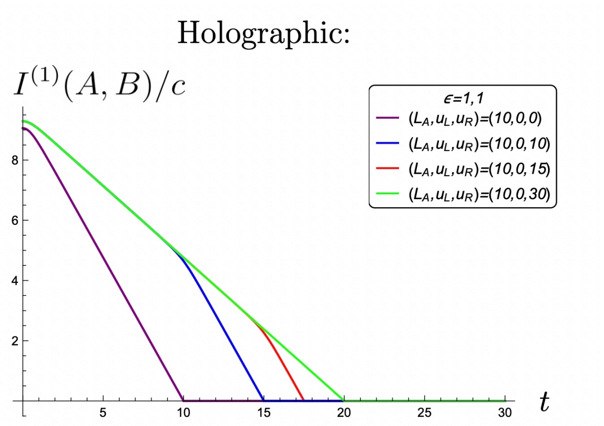

Figure 4.2: BOMI for different symmetric and antisymmetric subsystem configurations for a $c \gg 1$ holographic CFT. Figure from [2], reused with permission of the author.

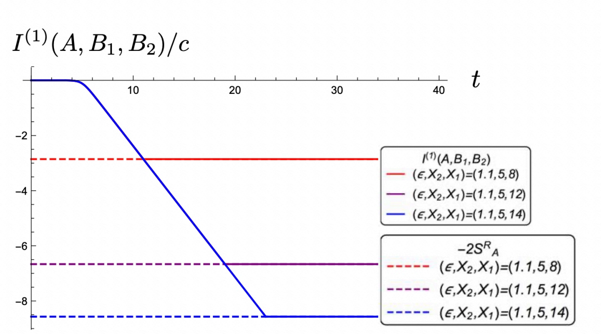

Figure 4.3: TOMI for different symmetric and antisymmetric subsystem configurations for a $c \gg 1$ holographic CFT. Figure from [2], reused with permission of the author.

4.3 Operator Entanglement in MBL

Now that we have seen two extreme cases of BOMI and TOMI, we will look at MBL, whose ability to spread information lies somewhere in between a free system and the holographic CFT. We will use the LIOM basis to compute operator mutual information for a MBL system. We start with the following Hamiltonian,

$$H_{LIOM} = -\sum_i h_i \sigma_i^z \quad - \sum_{i<j} J_{ij}^{(2)} \sigma_i^z \sigma_j^z - \sum_{i<j<k} J_{ijk}^{(3)} \sigma_i^z \sigma_j^z \sigma_k^z,$$

where we have truncated terms beyond third order. In the LIOM basis, the time evolution operator for a chain of N spins is

$$\begin{aligned} U &= \sum_{\{s\}} e^{-itH_{LIOM}(s)} |s_1 \cdots s_N\rangle\langle s_1 \cdots s_N|, \\ H_{LIOM}(s) &= -\sum_i h_i s_i - \sum_{i<j} J_{ij}^{(2)} s_i s_j - \sum_{i<j<k} J_{ijk}^{(3)} s_i s_j s_k, \end{aligned} \tag{4.6}$$

where $\sum_{\{s\}}$ is a sum over all 2^N classical spin configurations. Since U is already diagonal in the LIOM basis, and we can replace the Pauli operators in the Hamiltonian with classical spin values. To compute operator entanglement measures we use the channel-state duality to obtain the U operator state, and then we take the outer product to get the density matrix of the doubled Hilbert space state

$$\rho_U = \sum_{\{s\},\{s'\}} e^{it\left[H_{LIOM}(s) - H_{LIOM}(s')\right]} |s_1 \cdots s_N\rangle\langle s_1' \cdots s_N'|, \tag{4.7}$$

where $|s_1 \cdots s_N\rangle$ labels collectively spin configurations in the input and output Hilbert spaces, for brevity. We can go further by subdividing the input and output Hilbert spaces

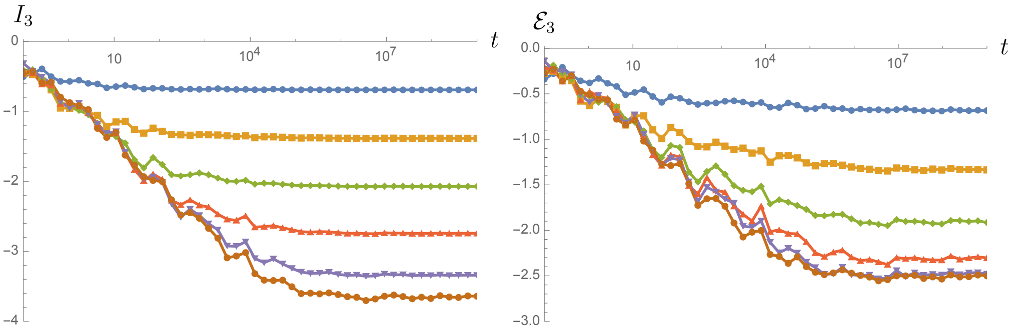

Figure 4.4: TOMI (left) and TOLN (right) for the H_{LIOM} for a system of 12 input and 12 output qubits for various subinterval sizes. Note the logarithmic timescale and the slow saturation of both quantities, and the larger (negative) magnitude of TOMI compared to TOLN, indicating a reduced spread of quantum vs. classical information.

into intervals A, D and B, C, respectively:

$$\rho_U = \sum_{\{s\},\{s'\}} e^{it\left[H_{LIOM}(s)-H_{LIOM}(s')\right]} |\{s\}_A, \{s\}_B, \{s\}_C, \{s\}_D\rangle\langle\{s'\}_A, \{s'\}_B, \{s'\}_C, \{s'\}_D|.$$

We choose A and B to be of the same size and position in their respective Hilbert spaces. To obtain a reduced density matrix for the operator state — for example for $A \cup B$ — we can trace out $C \cup D$

$$\rho_{AB} = \sum_{\{s\}_A,\{s\}_B,\{s'\}_A,\{s'\}_B} \sum_{\{s\}_C,\{s\}_D} \times e^{it\left[H_{LIOM}(s_A,s_B,s_C,s_D)-H_{LIOM}(s'_A,s'_B,s_C,s_D)\right]} |\{s\}_A, \{s\}_B\rangle\langle\{s'\}_A, \{s'\}_B|. \tag{4.8}$$

By performing the sums over s_C and s_D to calculate the matrix elements of ρ_{AB}, we can avoid directly storing and tracing over a $2^{2N} \times 2^{2N}$ matrix, and instead deal with, at most, a $2^N \times 2^N$ matrix. This is not a dramatic decrease in numerical overhead, but it allows us to (nearly) double the size of the system in question when computing operator entanglement measures, as compared to directly performing the partial trace over the full operator state density matrix.

We find slow scrambling in the tripartite operator mutual information and tripartite operator logarithmic negativity as seen in Fig. 4.4. Like many other observables in MBL, the values of

TOMI and TOLN take an exponentially long time to saturate. While a significant portion of the information in the input channel is delocalized under time evolution, the Haar random values of TOMI and TOLN are never reached[1]. Intriguingly, it appears that the scrambled *quantum information* (TOLN) may scale differently with system size than the *total information* (TOMI). In Fig. 4.5, we show the saturated values of TOMI and TOLN as a function of input interval size for our 12 site chain.

While TOMI scales at or near a volume law (up until half the system size), the magnitude of TOLN is smaller, suggesting the possibility of sub-volume law scaling, and indicating that the spreading of quantum correlations is suppressed compared to total correlations. By "total", we are referring to both the quantum and classical (thermal) correlations to which mutual information is sensitive[2] (see e.g. Ref. [18]). To the best of our knowledge, this is a new phenomenon that might be useful in characterizing the quasi-thermal, late-time state. It would be very interesting to further distinguish this late-time state from conventionally scrambled states. Given the small scales of our numerics, these signatures of novel scrambling behavior may be experimentally accessible in Noisy Intermediate-Scale Quantum (NISQ) devices [170] where protocols for preparation of the thermofield double state (4.2) are being developed [171].

4.4 Discussion

In this chapter we have introduced the notion of operator entanglement as a state-independent means of assessing a Hamiltonian's ability to spread entanglement and classical correlations. After reviewing the behavior of operator mutual information in both free and holographic CFTs, we computed TOMI and TOLN in the MBL LIOM effective model. The results indicated an interesting pattern of behavior, where both quantites saturate very slowly — exponentially slowly in the system size — and where at long times TOMI and TOLN seem to saturate to qualitatively different spatial

---

[1] See Ref. [167] for discussion on more quantum systems that scramble non-maximally. We also note that bipartite operator entanglement measures have previously been been studied in MBL systems [144, 168].

[2] See Ref. [169] for an interesting comparison between mutual information and negativity in MBL eigenstates.

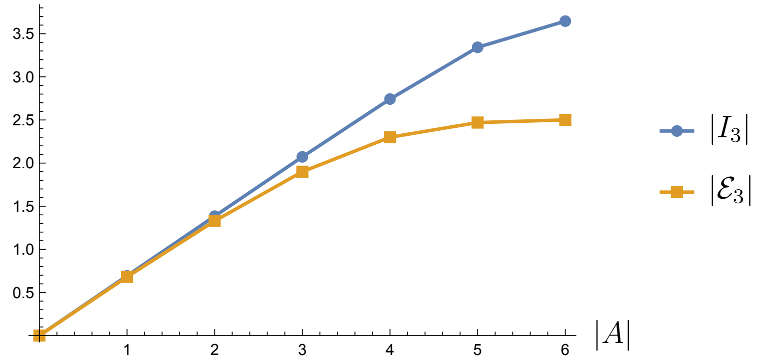

Figure 4.5: Late time saturation values of TOMI and TOLN for the 12 qubit MBL chain, calculated using LIOMs. The saturation values of TOMI fit well to the volume law $I_3(L_A) = \log(2)L_A$, while the TOLN values grow more slowly in magnitude with system size, indicating suppressed delocalization of quantum information.

profiles. It would be interesting to perform the same analysis using larger scale numerics via matrix product operator methods, to see if this pattern persists.

CHAPTER 5

REALIZING ENTANGLED QUANTUM STATES ON NEAR-TERM QUANTUM DEVICES

So far in this thesis we have introduced different measures of entanglement and used them to probe many-body quantum systems with unusual patterns of entanglement. Much of this work has come at a fortuitous time, as noisy intermediate-scale quantum (NISQ) devices are beginning to become easily accessible, and are steadily growing in size and quality. This new technology should allow for unprecedented control over the simulation of large many-body quantum systems. In this chapter we put forward a method to increase the size of 2D lattice systems that can be simulated on a NISQ device by taking advantage of tensor networks. Although we do not compute any entanglement measures here, we introduce a method that will allow for the probing of entanglement in many-body quantum states on near-term quantum computers. We also provide a proof of concept of the method using the Honeywell trapped-ion device. The work in this chapter was derived from [172].

5.1 Introduction

As the number of qubits offered by modern universal quantum computers remains relatively small, it is advantageous to make greater use of the available quantum resources by measuring and reusing qubits. Such capability has recently become available on some quantum processors [173], allowing one to simulate quantum systems consisting of more qubits than are present on the physical device. Several recent works have taken this approach, simulating both static and dynamical one-dimensional (1D) matrix product states (MPS) of quasi-infinite length using a constant number of qubits [174–176]. Since most physical quantum states of interest are not maximally entangled, it should not be necessary to use N qubits to simulate most relevant N-qubit states. Instead, we propose an adaptation of existing tensor network ansätze, which are designed to efficiently represent many-body quantum states on classical computers by exploiting their entanglement structure [1].

Here we take an approach similar to the one used for MPS in [174–176], but with 2D tensor networks. Specifically, we map a subset of projected entangled pair states (PEPs) tensor networks

— which represent 2D quantum states on a square lattice — to a quantum circuit, and run the resulting circuit on a trapped-ion quantum device. By measuring and reusing qubits, as well as imposing some constraints on the PEPs tensors, we are able to map an $N \times M$ PEPs state to a circuit on $\mathcal{O}(N \log \chi)$ qubits, where χ is the bond dimension, rather than $\mathcal{O}(N \times M)$ qubits, as the direct mapping would entail. The resulting circuit allows for measurement of arbitrary observables in the PEPs state, without resorting to approximations. Although PEPs tensor networks achieve significant compression, they are not efficiently contractible on classical computers [177], and their utility as a numerical tool has thus been limited. By outsourcing the contraction problem to a quantum computer, we can exactly probe the physics of larger 2D PEPs states than we could on a classical computer alone.

In this article, we first summarize in Section 5.2 the experiment we ran on the Honeywell System Model H1-1 trapped-ion device [173, 178], one of a handful of available quantum processors with mid-circuit measure-and-reuse capability. Here, we map a PEPs representation of the topologically-ordered ground state of the Wen plaquette model to a quantum circuit, achieving a compression of 9 qubits to 5. We then measure a non-trivial loop observable at various values of a magnetic field perturbation, and compare the results from the ion trap to the classically-contracted tensor network and to exact diagonalization. This allows us to probe the effects of device noise on the computed values of the observable, to establish the feasibility of our approach for larger system sizes. In Section 5.3, we provide more details about the mapping from PEPs tensor networks to quantum circuits, comparing our approach with that from the recent work [179]. Finally, we close with a discussion of the results and potential future work.

5.2 Summary of Experiment

To demonstrate the practicality of our mapping using an existing quantum device, we map a 9-qubit PEPs tensor network with bond dimension $\chi = 2$ onto a 5-qubit quantum circuit, with mid-circuit measurements acting as the physical indices of the tensors. A cartoon of the mapping is depicted in Fig. 5.1.

After optimizing the tensor network (on a classical computer) to reproduce the ground state of a topologically nontrivial Hamiltonian, we compute expectation values of observables in this state by executing the corresponding circuit on the Honeywell System Model H1-1 trapped-ion device. With the resulting data, we then compare the experimental results to exact and tensor network numerical results for these observables.

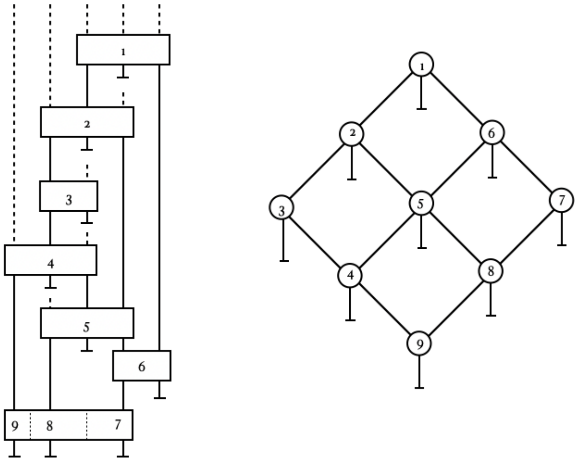

Figure 5.1: On the left is the 5-qubit circuit corresponding to the 9-qubit PEPs tensor network shown on the right. All qubits are initialized to the zero state at the top of the circuit. The vertical lines truncated by horizontal bars are physical sites and correspond to mid-circuit measurements in the circuit. Dotted lines correspond to qubits in the zero state. After a qubit is measured mid-circuit, it is reset to the zero state.

Our task consists of finding the PEPs representation of the ground state of a particular Hamiltonian, mapping that PEPs to a circuit, and using the circuit to compute non-local order parameters that indicate the phase of the ground state.

5.2.1 Tensor Parameterization and Optimization

We study the Wen plaquette model [180]:

$$H_0 = -\sum_{i \in sites} \sigma_i^x \sigma_{i+\hat{x}}^y \sigma_{i+\hat{x}+\hat{y}}^x \sigma_{i+\hat{y}}^y, \tag{5.1}$$

where $i+\hat{x}$ and $i+\hat{y}$ indicate neighboring sites to the site i in the x and y directions, respectively. This model's fourfold degenerate ground states (on the plane with open boundary conditions) possess Z_2 topological order, which can be diagnosed by measuring a number of different loop operators. Since our 9-site lattice has a boundary, we use the following boundary order parameter (described in [181]) to detect topological order:

$$\hat{O} = \sigma_1^y \sigma_2^z \sigma_3^x \sigma_4^z \sigma_9^y \sigma_8^z \sigma_7^x \sigma_6^z. \tag{5.2}$$

This is a closed-loop around the boundary of the square lattice. This operator can be obtained by taking a product of the four plaquette operators in our Hamiltonian. In the perfectly topologically-ordered ground states of (5.1), we have $|\langle \hat{O} \rangle| = 1$. We introduce the following magnetic field term, as in [180], to break the topological order:

$$H_{\text{mag}} = -g \sum_{i \in sites} (\sigma_i^x + \sigma_i^y + \sigma_i^z) \tag{5.3}$$

Our full Hamiltonian is thus $H = H_0 + H_{\text{mag}}$. As we increase g, the magnetic field strength, the topological order breaks down and $|\langle \hat{O} \rangle| \to 0$. The exact values of $|\langle \hat{O} \rangle|$ for $g \in [0, 1.2]$ are represented by the blue line in Fig. 5.3.

With the Hamiltonian in hand, we must first find a PEPs tensor network that approximates the ground state of the system for various values of the magnetic field strength g. To parameterize the tensors to be optimized, we start with the unitary circuit elements as depicted on the left-hand side of Fig. 5.1. The 2-qubit unitaries in the circuit consist of a single Mølmer-Sørensen (MS) entangling gate [182] abutted by a 3-parameter $SU(2)$ gate on each incoming and outgoing rail (see Fig. 5.2). Thus, the 2-qubit unitaries each contain 12 parameters. The 3-qubit unitaries in our circuit consist of two staggered 2-qubit unitaries, and thus contain 24 parameters (though only 21 independent parameters).

The unitary operators are then mapped to tensors by contracting their appropriate auxiliary bonds with the $|0\rangle$ state (depicted by dotted lines in Fig. 5.1). For the final row, we perform two successive singular value decompositions on the final 3-qubit unitary to yield the tensors numbered 7, 8, and 9, respectively. The use of a single MS gate in our unitary parameterization ensures that the bond dimension of the resulting tensors is no greater than 2, as desired. It is worth noting that

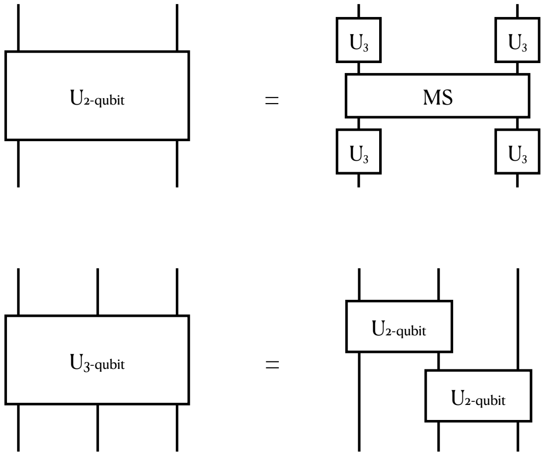

Figure 5.2: The decomposition of the two and three qubit gates used to parameterize the PEPs circuit. The 2-qubit gate consists of a single Mølmer-Sørensen gate [3] surrounded by an IBM-type U_3 rotation [4] on each input and output rail. Each U_3 gate contains 3 parameters, giving $U_{2-qubit}$ a total of 12 parameters. Meanwhile, $U_{3-qubit}$, which consists of two, staggered $U_{2-qubit}$ gates, contains 21 independent parameters.

many of the parameters in the unitary parameterization of the circuit are redundant, as contracting some of the input bonds of these unitaries reduces the effective rank of the resulting map. This is not a major concern when we are optimizing small numbers of parameters (144 in this case), but a less redundant parameterization may be necessary for efficient optimization of parameters in larger circuits.

Once we have mapped the parameterized unitaries to tensors, we can contract them into a 3×3 square lattice PEPs pattern, as seen on the right panel in Fig. 5.1. This is now the parameterized state $|\psi(\boldsymbol{\theta})\rangle$, where $\boldsymbol{\theta}$ are the 144 parameters of the circuit. We then minimize the expectation value of the Hamiltonian to find the tensor network approximation of the ground state for a particular value of g $|GS_{\text{TN}}(g)\rangle$

$$|GS_{\text{TN}}(g)\rangle = |\psi(\boldsymbol{\theta}_g)\rangle, \quad \boldsymbol{\theta}_g = \underset{\boldsymbol{\theta}}{\operatorname{argmin}} \frac{\langle\psi(\boldsymbol{\theta})|H(g)|\psi(\boldsymbol{\theta})\rangle}{\langle\psi(\boldsymbol{\theta})|\psi(\boldsymbol{\theta})\rangle} \tag{5.4}$$

We use the NLopt [183] implementation of COBYLA [184] to perform this optimization.

5.2.2 Experimental Results

The values of $\langle \hat{O} \rangle$ for the tensor approximations of $|GS(g)\rangle$ for $g = \{0, 0.1, 0.2, 0.4, 0.6, 1.0\}$ are depicted as green dots in Fig. 5.3. These values of the order parameter are not identical to the exact values (blue curve), due to the limited bond dimension of the tensor network. They are, however, close enough to the exact values to distinguish between topological and trivial phases for very high or very low values of g.

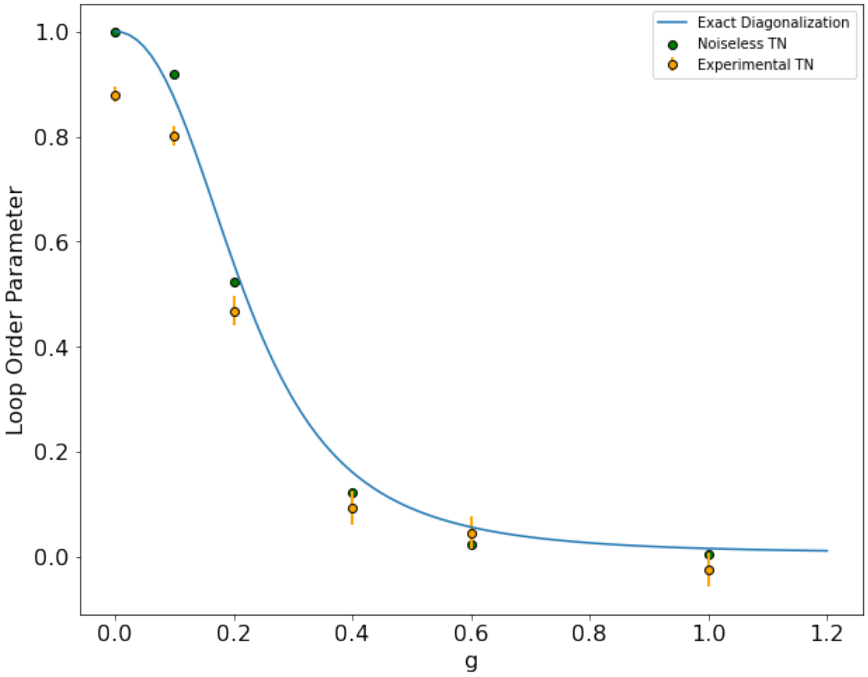

Figure 5.3: Values of the loop observable (5.2) for various values of the magnetic field strength, g. The blue curve indicates the results from exact diagonalization of the Hamiltonian. The green dots are the values of the observable for the tensor network approximation of the ground state (without noise). The orange dots are the experimental results, each corresponding to 1000 shots of the PEPs circuit on the Honeywell System Model H1-1 device. The error bars on the orange dots correspond to statistical error.

The effects of the noise from the System Model H1-1 device are evident in the experimental results (orange points). The experiment consisted of 1000 shots of the PEPs circuit for each separate value of g. The error bars on the orange dots are purely from the statistical error from measurements. The error bars are relatively small, so the orange dots provide good data on the effects of noise on the circuit. Overall, the noise has the effect of dampening the values of the loop observable. This effect is more pronounced the larger the expected values of the observable are. At $g = 0$, for example, where $\langle \hat{O} \rangle$ is exactly 1, the results from our circuit yield $\langle \hat{O} \rangle \approx 0.88$, which, absent exact results, serves as a strong indication of topological order. As the strength of the magnetic field g is increased, the measured values of the observable follow the exact tensor network values very closely, and clearly exhibit the transition from topological order to trivial, ferromagnetic order, providing at least a fuzzy phase boundary. The topological order appears to be broken by the time g reaches the value 1.

The quality of the results for our loop observable indicates that our experiment could potentially by scaled up to larger lattice sizes and still yield useful results on existing quantum hardware.

5.3 Mapping Tensor Networks to Quantum Channels

Unlike matrix product states, PEPs tensor networks have no intrinsic ordering that would allow them to be easily mapped to a quantum circuit. Thus, before defining a map from tensors to unitary operators, we must choose an ordering of the contraction of the PEPs tensors that will allow us to construct a quantum circuit. Moreover, we would like to find an ordering that will yield a *qubit-efficient* mapping from PEPs networks to quantum circuits. Ideally, we want to make use of mid-circuit measurement and reset so that our circuit contains fewer qubits than are present in the corresponding PEPs state, along the lines of the "holographic" simulation of MPS tensor networks employed in [174–176]. To this end, we order the PEPs tensor network in a zig-zag pattern, as depicted in Fig. 5.5. The incoming and outgoing arrows on the physical and virtual bonds of a tensor indicate the flow of time, and correspond to the input and output indices of a unitary circuit element, respectively.

Tensors that have more output than input indices can be supplemented with additional input indices (which will be fixed to the $|0\rangle$ state) in order to embed them in a unitary matrix. For example, the tensor numbered 1 in Fig. 5.5 contains three output and zero input bonds. Two of the output bonds are virtual bonds, each of bond dimension χ and will thus require $N_{\mathrm{B}} = \lceil \log_2 \chi \rceil$ qubits as virtual qubits in a corresponding unitary. Thus, a corresponding unitary operator is a $2N_{\mathrm{B}} + 1$ qubit unitary with all of its input qubits initialized in the $|0\rangle$ state. Similarly, tensor 3 will

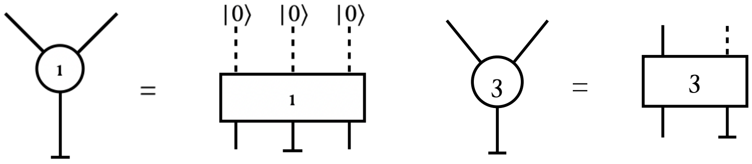

Figure 5.4: A mapping of tensors 1 and 3, respectively, from the causally-ordered tensor network depicted in Fig. 5.1 to unitary operators containing auxiliary input legs, which are always initialized to the zero state. For the unitary operators on the right and side, time flows from top to bottom.

be mapped to a unitary operator on $N_\mathrm{B}+1$ qubits, with one of the input qubits set to $|0\rangle$ — N_B of the qubits in the unitary correspond to the virtual bonds, while the additional qubit corresponds to the physical bond. Diagrammatic examples of this supplementation of bonds can be seen in Fig. 5.4. It is important to note that all supplementary bonds are input bonds. This allows the input qubits to these bonds to be deterministically set to $|0\rangle$ before the execution of the unitary gate. This allows us to avoid post-selection, an issue that would arise with output bonds that must be set to $|0\rangle$.

With this zig-zag causal ordering in place, we can map PEPs tensor networks on rectangular lattices of size $N \times M$ for arbitrary M with bond dimension $\chi = 2^{N_\mathrm{B}}$ to quantum circuits on $N_\mathrm{Q} = (N+1) \times N_\mathrm{B} + 1$ qubits. This becomes qubit-efficient, that is $N_\mathrm{Q} < N \times M$, when

$$M > \left\lfloor \left(1 + \frac{1}{N}\right) N_\mathrm{B} + \frac{1}{N} \right\rfloor, \tag{5.5}$$

or, in terms of the number of bond qubits,

$$N_\mathrm{B} < \left\lfloor \frac{N \times M - 1}{N+1} \right\rfloor. \tag{5.6}$$

For example, for a 3×3 square lattice, we must have a bond dimension of 2 or lower for our circuit to be qubit-efficient. For a general $N \times N$ square lattice, the circuit is qubit-efficient if $N_\mathrm{B} \leq (N-1)$. Thus, for a given bond dimension, the circuit mapping becomes more qubit-efficient as we increase the size of the lattice.

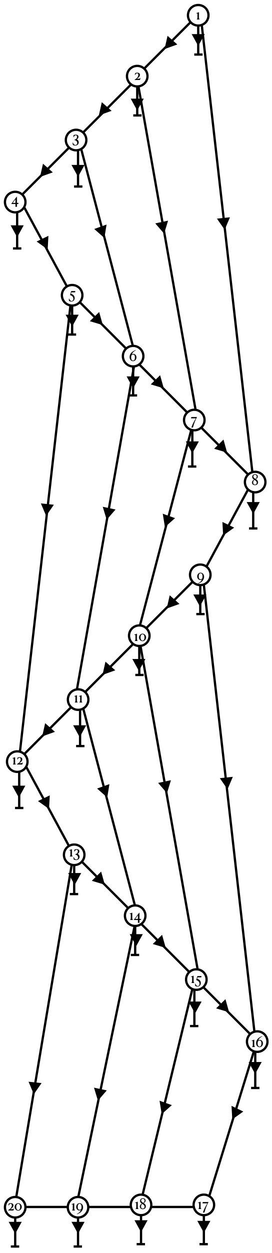

Figure 5.5: The zig-zag causal pattern used to map a PEPs tensor network onto a quantum circuit, depicted for a 4 × 5 qubit rectangular lattice. When mapping to unitary circuit elements, time runs from top to bottom, and physical bonds — indicated by the dangling lines with orthogonal indicated by dangling lines from tensors with orthogonal crosses — correspond to mid-circuit measurements followed by qubit resets.

5.3.1 Parameterizing the PEPs Tensors

One can choose a variety of tensor decomposition methods as a means to parameterize the PEPs tensor network, and, ultimately, its corresponding quantum channel. In parameterizing tensor 3 in Figs. 5.1 and 5.4, for example, starting with an arbitrary rank-3 tensor (assuming $\chi = 2$ for now), $T_i^{\alpha\beta}$ (where Roman letters indicate physical bonds and Greek letters indicate virtual bonds and we use Einstein summation), one can construct a 2-qubit unitary $U_{i\beta,\alpha\gamma}$ such that when one of the input qubits is set to the zero state (as depicted in Fig. 5.4), we have

$$U_{i\beta,\alpha\gamma}\delta_{\gamma,0} = U_{i\beta,\alpha 0} = T_i^{\alpha\beta}. \tag{5.7}$$

Once this constraint is in place, we must ensure the unitarity of $U_{i\beta,\alpha\gamma}$:

$$U^*_{\lambda\sigma,i\beta}U_{i\beta,\alpha\gamma} = \delta_{\lambda\sigma,\alpha\gamma} \tag{5.8}$$

$$U^*_{\lambda 0,i\beta}U_{i\beta,\alpha 0} = T_i^{*\lambda\beta}T_i^{\beta\alpha} = \delta_{\lambda,\alpha}. \tag{5.9}$$

This first constraint indicates that the tensors must be isometric in one direction (that is, when we contract a bond index and a physical index of two tensors, we obtain the identity for the remaining bond indices). Expanding the second constraint,

$$\begin{aligned} U_{j\zeta,\alpha\gamma}U^*_{\alpha\gamma,i\beta} &= \delta_{j\zeta,i\beta} \\ &= U_{j\zeta,\alpha 0}U^*_{\alpha 0,i\beta} + U_{j\zeta,\alpha 1}U^*_{\alpha 1,i\beta} \\ &= T_j^{\zeta\alpha}T_i^{*\alpha\beta} + U_{j\zeta,\alpha 1}U^*_{\alpha 1,i\beta}\delta_{j\zeta,i\beta} \qquad (5.10) \\ U_{j\zeta,\alpha 1}U^*_{\alpha 1,i\beta} &= \delta_{j\zeta,i\beta} - T_j^{\zeta\alpha}T_i^{*\alpha\beta}. \qquad (5.11) \end{aligned}$$

This second constraint allows us to solve for the remaining components of the unitary matrix using the components of the tensor.

5.3.2 Comparison with Isometric Tensor Networks

The constraints we impose on the PEPs tensors in order to define a causal structure are related to those proposed for so-called "isometric tensor networks" (isoTNS) [185]. In that work, the authors outline a procedure that involves first choosing a site (the "orthogonality center") in a 2D tensor network on which one wishes to compute the expectation value of a local observable. The column and row that intersect at this site then become the "orthogonality hypersurface". The tensors constituting the complementary regions of this hypersurface are then chosen to be isometric, with orthogonality to the hypersurfaces defining the "causal order" along which tensor contractions are isometric. In our zig-zag causal structure, no orthogonality center is specified, and the direction of isometry is different than that implied by the isoTNS method if we had chosen the final row of tensors as an orthogonality hypersurface. In our causal order, alternating rows have alternating causal order, whereas in the isoTNS structure, rows of tensors parallel to the orthogonality hypersurface have unidirectional causal order.

The disadvantage of the isoTNS approach is that one must select an orthogonality center before computing an observable, making it inconvenient for computing large or non-local observables, such as Wilson loops. In a work produced just before the work in this chapter by Slattery and Clark [179], the authors propose "quantum isometric tensor networks" (qisoTNS), which are very similar, but not identical to this proposal. In that work, as in this, one does not need to restrict to a selected orthogonality hypersurface in order to compute an observable. The work by Slattery and Clark retains the causal structure implied by isoTNS, unlike our zig-zag causal structure, but achieves similar compression of $N \times N$ square lattices to $\mathcal{O}(N \log \chi)$ qubit circuits, as our work does.

5.3.3 Mapping the Final Row of Tensors

For the final row of tensors evaluated in the circuit (i.e. tensors $17, 18, 19$, and 20 in Fig. 5.5), one may either continue the zig-zag pattern employed for the previous rows, or use one large N-qubit unitary operator to contain all N tensors in the row. In the former case, the mapping from tensors to unitaries proceeds as outlined in 5.3.1. In the latter case, one can simply contract the

N tensors of the final row together to form an N-qubit operator, and constrain the tensors such that this operator is unitary. This is what we have done to parameterize the tensor network in our experiment, as it slightly reduces the depth of the circuit as compared to the case where we retain zig-zag ordering in the final row.

5.4 Discussion

In this chapter we demonstrate the possibility of obtaining useful results from a PEPs to quantum circuit mapping on existing quantum hardware, at least for small system sizes. The obvious next step is to scale up the system size and determine the point at which device noise washes out the values of the desired observables and the results are no longer useful as e.g. probes of topological order. The H1-1 device supports up to 10 qubits, allowing for PEPs tensor networks with bond dimension 2 of up to $8 \times M$ (for arbitrary M) qubits to be simulated. The utility of the results and their resilience to noise will vary depending on the system and the measured observables, but measuring a long range loop order parameter in a topological phase, as we have done in this chapter, could serve as a fairly sensitive benchmark for the susceptibility of the circuit to noise.

As suggested in [179], it is not exactly clear how expressive PEPs tensor networks with isometric constraints can be. Clearly, the causal structure imposed by mapping PEPs to a circuit will limit what correlations can and cannot be present in the system. It may also prevent the exact imposition of certain spatial symmetries on the system. Whether this limitation can be overcome by simply increasing the bond dimension, or if this sort of PEPs tensor network is limited to a certain subset of 2D states is an interesting question. One advantage of this construction is the direct access it allows to the bonds of the PEPs tensor network, which should allow for fairly straightforward computation of various entanglement measures. It would be very interesting, via direct tomography or some other method, to use this approach to experimentally measure, e.g. the topological entanglement entropy in a 2D state [5, 6]. Additionally, it may be interesting to construct an analogous mapping for non-square lattice tensor network states. More broadly, it is worth asking if and how one could achieve some sort of quantum advantage using an approach like this. This would likely involve finding a noise-resilient observable in a specifically-chosen interacting 2D model, and measuring it using a quantum circuit of a size that cannot be efficiently classically simulated. Attempting to construct such a problem would be an interesting and worthwhile project. Regardless, it is likely that NISQ devices will at least serve as important companions to classical simulation in the study of strongly-correlated many-body quantum systems in the very near future.

CHAPTER 6

CONCLUSION AND OUTLOOK

In this thesis, we have surveyed several ways in which entanglement can take on unusual spatial distributions in quantum systems, both static and dynamical. Though it is unsurprising that a change in background geometry will affect the correlations in a quantum state, we have observed how dramatic these changes to entanglement structure can be. Moreover, we have presented a general way to compute the entanglement entropy — and related quantities — by choosing an appropriately curved cutoff in the bulk theory corresponding to the holographic CFT. These interesting geometric changes to entanglement structure motivated further development of the entanglement contour, a tool that allowed us to probe finer details of a state's entanglement structure. The entanglement contour was shown to be particularly well-suited to studying out-of-equilibrium quantum systems, and we used it to characterize the entanglement dynamics after quantum quenches in several different systems, including a many-body-localized system, where a logarithmic entanglement light-cone appeared to emerge.

Staying on the course of dynamical quantum systems, we sought to better understand how a many-body-localized system is able to spread entanglement and classical correlations, independent of the initial quench state. We thus introduced the notion of operator entanglement, providing several examples of its behavior from previous works. We then presented novel calculations of tripartite operator mutual information and negativity in MBL. These results revealed that the operator entanglement measures saturate exponentially slowly in the system size, and that the spatial profiles of the saturated mutual information and negativity appear to be qualitatively different from each other, indicating a sort of decoupling of classical and quantum correlations that is not seen in conventional interacting systems.

Finally, we took a slight change of course and presented a method for efficiently simulating many-body 2D quantum systems on existing quantum computers. Though this work did not directly involve the calculation of entanglement, methods like it will likely be incredibly useful for studying entangled quantum matter in the near future.

Further developments to these specific works are alluded to in each of the chapters. More broadly, there are many open questions and interesting areas of inquiry in the realm of many-body quantum entanglement. Among the most difficult is the study of multipartite entanglement. As mentioned in the introductory chapter, qualitatively different species of entanglement (GHZ, W, etc.) emerge when more than two qubits are present in a system, and there is no systematic way to fully characterize entanglement in systems larger than a few qubits. Indeed, the task is already quite formidable in the case of four qubits [186]. While measures of bipartite entanglement have been used to great success in characterizing quantum phases of matter, further work on multipartite entanglement could yield new tools for investigating many-body quantum systems. These tools (if they are easily computable) could provide insights into e.g. topological phases of matter, thermalization, or ergodicity-breaking that were previously invisible to conventional entanglement measures. How do GHZ, W, D, and other types of entanglement distribute themselves in these states? What physical consequences does this have? A better understanding of multipartite entanglement could also aid in the design of better resource states for measurement-based quantum computing [187].

Since generic quantum many-body systems are interacting, we are limited in our ability to understand them using analytical techniques and classical numerics. Even many tensor network methods fail when we approach certain interesting domains of physics (e.g. strong disorder). The emergence of noisy intermediate scale quantum devices provides some hope that a powerful new tool for understanding strongly entangled quantum matter is on the horizon. With sufficiently low noise, and sufficiently many qubits, it should be possible in the very near future to answer questions about strongly interacting quantum systems that were previously inaccessible to standard methods. We hope to see the formation of a positive feedback loop between the knowledge gained from studying quantum entanglement and the development and use of new quantum devices for further probing highly entangled quantum systems.

APPENDIX A

OPERATOR ENTANGLEMENT AND NEGATIVITY FOR FREE FERMIONS

In this appendix, we present a review of how to compute operator entanglement measures for free fermion systems using the correlator method.

We wish to compute the operator mutual information for the following state

$$|U_\beta(t)\rangle = e^{-\frac{it}{2}(H_1+H_2)}\,|TFD_\beta\rangle \tag{A.1}$$

for a free fermion Hamiltonian with no superconducting terms

$$\hat{H} = \sum_{i,j=1}^{L} H_{i,j} c_i^\dagger c_j. \tag{A.2}$$

We can diagonalize this Hamiltonian with a unitary matrix U, so $H = UDU^\dagger$:

$$\hat{H} = \underbrace{c_i^\dagger U_{ik}}_{\equiv \psi_k^\dagger} D_{kl} \underbrace{U_{lj}^\dagger c_j}_{\equiv \psi_l} = \psi_k^\dagger D_{kl} \psi_l = \epsilon_k \psi_k^\dagger \psi_k. \tag{A.3}$$

We then write down the thermofield double state with the fermions in the diagonal basis.

$$\begin{aligned} |TFD_\beta\rangle &= \frac{1}{\sqrt{Z}} \prod_k \Big(\sum_{i_k} e^{-\frac{\beta}{2}\epsilon_k \psi_k^\dagger \psi_k} |i_k\rangle\, |i_k^*\rangle \Big) \\ &= \frac{1}{\sqrt{Z}} \prod_k \Big(1 + e^{-\frac{\beta}{2}\epsilon_k} \psi_{Ak}^\dagger \psi_{Bk}^\dagger \Big) |0\rangle\,. \end{aligned} \tag{A.4}$$

Requiring $\langle TFD_\beta | TFD_\beta\rangle = 1$ fixes the normalization factor as $Z = \prod_k \left(1 + e^{-\beta\epsilon_k}\right)$. The normalized thermofield double state is thus

$$|TFD_\beta\rangle = \prod_k \left(\underbrace{\frac{e^{\frac{\beta}{2}\epsilon_k}}{\sqrt{1+e^{\beta\epsilon_k}}}}_{\equiv \cos\theta_k} + \underbrace{\frac{1}{\sqrt{1+e^{\beta\epsilon_k}}}}_{\equiv \sin\theta_k} \psi_{Ak}^\dagger \psi_{Bk}^\dagger \right) |0\rangle \tag{A.5}$$

and the time evolved operator state becomes

$$|U(t)\rangle = \prod_k \left(\cos\theta_k + \sin\theta_k e^{-it\epsilon_k} \psi^\dagger_{Ak} \psi^\dagger_{Bk}\right) |0\rangle \,. \tag{A.6}$$

We now rewrite the operator state (A.6) by using the holes of the B Hilbert space instead of the particles because this allows us to use the regular correlation matrix without pairing terms. Let χ_{Ak}, χ_{Bk} be new fermion operators and consider

$$\begin{aligned} &\prod_k \left(\cos\theta_k \chi^\dagger_{Bk} + \sin\theta_k e^{-it\epsilon_k} \chi^\dagger_{Ak}\right) |0\rangle_\chi \\ &= \prod_k \left(\cos\theta_k + \sin\theta_k e^{-it\epsilon_k} \chi^\dagger_{Ak}\chi_{Bk}\right) \prod_q \chi^\dagger_{Bq} |0\rangle_\chi \,. \end{aligned} \tag{A.7}$$

We now define $\chi_{Ak} = \psi_{Ak}$, $\chi_{Bk} = \psi^\dagger_{Bk}$ and note $|0\rangle_\psi \sim \prod_q \chi^\dagger_{Bq} |0\rangle_\chi$ because $\psi_{Bp} |0\rangle_\psi \sim \chi^\dagger_{Bp} \prod_q \chi^\dagger_{Bq} |0\rangle_\chi =$ 0, since $(\chi^\dagger)^2 = 0$. The ψ and χ fermions are related by a particle-hole transformation on H_B. The state (A.7) is already normalized. In terms of the χ_{Ik} fermions, we have

$$|U(t)\rangle = \prod_k (\cos\theta_k \chi^\dagger_{Bk} + \sin\theta_k e^{-it\epsilon_k} \chi^\dagger_{Ak}) |0\rangle \tag{A.8}$$

where it is understood that $|0\rangle = |0\rangle_\chi$.

Now we compute the correlation matrix

$$\langle U(t)| \chi^\dagger_{Ik}\chi_{Jk'} |U(t)\rangle = \delta_{kk'} \langle U(t)| \chi^\dagger_{Ik}\chi_{Jk} |U(t)\rangle \,, \tag{A.9}$$

where we note that if $k \neq k'$, $\chi^\dagger_{Ik}\chi_{Jk'} = -\chi_{Jk'}\chi^\dagger_{Ik}$ annihilates $|U(t)\rangle$. Suppose that the product over the modes in (A.8) is arranged in increasing order. The matrix element for each mode k can be computed from

$$
\begin{aligned}
\langle U(t)| \chi^\dagger_{Ik}\chi_{Jk} |U(t)\rangle = \langle 0| \prod_{q>k} &(\cos\theta_q \chi_{Bq} + \sin\theta_q e^{it\epsilon_q}\chi_{Aq}) \\
\times &\Big[(\cos\theta_k \chi_{Bk} + \sin\theta_k e^{it\epsilon_k}\chi_{Ak})\chi^\dagger_{Ik}\chi_{Jk} \\
\times &(\cos\theta_k \chi^\dagger_{Bk} + \sin\theta_k e^{-it\epsilon_k}\chi^\dagger_{Ak})\Big] \\
\times &\prod_{p>k}(\cos\theta_p \chi^\dagger_{Bp} + \sin\theta_p e^{-it\epsilon_p}\chi^\dagger_{Ap}) |0\rangle
\end{aligned}
\tag{A.10}
$$

for the four possible values of (I, J).

The correlation matrix in this basis is thus

$$
\begin{aligned}
&\langle U(t)|\chi^\dagger_{Ik}\chi_{Jk'} |U(t)\rangle = \\
&\delta_{kk'} \begin{pmatrix} \sin^2\theta_k & \sin\theta_k\cos\theta_k e^{it\epsilon_k} \\ \sin\theta_k\cos\theta_k e^{-it\epsilon_k} & \cos^2\theta_k \end{pmatrix}.
\end{aligned}
\tag{A.11}
$$

The correlation matrix in real space, which we need for the calculation of the entanglement entropy, is given by

$$
\begin{aligned}
&\langle U(t)| \chi^\dagger_{Ix}\chi_{Jx'} |U(t)\rangle \\
&= \sum_k V^*_{xk} \begin{pmatrix} \sin^2\theta_k & \sin\theta_k\cos\theta_k e^{it\epsilon_k} \\ \sin\theta_k\cos\theta_k e^{-it\epsilon_k} & \cos^2\theta_k \end{pmatrix} V^t_{kx'},
\end{aligned}
\tag{A.12}
$$

where a general position space Hamiltonian can be diagonalized through the unitary matrix as,

$$
\begin{aligned}
\hat{H} = \sum_{x,y}\chi^\dagger_x H_{xy}\chi_y &= \sum_{x,y} \underbrace{\chi^\dagger_x V_{xk}}_{\chi^\dagger_k} \underbrace{D_{kq}}_{\epsilon_k\delta_{kq}} \underbrace{V^\dagger_{qy}\chi_y}_{\chi_q} \\
&= \sum_k \epsilon_k \chi^\dagger_k\chi_k,
\end{aligned}
\tag{A.13}
$$

Finally, the Von Neumann entropy is given by

$$S(t) = -\sum_{n} \left[\xi_n(t) \ln \xi_n(t) + (1 - \xi_n(t)) \ln(1 - \xi_n(t))\right], \tag{A.14}$$

where $\xi_k(t)$ are the eigenvalues of the correlation matrix truncated to the entries corresponding to degrees of freedom in our subsystem.

APPENDIX B

QUASI-PARTICLES FOR THE RANDOM SINGLET PHASE

The early time entanglement entropy growth for a quantum quench into the random singlet phase (RSP) is depicted in Fig. 3.7. Qualitatively, we see an initial linear growth, followed by what appears to be a power law growth, which eventually settles to a very slow, sub-logarithmic growth at long times. In order to obtain an analytical estimate for the entanglement dynamics, we use the quasi-particle picture that is applicable to integrable systems [130, 132, 188, 189]. The master formula is

$$S(t) \propto t \int_{|v(\varepsilon)|t<\ell} d\varepsilon v(\varepsilon) f(\varepsilon) + \ell \int_{|v(\varepsilon)|t>\ell} d\varepsilon f(\varepsilon), \tag{B.1}$$

where ℓ is the length of the interval, $v(\varepsilon)$ is the velocity of the quasi-particles at energy ε and $f(\varepsilon)$ is the entanglement production rate of quasi-particles. In other words, $f(\varepsilon)$ is the extent to which each mode contributes to the entanglement entropy. For this function, we can use the entropy of each occupied fermionic mode

$$f(\varepsilon) = -(1 - n(\varepsilon)) \log(1 - n(\varepsilon)) - n(\varepsilon) \log n(\varepsilon), \tag{B.2}$$

where $n(\varepsilon)$ is the occupation number of each mode after the quench. We use the Fermi-Dirac distribution

$$n(\varepsilon) = \frac{1}{1 + e^{\beta_{\mathit{eff}} \varepsilon}}, \tag{B.3}$$

which provides an excellent approximation. Here, β_{eff} is an effective inverse temperature, determined by the energy of the initial state.

Using the density of states for the SDRG fixed point, $\rho(\varepsilon)$ [190], we can compute the velocity of the associated quasi-particles

$$\rho(\varepsilon) = \frac{\rho_0}{\varepsilon |\log \varepsilon|^3} \quad \rightarrow \quad v(\varepsilon) = \frac{\varepsilon |\log \varepsilon|^3}{\rho_0}. \tag{B.4}$$

The above density of states is quite unusual, though we have verified it numerically, reassuring us that we are closely approximating the infinite disorder fixed point. It displays a concentration of low energy "slow" modes between $\varepsilon = 0$ and $\varepsilon = 1$. These may be responsible for the long-time growth of entanglement entropy. It should be emphasized, however, that the above density of states comes from the fixed point of a real space RG procedure, and is only expected to be valid asymptotically as $\varepsilon \to 0$. Using the standard form for the semiclassical particle velocity, $v(\varepsilon) = d\varepsilon(k)/dk\big|_{k(\varepsilon)}$, which we have done, is also not exactly correct, since the eigenstates of the disordered model are not labeled by momentum k. Disorder averaging, however, restores approximate translational symmetry, and the above form of the quasi-particle velocities yields results consistent with numerics. Combining the ingredients from (B.1)-(B.4), we obtain the integral

$$\begin{aligned} S(t) \propto \frac{t}{\rho_0} & \left[\int_{|v(\varepsilon)|t<\ell} d\varepsilon \varepsilon |\log \varepsilon|^3 + \ell \int_{|v(\varepsilon)|t>\ell} d\varepsilon \right] \\ & \times \left[\log(1+e^{\beta\varepsilon}) - \frac{\beta\varepsilon e^{\beta\varepsilon}}{1+e^{\beta\varepsilon}} \right] \end{aligned} \tag{B.5}$$

To second order in β, the first integral is

$$\frac{t}{\rho_0} \int_{|v(\varepsilon)|t<\ell} d\varepsilon \varepsilon |\log \varepsilon|^3 \left(\log 2 - \frac{\varepsilon^2 \beta^2}{8} + \mathcal{O}(\beta^4) \right) \tag{B.6}$$

which is much easier to deal with. To determine the integration bounds, we solve

$$v(\varepsilon)t = \frac{\varepsilon |\log \varepsilon|^3 t}{\rho_0} = \ell \tag{B.7}$$

for $\varepsilon > 0$. Because $v(\varepsilon)$ does not increase monotonically with ε, there are multiple branches to the solution: $\exp\left[3W_{-1}\left(\frac{-1}{3}\sqrt[3]{\frac{\ell}{t}}\right)\right]$, $\exp\left[3W\left(\frac{-1}{3}\sqrt[3]{\frac{\ell}{t}}\right)\right]$, and $\exp\left[3W\left(\frac{1}{3}\sqrt[3]{\frac{\ell}{t}}\right)\right]$, where $W_k(x)$ is the k^{th} branch of the product log or Lambert W-function, and $W(x)$ is the principal branch of the product log function. The first two solutions are only valid (real) for $t > t^* = \frac{e^3\ell}{27}$, while the third is valid for all $t > 0$. Thus, t^* is the time at which the slow modes begin to contribute to the entanglement growth. This set of slow modes makes the dynamics of the RSP markedly different than that of free fermions.

The second term in (B.5) can be integrated exactly. Taking into account, once again, the multiple domains of integration, and imposing an energy cutoff ϵ (which also functions as a velocity cutoff), we obtain a very complicated and unenlightening expression for the entanglement entropy, which we omit for brevity, and which we have used to fit the numerical data in Fig. 3.7.

REFERENCES

[1] Román Orús. A practical introduction to tensor networks: Matrix product states and projected entangled pair states. *Annals of Physics*, 349:117–158, October 2014. doi: 10.1016/j.aop.2014.06.013.

[2] Laimei Nie, Masahiro Nozaki, Shinsei Ryu, and Mao Tian Tan. Signature of quantum chaos in operator entanglement in 2d CFTs. *Journal of Statistical Mechanics: Theory and Experiment*, 9(9):093107, September 2019. doi: 10.1088/1742-5468/ab3a29.

[3] Klaus Mølmer and Anders Sørensen. Multiparticle Entanglement of Hot Trapped Ions. *Phys. Rev. Lett.*, 82(9):1835–1838, March 1999. doi: 10.1103/PhysRevLett.82.1835.

[4] Andrew W. Cross, Lev S. Bishop, John A. Smolin, and Jay M. Gambetta. Open Quantum Assembly Language. *arXiv e-prints*, art. arXiv:1707.03429, July 2017.

[5] Alexei Kitaev and John Preskill. Topological Entanglement Entropy. *Phys. Rev. Lett.*, 96 (11):110404, March 2006. doi: 10.1103/PhysRevLett.96.110404.

[6] Michael Levin and Xiao-Gang Wen. Detecting Topological Order in a Ground State Wave Function. *Phys. Rev. Lett.*, 96(11):110405, March 2006. doi: 10.1103/PhysRevLett.96.110405.

[7] S. Sachdev. *Quantum phase transitions*. Cambridge University Press, Cambridge, second ed. edition, 2011. ISBN 9780521514682.

[8] Ken Shiozaki, Hassan Shapourian, Kiyonori Gomi, and Shinsei Ryu. Many-body topological invariants for fermionic short-range entangled topological phases protected by antiunitary symmetries. *Phys. Rev. B*, 98(3):035151, July 2018. doi: 10.1103/PhysRevB.98.035151.

[9] J. Eisert, M. Friesdorf, and C. Gogolin. Quantum many-body systems out of equilibrium. *Nature Physics*, 11(2):124–130, February 2015. doi: 10.1038/nphys3215.

[10] O. Aharony, S. S. Gubser, J. Maldacena, H. Ooguri, and Y. Oz. Large N field theories, string theory and gravity. *Physics Reports*, 323:183–386, January 2000. doi: 10.1016/S0370-1573(99)00083-6.

[11] S. Ryu and T. Takayanagi. Holographic Derivation of Entanglement Entropy from the anti de Sitter Space/Conformal Field Theory Correspondence. *Physical Review Letters*, 96(18): 181602, May 2006. doi: 10.1103/PhysRevLett.96.181602.

[12] S. Ryu and T. Takayanagi. Aspects of holographic entanglement entropy. *Journal of High Energy Physics*, 8:045, August 2006. doi: 10.1088/1126-6708/2006/08/045.

[13] D. Perez-Garcia, F. Verstraete, M. M. Wolf, and J. I. Cirac. Matrix Product State Representations. *arXiv e-prints*, art. quant-ph/0608197, August 2006.

[14] F. Verstraete and J. I. Cirac. Renormalization algorithms for Quantum-Many Body Systems in two and higher dimensions. *arXiv e-prints*, art. cond-mat/0407066, July 2004.

[15] G. Evenbly and G. Vidal. Algorithms for entanglement renormalization. *Phys. Rev. B*, 79 (14):144108, April 2009. doi: 10.1103/PhysRevB.79.144108.

[16] Michael A. Nielsen and Isaac L. Chuang. *Quantum Computation and Quantum Information: 10th Anniversary Edition*. Cambridge University Press, New York, NY, USA, 10th edition, 2011. ISBN 1107002176, 9781107002173.

[17] Michael M. Wolf, Frank Verstraete, Matthew B. Hastings, and J. Ignacio Cirac. Area Laws in Quantum Systems: Mutual Information and Correlations. *Phys. Rev. Lett.*, 100(7):070502, February 2008. doi: 10.1103/PhysRevLett.100.070502.

[18] Berry Groisman, Sandu Popescu, and Andreas Winter. Quantum, classical, and total amount of correlations in a quantum state. *Phys. Rev. A*, 72(3):032317, September 2005. doi: 10.1103/PhysRevA.72.032317.

[19] Paweł Horodecki. Separability criterion and inseparable mixed states with positive partial transposition. *Physics Letters A*, 232(5):333–339, February 1997. doi: 10.1016/S0375-9601(97)00416-7.

[20] Asher Peres. Separability Criterion for Density Matrices. *Phys. Rev. Lett.*, 77(8):1413–1415, August 1996. doi: 10.1103/PhysRevLett.77.1413.

[21] Ingemar Bengtsson and Karol Zyczkowski. A brief introduction to multipartite entanglement. *arXiv e-prints*, art. arXiv:1612.07747, December 2016.

[22] W. Dür, G. Vidal, and J. I. Cirac. Three qubits can be entangled in two inequivalent ways. *Phys. Rev. A*, 62(6):062314, December 2000. doi: 10.1103/PhysRevA.62.062314.

[23] Jonah Kudler-Flam, Masahiro Nozaki, Shinsei Ryu, and Mao Tian Tan. Quantum vs. classical information: operator negativity as a probe of scrambling. *Journal of High Energy Physics*, 2020(1):31, Jan 2020. doi: 10.1007/JHEP01(2020)031.

[24] Philippe Di Francesco, Pierre Mathieu, and David Sénéchal. *Conformal field theory*. Graduate texts in contemporary physics. Springer, New York, NY, 1997. doi: 10.1007/978-1-4612-2256-9. URL `https://cds.cern.ch/record/639405`.

[25] Veronika E. Hubeny. The AdS/CFT correspondence. *Classical and Quantum Gravity*, 32(12):124010, June 2015. doi: 10.1088/0264-9381/32/12/124010.

[26] Tatsuma Nishioka, Shinsei Ryu, and Tadashi Takayanagi. Holographic entanglement entropy: an overview. *Journal of Physics A Mathematical General*, 42(50):504008, December 2009. doi: 10.1088/1751-8113/42/50/504008.

[27] Jonah Kudler-Flam, Ian MacCormack, and Shinsei Ryu. Holographic entanglement contour, bit threads, and the entanglement tsunami. *Journal of Physics A Mathematical General*, 52(32):325401, August 2019. doi: 10.1088/1751-8121/ab2dae.

[28] G. Vitagliano, A. Riera, and J. I. Latorre. Volume-law scaling for the entanglement entropy in spin-1/2 chains. *New Journal of Physics*, 12(11):113049, November 2010. doi: 10.1088/1367-2630/12/11/113049.

[29] G. Ramírez, J. Rodríguez-Laguna, and G. Sierra. From conformal to volume law for the entanglement entropy in exponentially deformed critical spin 1/2 chains. *Journal of Statistical Mechanics: Theory and Experiment*, 10:10004, October 2014. doi: 10.1088/1742-5468/2014/10/P10004.

[30] G. Ramírez, J. Rodríguez-Laguna, and G. Sierra. Entanglement over the rainbow. *Journal of Statistical Mechanics: Theory and Experiment*, 6:06002, June 2015. doi: 10.1088/1742-5468/2015/06/P06002.

[31] Javier Rodríguez-Laguna, Jérôme Dubail, Giovanni Ramírez, Pasquale Calabrese, and Germán Sierra. More on the rainbow chain: entanglement, space-time geometry and thermal states. *Journal of Physics A Mathematical General*, 50(16):164001, Apr 2017. doi: 10.1088/1751-8121/aa6268.

[32] Vincenzo Alba, Silvia N. Santalla, Paola Ruggiero, Javier Rodriguez-Laguna, Pasquale Calabrese, and German Sierra. Unusual area-law violation in random inhomogeneous systems. *Journal of Statistical Mechanics: Theory and Experiment*, 2:023105, Feb 2019. doi: 10.1088/1742-5468/ab02df.

[33] E. Tonni, J. Rodríguez-Laguna, and G. Sierra. Entanglement hamiltonian and entanglement contour in inhomogeneous 1D critical systems. *Journal of Statistical Mechanics: Theory and Experiment*, 4:043105, April 2018. doi: 10.1088/1742-5468/aab67d.

[34] Chandan Dasgupta and Shang-keng Ma. Low-temperature properties of the random heisenberg antiferromagnetic chain. *Phys. Rev. B*, 22:1305–1319, Aug 1980. doi: 10.1103/PhysRevB.22.1305. URL `https://link.aps.org/doi/10.1103/PhysRevB.22.1305`.

[35] A. Gendiar, R. Krcmar, and T. Nishino. Spherical Deformation for One-Dimensional Quantum Systems. *Progress of Theoretical Physics*, 122:953–967, October 2009. doi: 10.1143/PTP.122.953.

[36] T. Hikihara and T. Nishino. Connecting distant ends of one-dimensional critical systems by a sine-square deformation. *Phys. Rev. B*, 83(6):060414, February 2011. doi: 10.1103/PhysRevB.83.060414.

[37] A. Gendiar, M. Daniška, Y. Lee, and T. Nishino. Suppression of finite-size effects in one-dimensional correlated systems. *Phys. Rev. A*, 83(5):052118, May 2011. doi: 10.1103/PhysRevA.83.052118.

[38] N. Shibata and C. Hotta. Boundary effects in the density-matrix renormalization group calculation. *Phys. Rev. B*, 84(11):115116, September 2011. doi: 10.1103/PhysRevB.84.115116.

[39] I. Maruyama, H. Katsura, and T. Hikihara. Sine-square deformation of free fermion systems in one and higher dimensions. *Phys. Rev. B*, 84(16):165132, October 2011. doi: 10.1103/PhysRevB.84.165132.

[40] H. Katsura. Exact ground state of the sine-square deformed XY spin chain. *Journal of Physics A Mathematical General*, 44(25):252001, June 2011. doi: 10.1088/1751-8113/44/25/252001.

[41] H. Katsura. Sine-square deformation of solvable spin chains and conformal field theories. *Journal of Physics A Mathematical General*, 45(11):115003, March 2012. doi: 10.1088/1751-8113/45/11/115003.

[42] C. Hotta and N. Shibata. Grand canonical finite-size numerical approaches: A route to measuring bulk properties in an applied field. *Phys. Rev. B*, 86(4):041108, July 2012. doi: 10.1103/PhysRevB.86.041108.

[43] K. Okunishi and H. Katsura. Sine-square deformation and supersymmetric quantum mechanics. *Journal of Physics A Mathematical General*, 48:445208, November 2015. doi: 10.1088/1751-8113/48/44/445208.

[44] T. Tada. Sine-square deformation and its relevance to string theory. *Modern Physics Letters A*, 30:1550092, May 2015. doi: 10.1142/s0217732315500923.

[45] N. Ishibashi and T. Tada. Infinite circumference limit of conformal field theory. *Journal of Physics A Mathematical General*, 48:315402, August 2015. doi: 10.1088/1751-8113/48/31/315402.

[46] Kouichi Okunishi. Sine-square deformation and Mobius quantization of two-dimensional conformal field theory. *arXiv e-prints*, art. arXiv:1603.09543, Mar 2016.

[47] N. Ishibashi and T. Tada. Dipolar quantization and the infinite circumference limit of two-dimensional conformal field theories. *International Journal of Modern Physics A*, 31:1650170, November 2016. doi: 10.1142/S0217751X16501700.

[48] X. Wen, S. Ryu, and A. W. W. Ludwig. Evolution operators in conformal field theories and conformal mappings: Entanglement Hamiltonian, the sine-square deformation, and others. *Phys. Rev. B*, 93(23):235119, June 2016. doi: 10.1103/PhysRevB.93.235119.

[49] Shota Tamura and Hosho Katsura. Zero-energy states in conformal field theory with sine-square deformation. *arXiv e-prints*, art. arXiv:1709.06238, Sep 2017.

[50] X. Wen and J.-Q. Wu. Quantum dynamics in sine-square deformed conformal field theory: Quench from uniform to nonuniform conformal field theory. *Phys. Rev. B*, 97(18):184309, May 2018. doi: 10.1103/PhysRevB.97.184309.

[51] Xueda Wen and Jie-Qiang Wu. Floquet conformal field theory. *arXiv e-prints*, art. arXiv:1805.00031, Apr 2018.

[52] T. Tada. Conformal quantum mechanics and sine-square deformation. *Progress of Theoretical and Experimental Physics*, 2018(6):061B01, June 2018. doi: 10.1093/ptep/pty058.

[53] Peter D. Hislop and Roberto Longo. Modular structure of the local algebras associated with the free massless scalar field theory. *Communications in Mathematical Physics*, 84(1):71–85, 1982. doi: 10.1007/bf01208372.

[54] I. Peschel. On the entanglement entropy for an XY spin chain. *Journal of Statistical Mechanics: Theory and Experiment*, 12:12005, December 2004. doi: 10.1088/1742-5468/2004/12/P12005.

[55] J. Cardy and E. Tonni. Entanglement Hamiltonians in two-dimensional conformal field theory. *Journal of Statistical Mechanics: Theory and Experiment*, 12:123103, December 2016. doi: 10.1088/1742-5468/2016/12/123103.

[56] Jerome Dubail, Jean-Marie Stéphan, Jacopo Viti, and Pasquale Calabrese. Conformal field theory for inhomogeneous one-dimensional quantum systems: the example of non-interacting Fermi gases. *SciPost Physics*, 2(1):002, Feb 2017. doi: 10.21468/SciPostPhys.2.1.002.

[57] Sara Murciano, Paola Ruggiero, and Pasquale Calabrese. Entanglement and relative entropies for low-lying excited states in inhomogeneous one-dimensional quantum systems. *Journal of Statistical Mechanics: Theory and Experiment*, 3:034001, Mar 2019. doi: 10.1088/1742-5468/ab00ec.

[58] Hiroshi Ueda, Andrej Gendiar, Valentin Zauner, Takatsugu Iharagi, and Tomotoshi Nishino. Transverse Field Ising Model Under Hyperbolic Deformation. *arXiv e-prints*, art. arXiv:1008.3458, Aug 2010.

[59] H. Ueda, H. Nakano, K. Kusakabe, and T. Nishino. Scaling Relation for Excitation Energy under Hyperbolic Deformation. *Progress of Theoretical Physics*, 124:389–398, September 2010. doi: 10.1143/PTP.124.389.

[60] T. Iharagi, A. Gendiar, H. Ueda, and T. Nishino. Phase Transition of the Ising Model on a Hyperbolic Lattice. *Journal of the Physical Society of Japan*, 79(10):104001–104001, October 2010. doi: 10.1143/JPSJ.79.104001.

[61] Edwin Langmann and Per Moosavi. Diffusive Heat Waves in Random Conformal Field Theory. *Phys. Rev. Lett.*, 122(2):020201, Jan 2019. doi: 10.1103/PhysRevLett.122.020201.

[62] Jerome Dubail, Jean-Marie Stéphan, and Pasquale Calabrese. Emergence of curved light-cones in a class of inhomogeneous Luttinger liquids. *SciPost Physics*, 3:019, Sep 2017. doi: 10.21468/SciPostPhys.3.3.019.

[63] O. Aharony, D. Marolf, and M. Rangamani. Conformal field theories in anti-de Sitter space. *Journal of High Energy Physics*, 2:41, February 2011. doi: 10.1007/JHEP02(2011)041.

[64] K. Jensen, A. Karch, and B. Robinson. Holographic dual of a Hawking pair has a wormhole. *Phys. Rev. D*, 90(6):064019, September 2014. doi: 10.1103/PhysRevD.90.064019.

[65] T. Andrade and C. F. Uhlemann. Beyond the unitarity bound in AdS/CFT$_{(A)dS}$. *Journal of High Energy Physics*, 1:123, January 2012. doi: 10.1007/JHEP01(2012)123.

[66] K. Skenderis and S. N. Solodukhin. Quantum effective action from the AdS/CFT correspondence. *Physics Letters B*, 472:316–322, January 2000. doi: 10.1016/S0370-2693(99)01467-7.

[67] Maulik Parikh and Prasant Samantray. Rindler-AdS/CFT. *Journal of High Energy Physics*, 2018(10):129, Oct 2018. doi: 10.1007/JHEP10(2018)129.

[68] Borun D. Chowdhury and Maulik K. Parikh. When UV and IR Collide: Inequivalent CFTs From Different Foliations Of AdS. *arXiv e-prints*, art. arXiv:1407.4467, Jul 2014.

[69] S. Deser and O. Levin. LETTER TO THE EDITOR: Equivalence of Hawking and Unruh temperatures and entropies through flat space embeddings. *Classical and Quantum Gravity*, 15:L85–L87, December 1998. doi: 10.1088/0264-9381/15/12/002.

[70] E. Cáceres, M. Chernicoff, A. Güijosa, and J. F. Pedraza. Quantum Fluctuations and the Unruh effect in strongly-coupled conformal field theories. *Journal of High Energy Physics*, 6: 78, June 2010. doi: 10.1007/JHEP06(2010)078.

[71] H. Casini, M. Huerta, and R. C. Myers. Towards a derivation of holographic entanglement entropy. *Journal of High Energy Physics*, 5:36, May 2011. doi: 10.1007/JHEP05(2011)036.

[72] T. Hirayama, P.-W. Kao, S. Kawamoto, and F.-L. Lin. Unruh effect and holography. *Nuclear Physics B*, 844:1–25, March 2011. doi: 10.1016/j.nuclphysb.2010.10.018.

[73] T. Takayanagi. Holographic Dual of a Boundary Conformal Field Theory. *Physical Review Letters*, 107(10):101602, September 2011. doi: 10.1103/PhysRevLett.107.101602.

[74] M. Fujita, T. Takayanagi, and E. Tonni. Aspects of AdS/BCFT. *Journal of High Energy Physics*, 11:43, November 2011. doi: 10.1007/JHEP11(2011)043.

[75] Máximo Bañados. Three-dimensional quantum geometry and black holes. In Horacio Falomir, Ricardo E. Gamboa Saravi, and Fidel A. Schaposnik, editors, *Trends in Theoretical Physics II*, volume 484 of *American Institute of Physics Conference Series*, pages 147–169, July 1999. doi: 10.1063/1.59661.

[76] M. M. Roberts. Time evolution of entanglement entropy from a pulse. *Journal of High Energy Physics*, 12:27, December 2012. doi: 10.1007/JHEP12(2012)027.

[77] G. Mandal, R. Sinha, and N. Sorokhaibam. The inside outs of $\mathrm{AdS}_3/\mathrm{CFT}_2$: exact AdS wormholes with entangled CFT duals. *Journal of High Energy Physics*, 1:36, January 2015. doi: 10.1007/JHEP01(2015)036.

[78] Mario Flory and Nina Miekley. Complexity change under conformal transformations in $\mathrm{AdS}_3/\mathrm{CFT}_2$. *Journal of High Energy Physics*, 2019(5):3, May 2019. doi: 10.1007/JHEP05(2019)003.

[79] D. Anninos, J. Samani, and E. Shaghoulian. Warped entanglement entropy. *Journal of High Energy Physics*, 2:118, February 2014. doi: 10.1007/JHEP02(2014)118.

[80] Veronika E. Hubeny, Mukund Rangamani, and Tadashi Takayanagi. A covariant holographic entanglement entropy proposal. *Journal of High Energy Physics*, 2007:062, July 2007. doi: 10.1088/1126-6708/2007/07/062.

[81] M. M. Sheikh-Jabbari and H. Yavartanoo. Excitation entanglement entropy in two dimensional conformal field theories. *Phys. Rev. D*, 94(12):126006, December 2016. doi: 10.1103/PhysRevD.94.126006.

[82] N. Tetradis. Entropy from $\mathrm{AdS}_3/\mathrm{CFT}_2$. *Journal of High Energy Physics*, 2:54, February 2012. doi: 10.1007/JHEP02(2012)054.

[83] Yannis Brun and Jerome Dubail. One-particle density matrix of trapped one-dimensional impenetrable bosons from conformal invariance. *SciPost Physics*, 2:012, Apr 2017. doi: 10.21468/SciPostPhys.2.2.012.

[84] A. Colcelli, J. Viti, G. Mussardo, and A. Trombettoni. Universal off-diagonal long-range-order behavior for a trapped Tonks-Girardeau gas. *Phys. Rev. A*, 98(6):063633, Dec 2018. doi: 10.1103/PhysRevA.98.063633.

[85] G. Vidal, J. I. Latorre, E. Rico, and A. Kitaev. Entanglement in Quantum Critical Phenomena. *Phys. Rev. Lett.*, 90:227902, June 2003. doi: 10.1103/PhysRevLett.90.227902.

[86] Mark van Raamsdonk. Building up spacetime with quantum entanglement. *General Relativity and Gravitation*, 42:2323–2329, October 2010. doi: 10.1007/s10714-010-1034-0.

[87] Yangang Chen and Guifre Vidal. Entanglement contour. *Journal of Statistical Mechanics: Theory and Experiment*, 2014(10):10011, Oct 2014. doi: 10.1088/1742-5468/2014/10/P10011.

[88] Alonso Botero and Benni Reznik. Spatial structures and localization of vacuum entanglement in the linear harmonic chain. *Phys. Rev. A*, 70(5):052329, Nov 2004. doi: 10.1103/PhysRevA.70.052329.

[89] Andrea Coser, Cristiano De Nobili, and Erik Tonni. A contour for the entanglement entropies in harmonic lattices. *Journal of Physics A Mathematical General*, 50(31):314001, Aug 2017. doi: 10.1088/1751-8121/aa7902.

[90] Qiang Wen. Fine structure in holographic entanglement and entanglement contour. *arXiv e-prints*, art. arXiv:1803.05552, Mar 2018.

[91] V. Alba, S. N. Santalla, P. Ruggiero, J. Rodriguez-Laguna, P. Calabrese, and G. Sierra. Unusual area-law violation in random inhomogeneous systems. *ArXiv e-prints*, July 2018.

[92] M. Freedman and M. Headrick. Bit Threads and Holographic Entanglement. *Communications in Mathematical Physics*, 352:407–438, May 2017. doi: 10.1007/s00220-016-2796-3.

[93] H. Liu and S. J. Suh. Entanglement Tsunami: Universal Scaling in Holographic Thermalization. *Physical Review Letters*, 112(1):011601, January 2014. doi: 10.1103/PhysRevLett.112.011601.

[94] Hong Liu and S. Josephine Suh. Entanglement growth during thermalization in holographic systems. *Phys. Rev. D*, 89:066012, March 2014. doi: 10.1103/PhysRevD.89.066012.

[95] Horacio Casini, Hong Liu, and Márk Mezei. Spread of entanglement and causality. *Journal of High Energy Physics*, 2016:77, July 2016. doi: 10.1007/JHEP07(2016)077.

[96] Stefan Leichenauer and Mudassir Moosa. Entanglement tsunami in (1 +1)-dimensions. *Phys. Rev. D*, 92:126004, December 2015. doi: 10.1103/PhysRevD.92.126004.

[97] Jonah Kudler-Flam, Ian MacCormack, and Shinsei Ryu. Holographic entanglement contour, bit threads, and the entanglement tsunami. *Journal of Physics A: Mathematical and Theoretical*, 52(32):arXiv:1902.04654, Jul 2019. doi: 10.1088/1751-8121/ab2dae. URL `https://doi.org/10.1088%2F1751-8121%2Fab2dae`.

[98] Ian MacCormack, Mao Tian Tan, Jonah Kudler-Flam, and Shinsei Ryu. Operator and entanglement growth in non-thermalizing systems: many-body localization and the random singlet phase. *arXiv e-prints*, art. arXiv:2001.08222, January 2020.

[99] Huzihiro Araki and Elliott H. Lieb. Entropy inequalities. *Comm. Math. Phys.*, 18(2):160–170, 1970. URL `https://projecteuclid.org:443/euclid.cmp/1103842506`.

[100] Qiang Wen. Towards the generalized gravitational entropy for spacetimes with non- Lorentz invariant duals. *ArXiv e-prints*, art. arXiv:1810.11756, October 2018.

[101] Geoffrey Compère, Wei Song, and Andrew Strominger. New boundary conditions for AdS$_3$. *Journal of High Energy Physics*, 2013:152, May 2013. doi: 10.1007/JHEP05(2013)152.

[102] T. Azeyanagi, T. Takayanagi, A. Karch, and E. G. Thompson. Holographic calculation of boundary entropy. *Journal of High Energy Physics*, 3:054, March 2008. doi: 10.1088/1126-6708/2008/03/054.

[103] A. L. Fitzpatrick, J. Kaplan, and M. T. Walters. Universality of long-distance AdS physics from the CFT bootstrap. *Journal of High Energy Physics*, 8:145, August 2014. doi: 10.1007/JHEP08(2014)145.

[104] C. T. Asplund, A. Bernamonti, F. Galli, and T. Hartman. Holographic entanglement entropy from 2d CFT: heavy states and local quenches. *Journal of High Energy Physics*, 2:171, February 2015. doi: 10.1007/JHEP02(2015)171.

[105] Pawel Caputa, Joan Simón, Andrius Štikonas, and Tadashi Takayanagi. Quantum entanglement of localized excited states at finite temperature. *Journal of High Energy Physics*, 2015: 102, Jan 2015. doi: 10.1007/JHEP01(2015)102.

[106] Mark Srednicki. Chaos and quantum thermalization. *Phys. Rev. E*, 50:888–901, Aug 1994. doi: 10.1103/PhysRevE.50.888. URL `https://link.aps.org/doi/10.1103/PhysRevE.50.888`.

[107] C. J. Turner, A. A. Michailidis, D. A. Abanin, M. Serbyn, and Z. Papić. Weak ergodicity breaking from quantum many-body scars. *Nature Physics*, 14:745–749, May 2018. doi: 10.1038/s41567-018-0137-5.

[108] Tarun Grover, Ari M. Turner, and Ashvin Vishwanath. Entanglement entropy of gapped phases and topological order in three dimensions. *Physical Review B*, 84:195120, November 2011. doi: 10.1103/PhysRevB.84.195120.

[109] C. A. Agón, J. de Boer, and J. F. Pedraza. Geometric Aspects of Holographic Bit Threads. *ArXiv e-prints*, November 2018.

[110] Daniel L. Jafferis and S. Josephine Suh. The Gravity Duals of Modular Hamiltonians. *ArXiv e-prints*, art. arXiv:1412.8465, December 2014.

[111] J. Kudler-Flam and S. Ryu. Entanglement negativity and minimal entanglement wedge cross sections in holographic theories. *ArXiv e-prints*, August 2018.

[112] C. De Nobili. On entanglement negativity in 1 + 1 and 2 + 1 dimensional quantum systems. October 2016.

[113] Jonah Kudler-Flam, Hassan Shapourian, and Shinsei Ryu. The negativity contour: a quasi-local measure of entanglement for mixed states. *SciPost Physics*, 8(4):063, April 2020. doi: 10.21468/SciPostPhys.8.4.063.

[114] T. Takayanagi and K. Umemoto. Holographic Entanglement of Purification. *ArXiv e-prints*, August 2017.

[115] A. Bhattacharyya, T. Takayanagi, and K. Umemoto. Entanglement of purification in free scalar field theories. *Journal of High Energy Physics*, 4:132, April 2018. doi: 10.1007/JHEP04(2018)132.

[116] P. Nguyen, T. Devakul, M. G. Halbasch, M. P. Zaletel, and B. Swingle. Entanglement of purification: from spin chains to holography. *Journal of High Energy Physics*, 1:98, January 2018. doi: 10.1007/JHEP01(2018)098.

[117] K. Umemoto and Y. Zhou. Entanglement of Purification for Multipartite States and its Holographic Dual. *ArXiv e-prints*, May 2018.

[118] N. Bao and I. F. Halpern. Holographic inequalities and entanglement of purification. *Journal of High Energy Physics*, 3:6, March 2018. doi: 10.1007/JHEP03(2018)006.

[119] H. Hirai, K. Tamaoka, and T. Yokoya. Towards entanglement of purification for conformal field theories. *Progress of Theoretical and Experimental Physics*, 2018(6):063B03, June 2018. doi: 10.1093/ptep/pty063.

[120] Y. Nomura, P. Rath, and N. Salzetta. Pulling the boundary into the bulk. *Phys. Rev. D*, 98 (2):026010, July 2018. doi: 10.1103/PhysRevD.98.026010.

[121] N. Bao and I. F. Halpern. Conditional and Multipartite Entanglements of Purification and Holography. *ArXiv e-prints*, May 2018.

[122] R. Espíndola, A. Guijosa, and J. F. Pedraza. Entanglement Wedge Reconstruction and Entanglement of Purification. *ArXiv e-prints*, April 2018.

[123] Pawel Caputa, Masamichi Miyaji, Tadashi Takayanagi, and Koji Umemoto. Holographic Entanglement of Purification from Conformal Field Theories. *arXiv e-prints*, art. arXiv:1812.05268, December 2018.

[124] Kotaro Tamaoka. Entanglement Wedge Cross Section from the Dual Density Matrix. *Phys. Rev. Lett.*, 122(14):141601, Apr 2019. doi: 10.1103/PhysRevLett.122.141601.

[125] Bartłomiej Czech, Lampros Lamprou, Samuel McCandlish, and James Sully. Integral geometry and holography. *Journal of High Energy Physics*, 2015:175, October 2015. doi: 10.1007/JHEP10(2015)175.

[126] Bartlomiej Czech, Lampros Lamprou, Samuel McCandlish, and James Sully. Tensor networks from kinematic space. *Journal of High Energy Physics*, 2016:100, July 2016. doi: 10.1007/JHEP07(2016)100.

[127] Masahiro Nozaki, Tokiro Numasawa, and Tadashi Takayanagi. Holographic local quenches and entanglement density. *Journal of High Energy Physics*, 2013:80, May 2013. doi: 10.1007/JHEP05(2013)080.

[128] Chong-Bin Chen, Fu-Wen Shu, and Meng-He Wu. Quantum bit threads of MERA tensor network in large c limit. *arXiv e-prints*, art. arXiv:1804.00441, April 2018.

[129] Tomonori Ugajin. Two dimensional quantum quenches and holography. *arXiv e-prints*, art. arXiv:1311.2562, Nov 2013.

[130] Pasquale Calabrese and John Cardy. Time Dependence of Correlation Functions Following a Quantum Quench. *Phys. Rev. Lett.*, 96(13):136801, April 2006. doi: 10.1103/PhysRevLett.96.136801.

[131] Pasquale Calabrese and John Cardy. Entanglement and correlation functions following a local quench: a conformal field theory approach. *Journal of Statistical Mechanics: Theory and Experiment*, 2007:10004, October 2007. doi: 10.1088/1742-5468/2007/10/P10004.

[132] Pasquale Calabrese and John Cardy. Evolution of entanglement entropy in one-dimensional systems. *Journal of Statistical Mechanics: Theory and Experiment*, 2005(4):04010, Apr 2005. doi: 10.1088/1742-5468/2005/04/P04010.

[133] M. Nozaki, T. Numasawa, A. Prudenziati, and T. Takayanagi. Dynamics of entanglement entropy from Einstein equation. *Phys. Rev. D*, 88(2):026012, July 2013. doi: 10.1103/PhysRevD.88.026012.

[134] Adam Nahum, Jonathan Ruhman, Sagar Vijay, and Jeongwan Haah. Quantum Entanglement Growth under Random Unitary Dynamics. *Physical Review X*, 7:031016, July 2017. doi: 10.1103/PhysRevX.7.031016.

[135] Adam Nahum, Sagar Vijay, and Jeongwan Haah. Operator Spreading in Random Unitary Circuits. *Physical Review X*, 8:021014, April 2018. doi: 10.1103/PhysRevX.8.021014.

[136] C. W. von Keyserlingk, Tibor Rakovszky, Frank Pollmann, and S. L. Sondhi. Operator Hydrodynamics, OTOCs, and Entanglement Growth in Systems without Conservation Laws. *Physical Review X*, 8(2):021013, Apr 2018. doi: 10.1103/PhysRevX.8.021013.

[137] Cheryne Jonay, David A. Huse, and Adam Nahum. Coarse-grained dynamics of operator and state entanglement. *arXiv e-prints*, art. arXiv:1803.00089, February 2018.

[138] Dmitry A. Abanin and Zlatko Papić. Recent progress in many-body localization. *Annalen der Physik*, 529(7):1700169, Jul 2017. doi: 10.1002/andp.201700169.

[139] Maksym Serbyn, Z. Papić, and Dmitry A. Abanin. Local Conservation Laws and the Structure of the Many-Body Localized States. *Phys. Rev. Lett.*, 111(12):127201, Sep 2013. doi: 10.1103/PhysRevLett.111.127201.

[140] David A. Huse, Rahul Nandkishore, and Vadim Oganesyan. Phenomenology of fully many-body-localized systems. *arXiv e-prints*, art. arXiv:1408.4297, Aug 2014.

[141] J. Smith, A. Lee, P. Richerme, B. Neyenhuis, P. W. Hess, P. Hauke, M. Heyl, D. A. Huse, and C. Monroe. Many-body localization in a quantum simulator with programmable random disorder. *Nature Physics*, 12(10):907–911, Oct 2016. doi: 10.1038/nphys3783.

[142] Rajibul Islam, Ruichao Ma, Philipp M. Preiss, M. Eric Tai, Alexander Lukin, Matthew Rispoli, and Markus Greiner. Measuring entanglement entropy through the interference of quantum many-body twins. *arXiv e-prints*, art. arXiv:1509.01160, Sep 2015.

[143] Alexander Lukin, Matthew Rispoli, Robert Schittko, M. Eric Tai, Adam M. Kaufman, Soonwon Choi, Vedika Khemani, Julian Léonard, and Markus Greiner. Probing entanglement in a many-body-localized system. *Science*, 364(6437):256–260, Apr 2019. doi: 10.1126/science.aau0818.

[144] Marko Žnidarič, Tomaž Prosen, and Peter Prelovšek. Many-body localization in the Heisenberg XXZ magnet in a random field. *Phys. Rev. B*, 77(6):064426, Feb 2008. doi: 10.1103/PhysRevB.77.064426.

[145] Jens H. Bardarson, Frank Pollmann, and Joel E. Moore. Unbounded Growth of Entanglement in Models of Many-Body Localization. *Phys. Rev. Lett.*, 109:017202, Jul 2012. doi: 10.1103/PhysRevLett.109.017202.

[146] Xiao Chen, Tianci Zhou, David A. Huse, and Eduardo Fradkin. Out-of-time-order correlations in many-body localized and thermal phases. *Annalen der Physik*, 529(7):1600332, Jul 2017. doi: 10.1002/andp.201600332.

[147] Brian Swingle and Debanjan Chowdhury. Slow scrambling in disordered quantum systems. *Phys. Rev. B*, 95(6):060201, Feb 2017. doi: 10.1103/PhysRevB.95.060201.

[148] Rahul Nandkishore and David A. Huse. Many-Body Localization and Thermalization in Quantum Statistical Mechanics. *Annual Review of Condensed Matter Physics*, 6:15–38, Mar 2015. doi: 10.1146/annurev-conmatphys-031214-014726.

[149] Yichen Huang, Yong-Liang Zhang, and Xie Chen. Out-of-time-ordered correlators in many-body localized systems. *Annalen der Physik*, 529:1600318, Jul 2017. doi: 10.1002/andp.201600318.

[150] Yu Chen. Universal Logarithmic Scrambling in Many Body Localization. *arXiv e-prints*, art. arXiv:1608.02765, Aug 2016.

[151] Daniel S. Fisher. Random antiferromagnetic quantum spin chains. *Phys. Rev. B*, 50:3799–3821, Aug 1994. doi: 10.1103/PhysRevB.50.3799. URL `https://link.aps.org/doi/10.1103/PhysRevB.50.3799`.

[152] G. Refael and J. E. Moore. Entanglement Entropy of Random Quantum Critical Points in One Dimension. *Physical Review Letters*, 93(26):260602, Dec 2004. doi: 10.1103/PhysRevLett.93.260602.

[153] Nicolas Laflorencie. Scaling of entanglement entropy in the random singlet phase. *Physical Review B*, 72:140408, Oct 2005. doi: 10.1103/PhysRevB.72.140408.

[154] G. Refael and J. E. Moore. Criticality and entanglement in random quantum systems. *Journal of Physics A Mathematical General*, 42(50):504010, Dec 2009. doi: 10.1088/1751-8113/42/50/504010.

[155] Maurizio Fagotti, Pasquale Calabrese, and Joel E. Moore. Entanglement spectrum of random-singlet quantum critical points. *Phys. Rev. B*, 83(4):045110, Jan 2011. doi: 10.1103/PhysRevB.83.045110.

[156] R. Vasseur, A. C. Potter, and S. A. Parameswaran. Quantum criticality of hot random spin chains. *Phys. Rev. Lett.*, 114:217201, May 2015. doi: 10.1103/PhysRevLett.114.217201. URL `https://link.aps.org/doi/10.1103/PhysRevLett.114.217201`.

[157] Romain Vasseur, Aaron J. Friedman, S. A. Parameswaran, and Andrew C. Potter. Particle-hole symmetry, many-body localization, and topological edge modes. *Phys. Rev. B*, 93:134207, Apr 2016. doi: 10.1103/PhysRevB.93.134207. URL `https://link.aps.org/doi/10.1103/PhysRevB.93.134207`.

[158] Giuseppe De Tomasi, Daniele Trapin, Markus Heyl, and Soumya Bera. Anomalous diffusion in particle-hole symmetric many-body localized systems. *arXiv e-prints*, art. arXiv:2001.04996, Jan 2020.

[159] Ferenc Iglói, Zsolt Szatmári, and Yu-Cheng Lin. Entanglement entropy dynamics of disordered quantum spin chains. *Phys. Rev. B*, 85(9):094417, Mar 2012. doi: 10.1103/PhysRevB.85.094417.

[160] Olexei Motrunich, Kedar Damle, and David A. Huse. Dynamics and transport in random quantum systems governed by strong-randomness fixed points. *Phys. Rev. B*, 63:134424, Mar 2001. doi: 10.1103/PhysRevB.63.134424. URL `https://link.aps.org/doi/10.1103/PhysRevB.63.134424`.

[161] Y. Zhao, F. Andraschko, and J. Sirker. Entanglement entropy of disordered quantum chains following a global quench. *Phys. Rev. B*, 93(20):205146, May 2016. doi: 10.1103/PhysRevB.93.205146.

[162] Jonathan Harper, Matthew Headrick, and Andrew Rolph. Bit Threads in Higher Curvature Gravity. *arXiv e-prints*, art. arXiv:1807.04294, July 2018.

[163] Paolo Zanardi. Entanglement of quantum evolutions. *Phys. Rev. A*, 63(4):040304, Apr 2001. doi: 10.1103/PhysRevA.63.040304.

[164] Man-Duen Choi. Completely positive linear maps on complex matrices. *Linear Algebra and its Applications*, 10(3):285 – 290, 1975. ISSN 0024-3795. doi: https://doi.org/10.1016/0024-3795(75)90075-0. URL `http://www.sciencedirect.com/science/article/pii/0024379575900750`.

[165] A. Jamiolkowski. Linear transformations which preserve trace and positive semidefiniteness of operators. *Reports on Mathematical Physics*, 3(4):275 – 278, 1972. ISSN 0034-4877. doi: https://doi.org/10.1016/0034-4877(72)90011-0. URL `http://www.sciencedirect.com/science/article/pii/0034487772900110`.

[166] Pavan Hosur, Xiao-Liang Qi, Daniel A. Roberts, and Beni Yoshida. Chaos in quantum channels. *Journal of High Energy Physics*, 2016:4, Feb 2016. doi: 10.1007/JHEP02(2016)004.

[167] Jonah Kudler-Flam, Laimei Nie, and Shinsei Ryu. Conformal field theory and the web of quantum chaos diagnostics. *Journal of High Energy Physics*, 2020(1):175, Jan 2020. doi: 10.1007/JHEP01(2020)175.

[168] Tianci Zhou and David J. Luitz. Operator entanglement entropy of the time evolution operator in chaotic systems. *Phys. Rev. B*, 95(9):094206, Mar 2017. doi: 10.1103/PhysRevB.95.094206.

[169] Johnnie Gray, Abolfazl Bayat, Arijeet Pal, and Sougato Bose. Scale Invariant Entanglement Negativity at the Many-Body Localization Transition. *arXiv e-prints*, art. arXiv:1908.02761, August 2019.

[170] John Preskill. Quantum Computing in the NISQ era and beyond. *arXiv e-prints*, art. arXiv:1801.00862, January 2018.

[171] Jingxiang Wu and Timothy H. Hsieh. Variational Thermal Quantum Simulation via Thermofield Double States. *Phys. Rev. Lett.*, 123(22):220502, November 2019. doi: 10.1103/PhysRevLett.123.220502.

[172] Ian MacCormack, Alexey Galda, and Adam L. Lyon. Simulating Large PEPs Tensor Networks on Small Quantum Devices. *arXiv e-prints*, art. arXiv:2110.00507, October 2021.

[173] J. M. Pino, J. M. Dreiling, C. Figgatt, J. P. Gaebler, S. A. Moses, M. S. Allman, C. H. Baldwin, M. Foss-Feig, D. Hayes, K. Mayer, C. Ryan-Anderson, and B. Neyenhuis. Demonstration of the trapped-ion quantum CCD computer architecture. *Nature Physics*, 592(7853): 209–213, January 2021. doi: 10.1038/s41586-021-03318-4.

[174] Michael Foss-Feig, David Hayes, Joan M. Dreiling, Caroline Figgatt, John P. Gaebler, Steven A. Moses, Juan M. Pino, and Andrew C. Potter. Holographic quantum algorithms for simulating correlated spin systems. *Physical Review Research*, 3(3):033002, July 2021. doi: 10.1103/PhysRevResearch.3.033002.

[175] Michael Foss-Feig, Stephen Ragole, Andrew Potter, Joan Dreiling, Caroline Figgatt, John Gaebler, Alex Hall, Steven Moses, Juan Pino, Ben Spaun, Brian Neyenhuis, and David Hayes. Entanglement from tensor networks on a trapped-ion QCCD quantum computer. *arXiv e-prints*, art. arXiv:2104.11235, April 2021.

[176] Eli Chertkov, Justin Bohnet, David Francois, John Gaebler, Dan Gresh, Aaron Hankin, Kenny Lee, Ra'anan Tobey, David Hayes, Brian Neyenhuis, Russell Stutz, Andrew C. Potter, and Michael Foss-Feig. Holographic dynamics simulations with a trapped ion quantum computer. *arXiv e-prints*, art. arXiv:2105.09324, May 2021.

[177] Jonas Haferkamp, Dominik Hangleiter, Jens Eisert, and Marek Gluza. Contracting projected entangled pair states is average-case hard. *Phys. Rev. Research*, 2:013010, Jan 2020. doi: 10.1103/PhysRevResearch.2.013010. URL `https://link.aps.org/doi/10.1103/PhysRevResearch.2.013010`.

[178] C. Ryan-Anderson, J. G. Bohnet, K. Lee, D. Gresh, A. Hankin, J. P. Gaebler, D. Francois, A. Chernoguzov, D. Lucchetti, N. C. Brown, T. M. Gatterman, S. K. Halit, K. Gilmore, J. Gerber, B. Neyenhuis, D. Hayes, and R. P. Stutz. Realization of real-time fault-tolerant quantum error correction. *arXiv e-prints*, art. arXiv:2107.07505, July 2021.

[179] Lucas Slattery and Bryan K. Clark. Quantum Circuits For Two-Dimensional Isometric Tensor Networks. *arXiv e-prints*, art. arXiv:2108.02792, August 2021.

[180] Xiao-Gang Wen. Quantum order from string-net condensations and the origin of light and massless fermions. *Phys. Rev. D*, 68(6):065003, September 2003. doi: 10.1103/PhysRevD.68.065003.

[181] Jing Yu, Xing-Hai Zhang, and Su-Peng Kou. Majorana edge states for Z_2 topological orders of the Wen plaquette and toric code models. *Phys. Rev. B*, 87(18):184402, May 2013. doi: 10.1103/PhysRevB.87.184402.

[182] Klaus Mølmer and Anders Sørensen. Multiparticle entanglement of hot trapped ions. *Phys. Rev. Lett.*, 82:1835–1838, Mar 1999. doi: 10.1103/PhysRevLett.82.1835. URL `https://link.aps.org/doi/10.1103/PhysRevLett.82.1835`.

[183] Steven G. Johnson. *The NLopt nonlinear-optimization package*, 2011. URL `http://ab-initio.mit.edu/nlopt`.

[184] M. J. D. Powell. *A Direct Search Optimization Method That Models the Objective and Constraint Functions by Linear Interpolation*, pages 51–67. Springer Netherlands, Dordrecht, 1994. ISBN 978-94-015-8330-5. doi: 10.1007/978-94-015-8330-5_4. URL `https://doi.org/10.1007/978-94-015-8330-5_4`.

[185] Michael P. Zaletel and Frank Pollmann. Isometric Tensor Network States in Two Dimensions. *Phys. Rev. Lett.*, 124(3):037201, January 2020. doi: 10.1103/PhysRevLett.124.037201.

[186] C. Spee, J. I. de Vicente, and B. Kraus. The maximally entangled set of 4-qubit states. *Journal of Mathematical Physics*, 57(5):052201, May 2016. doi: 10.1063/1.4946895.

[187] H. J. Briegel, D. E. Browne, W. Dür, R. Raussendorf, and M. Van den Nest. Measurement-based quantum computation. *arXiv e-prints*, art. arXiv:0910.1116, October 2009.

[188] Vincenzo Alba and Pasquale Calabrese. Entanglement and thermodynamics after a quantum quench in integrable systems. *Proceedings of the National Academy of Science*, 114(30): 7947–7951, July 2017. doi: 10.1073/pnas.1703516114.

[189] Vincenzo Alba and Pasquale Calabrese. Entanglement dynamics after quantum quenches in generic integrable systems. *SciPost Physics*, 4(3):017, March 2018. doi: 10.21468/SciPostPhys.4.3.017.

[190] Freeman J. Dyson. The dynamics of a disordered linear chain. *Phys. Rev.*, 92:1331–1338, Dec 1953. doi: 10.1103/PhysRev.92.1331. URL `https://link.aps.org/doi/10.1103/PhysRev.92.1331`.

[191] Rachel Zuckerman Sarango, Saul, Stefan Elrington Earnest-Noble, Nate, Jay Gambetta Kawase, Kei, Ivano Tavernelli Barkoutsos, and Panagiotis. Ibm's roadmap for scaling quantum technology, Feb 2021. URL `https://research.ibm.com/blog/ibm-quantum-roadmap`.

[192] Kishor Bharti, Alba Cervera-Lierta, Thi Ha Kyaw, Tobias Haug, Sumner Alperin-Lea, Abhinav Anand, Matthias Degroote, Hermanni Heimonen, Jakob S. Kottmann, Tim Menke, Wai-Keong Mok, Sukin Sim, Leong-Chuan Kwek, and Alán Aspuru-Guzik. Noisy intermediate-scale quantum (NISQ) algorithms. *arXiv e-prints*, art. arXiv:2101.08448, January 2021.

[193] Richard P Feynman. Simulating physics with computers. *International journal of theoretical physics*, 21(6/7):467–488, 1982.

[194] Román Orús. Tensor networks for complex quantum systems. *Nature Reviews Physics*, 1(9): 538–550, August 2019. doi: 10.1038/s42254-019-0086-7.

[195] U. Schollwöck. The density-matrix renormalization group. *Reviews of Modern Physics*, 77 (1):259–315, January 2005. doi: 10.1103/RevModPhys.77.259.

[196] Ulrich Schollwöck. The density-matrix renormalization group in the age of matrix product states. *Annals of Physics*, 326(1):96–192, January 2011. doi: 10.1016/j.aop.2010.09.012.

[197] William Huggins, Piyush Patil, Bradley Mitchell, K. Birgitta Whaley, and E. Miles Stoudenmire. Towards quantum machine learning with tensor networks. *Quantum Science and Technology*, 4(2):024001, April 2019. doi: 10.1088/2058-9565/aaea94.

[198] Hassan Shapourian, Ken Shiozaki, and Shinsei Ryu. Partial time-reversal transformation and entanglement negativity in fermionic systems. *Phys. Rev. B*, 95(16):165101, April 2017. doi: 10.1103/PhysRevB.95.165101.

[199] Ruihua Fan, Yingfei Gu, Ashvin Vishwanath, and Xueda Wen. Emergent Spatial Structure and Entanglement Localization in Floquet Conformal Field Theory. *arXiv e-prints*, art. arXiv:1908.05289, Aug 2019.

[200] Nicolas Macé, Nicolas Laflorencie, and Fabien Alet. Many-body localization in a quasiperiodic Fibonacci chain. *SciPost Physics*, 6(4):050, Apr 2019. doi: 10.21468/SciPostPhys.6.4.050.

[201] Yaodong Li, Xiao Chen, and Matthew P. A. Fisher. Quantum Zeno effect and the many-body entanglement transition. *Phys. Rev. B*, 98(20):205136, Nov 2018. doi: 10.1103/PhysRevB.98.205136.

[202] Chao-Ming Jian, Yi-Zhuang You, Romain Vasseur, and Andreas W. W. Ludwig. Measurement-induced criticality in random quantum circuits. *arXiv e-prints*, art. arXiv:1908.08051, Aug 2019.

[203] S. Aubry and Gilles André. Analyticity breaking and anderson localization in incommensurate lattices. 1980.

[204] Thomas Hartman and Juan Maldacena. Time evolution of entanglement entropy from black hole interiors. *Journal of High Energy Physics*, 2013:14, May 2013. doi: 10.1007/JHEP05(2013)014.

[205] Jonathon Riddell and Erik S. Sørensen. Out-of-time ordered correlators and entanglement growth in the random-field XX spin chain. *Phys. Rev. B*, 99(5):054205, Feb 2019. doi: 10.1103/PhysRevB.99.054205.

[206] Adam Nahum, Jonathan Ruhman, and David A. Huse. Dynamics of entanglement and transport in one-dimensional systems with quenched randomness. *Phys. Rev. B*, 98(3):035118, Jul 2018. doi: 10.1103/PhysRevB.98.035118.

[207] Subhayan Sahu, Shenglong Xu, and Brian Swingle. Scrambling dynamics across a thermalization-localization quantum phase transition. *arXiv e-prints*, art. arXiv:1807.06086, Jul 2018.

[208] A. I. Larkin and Yu. N. Ovchinnikov. Quasiclassical Method in the Theory of Superconductivity. *Soviet Journal of Experimental and Theoretical Physics*, 28:1200, Jun 1969.

[209] Marcos Rigol, Vanja Dunjko, and Maxim Olshanii. Thermalization and its mechanism for generic isolated quantum systems. *Nature Physics*, 452(7189):854–858, Apr 2008. doi: 10.1038/nature06838.

[210] Qiang Wen. Entanglement contour from subset entanglement entropies. *arXiv e-prints*, art. arXiv:1902.06905, Feb 2019.

[211] Qiang Wen. Formulas for partial entanglement entropy. *Physical Review Research*, 2(2): 023170, May 2020. doi: 10.1103/PhysRevResearch.2.023170.

[212] Eric Mascot, Masahiro Nozaki, and Masaki Tezuka. Local Operator Entanglement in Spin Chains. *arXiv e-prints*, art. arXiv:2012.14609, December 2020.

[213] Brian Skinner, Jonathan Ruhman, and Adam Nahum. Measurement-Induced Phase Transitions in the Dynamics of Entanglement. *Physical Review X*, 9(3):031009, Jul 2019. doi: 10.1103/PhysRevX.9.031009.

[214] Ruihua Fan, Pengfei Zhang, Huitao Shen, and Hui Zhai. Out-of-Time-Order Correlation for Many-Body Localization. *arXiv e-prints*, art. arXiv:1608.01914, Aug 2016.

[215] Vedika Khemani, Ashvin Vishwanath, and David A. Huse. Operator Spreading and the Emergence of Dissipative Hydrodynamics under Unitary Evolution with Conservation Laws. *Physical Review X*, 8(3):031057, Jul 2018. doi: 10.1103/PhysRevX.8.031057.

[216] I. V. Protopopov, R. K. Panda, T. Parolini, A. Scardicchio, E. Demler, and D. A. Abanin. Non-Abelian symmetries and disorder: a broad non-ergodic regime and anomalous thermalization. *arXiv e-prints*, art. arXiv:1902.09236, Feb 2019.

[217] E. Westerberg, A. Furusaki, M. Sigrist, and P. A. Lee. Low-energy fixed points of random quantum spin chains. *Phys. Rev. B*, 55:12578–12593, May 1997. doi: 10.1103/PhysRevB.55.12578. URL `https://link.aps.org/doi/10.1103/PhysRevB.55.12578`.

[218] Yimu Bao, Soonwon Choi, and Ehud Altman. Theory of the Phase Transition in Random Unitary Circuits with Measurements. *arXiv e-prints*, art. arXiv:1908.04305, Aug 2019.

[219] Achilleas Lazarides, Arnab Das, and Roderich Moessner. Periodic Thermodynamics of Isolated Quantum Systems. *Phys. Rev. Lett.*, 112(15):150401, Apr 2014. doi: 10.1103/PhysRevLett.112.150401.

[220] Shenglong Xu, Xiao Li, Yi-Ting Hsu, Brian Swingle, and Sankar Das Sarma. Butterfly effect in interacting Aubry-Andre model: thermalization, slow scrambling, and many-body localization. *arXiv e-prints*, art. arXiv:1902.07199, Feb 2019.

[221] Tiff Brydges, Andreas Elben, Petar Jurcevic, Benoît Vermersch, Christine Maier, Ben P. Lanyon, Peter Zoller, Rainer Blatt, and Christian F. Roos. Probing Rényi entanglement entropy via randomized measurements. *Science*, 364(6437):260–263, Apr 2019. doi: 10.1126/science.aau4963.

[222] P. Roushan, C. Neill, J. Tangpanitanon, V. M. Bastidas, A. Megrant, R. Barends, Y. Chen, Z. Chen, B. Chiaro, A. Dunsworth, A. Fowler, B. Foxen, M. Giustina, E. Jeffrey, J. Kelly, E. Lucero, J. Mutus, M. Neeley, C. Quintana, D. Sank, A. Vainsencher, J. Wenner, T. White, H. Neven, D. G. Angelakis, and J. Martinis. Spectral signatures of many-body localization with interacting photons. *arXiv e-prints*, art. arXiv:1709.07108, Sep 2017.

[223] Michael Schreiber, Sean S. Hodgman, Pranjal Bordia, Henrik P. Lüschen, Mark H. Fischer, Ronen Vosk, Ehud Altman, Ulrich Schneider, and Immanuel Bloch. Observation of many-body localization of interacting fermions in a quasirandom optical lattice. *Science*, 349(6250): 842–845, Aug 2015. doi: 10.1126/science.aaa7432.

[224] Josiah Couch, Stefan Eccles, Phuc Nguyen, Brian Swingle, and Shenglong Xu. The Speed of Quantum Information Spreading in Chaotic Systems. *arXiv e-prints*, art. arXiv:1908.06993, Aug 2019.

[225] Arpan Bhattacharyya, Wissam Chemissany, S. Shajidul Haque, and Bin Yan. Towards the Web of Quantum Chaos Diagnostics. *arXiv e-prints*, art. arXiv:1909.01894, Sep 2019.

[226] Pak Hang Chris Lau, Chen-Te Ma, Jeff Murugan, and Masaki Tezuka. Randomness and chaos in qubit models. *Physics Letters B*, 795:230–235, Aug 2019. doi: 10.1016/j.physletb.2019.05.052.

[227] Xhek Turkeshi, Paola Ruggiero, and Pasquale Calabrese. Negativity Spectrum in the Random Singlet Phase. *arXiv e-prints*, art. arXiv:1910.09571, Oct 2019.

[228] Giuseppe De Tomasi, Soumya Bera, Jens H. Bardarson, and Frank Pollmann. Quantum Mutual Information as a Probe for Many-Body Localization. *Phys. Rev. Lett.*, 118(1):016804, Jan 2017. doi: 10.1103/PhysRevLett.118.016804.

[229] Colin G. West and Tzu-Chieh Wei. Global and short-range entanglement properties in excited, many-body localized spin chains. *arXiv e-prints*, art. arXiv:1809.04689, Sep 2018.

[230] Paweł Caputa and Marek M. Rams. Quantum dimensions from local operator excitations in the Ising model. *Journal of Physics A Mathematical General*, 50(5):055002, Feb 2017. doi: 10.1088/1751-8121/aa5202.

[231] Yasuhiro Sekino and L. Susskind. Fast scramblers. *Journal of High Energy Physics*, 2008 (10):065, Oct 2008. doi: 10.1088/1126-6708/2008/10/065.

[232] Juan Maldacena, Stephen H. Shenker, and Douglas Stanford. A bound on chaos. *Journal of High Energy Physics*, 2016(8):106, Aug 2016. doi: 10.1007/JHEP08(2016)106.

[233] Andrea Coser, Erik Tonni, and Pasquale Calabrese. Entanglement negativity after a global quantum quench. *Journal of Statistical Mechanics: Theory and Experiment*, 2014(12):12017, Dec 2014. doi: 10.1088/1742-5468/2014/12/P12017.

[234] Paola Ruggiero, Vincenzo Alba, and Pasquale Calabrese. Entanglement negativity in random spin chains. *Phys. Rev. B*, 94(3):035152, Jul 2016. doi: 10.1103/PhysRevB.94.035152.

[235] Yuya O. Nakagawa, Masataka Watanabe, Hiroyuki Fujita, and Sho Sugiura. Universality in volume-law entanglement of scrambled pure quantum states. *Nature Communications*, 9: 1635, Apr 2018. doi: 10.1038/s41467-018-03883-9.

[236] Sergey Bravyi, David Fattal, and Daniel Gottesman. GHZ extraction yield for multipartite stabilizer states. *Journal of Mathematical Physics*, 47(6):062106, Jun 2006. doi: 10.1063/1.2203431.

[237] Daniel A. Roberts and Brian Swingle. Lieb-Robinson and the butterfly effect. *arXiv e-prints*, art. arXiv:1603.09298, Mar 2016.

[238] Luca D'Alessio, Yariv Kafri, Anatoli Polkovnikov, and Marcos Rigol. From quantum chaos and eigenstate thermalization to statistical mechanics and thermodynamics. *Advances in Physics*, 65(3):239–362, May 2016. doi: 10.1080/00018732.2016.1198134.

[239] John Z. Imbrie, Valentina Ros, and Antonello Scardicchio. Local integrals of motion in many-body localized systems. *Annalen der Physik*, 529(7):1600278, Jul 2017. doi: 10.1002/andp.201600278.

[240] Toma ž Prosen and Iztok Pižorn. Operator space entanglement entropy in a transverse ising chain. *Phys. Rev. A*, 76:032316, Sep 2007. doi: 10.1103/PhysRevA.76.032316. URL `https://link.aps.org/doi/10.1103/PhysRevA.76.032316`.

[241] Leon Balents and Matthew P. A. Fisher. Delocalization transition via supersymmetry in one dimension. *Phys. Rev. B*, 56(20):12970–12991, Nov 1997. doi: 10.1103/PhysRevB.56.12970.

[242] Sandra Byju, Kinjalk Lochan, and S. Shankaranarayanan. Generalized thermalization in quenched free Fermionic models. *arXiv e-prints*, art. arXiv:1808.07742, Aug 2018.

[243] Maksym Serbyn, Z. Papić, and Dmitry A. Abanin. Universal Slow Growth of Entanglement in Interacting Strongly Disordered Systems. *Phys. Rev. Lett.*, 110(26):260601, Jun 2013. doi: 10.1103/PhysRevLett.110.260601.

[244] Daniel A. Roberts and Douglas Stanford. Diagnosing Chaos Using Four-Point Functions in Two-Dimensional Conformal Field Theory. *Phys. Rev. Lett.*, 115(13):131603, Sep 2015. doi: 10.1103/PhysRevLett.115.131603.

[245] Stephen H. Shenker and Douglas Stanford. Black holes and the butterfly effect. *Journal of High Energy Physics*, 2014:67, Mar 2014. doi: 10.1007/JHEP03(2014)067.

[246] Maksym Serbyn, Alexios A. Michailidis, Dmitry A. Abanin, and Z. Papić. Power-law entanglement spectrum in many-body localized phases. *Phys. Rev. Lett.*, 117:160601, Oct 2016. doi: 10.1103/PhysRevLett.117.160601. URL `https://link.aps.org/doi/10.1103/PhysRevLett.117.160601`.

[247] D. M. Kennes and C. Karrasch. Entanglement scaling of excited states in large one-dimensional many-body localized systems. *Phys. Rev. B*, 93:245129, Jun 2016. doi: 10.1103/PhysRevB.93.245129. URL `https://link.aps.org/doi/10.1103/PhysRevB.93.245129`.

[248] Vedika Khemani, Frank Pollmann, and S. L. Sondhi. Obtaining highly excited eigenstates of many-body localized hamiltonians by the density matrix renormalization group approach. *Phys. Rev. Lett.*, 116:247204, Jun 2016. doi: 10.1103/PhysRevLett.116.247204. URL `https://link.aps.org/doi/10.1103/PhysRevLett.116.247204`.

[249] S. P. Lim and D. N. Sheng. Many-body localization and transition by density matrix renormalization group and exact diagonalization studies. *Phys. Rev. B*, 94:045111, Jul 2016. doi: 10.1103/PhysRevB.94.045111. URL `https://link.aps.org/doi/10.1103/PhysRevB.94.045111`.

[250] Cheng-Ju Lin and Olexei I. Motrunich. Out-of-time-ordered correlators in a quantum Ising chain. *Phys. Rev. B*, 97(14):144304, Apr 2018. doi: 10.1103/PhysRevB.97.144304.

[251] Gabriele DeChiara, Simone Montangero, Pasquale Calabrese, and Rosario Fazio. Entanglement entropy dynamics of Heisenberg chains. *Journal of Statistical Mechanics: Theory and Experiment*, 2006(3):03001, Mar 2006. doi: 10.1088/1742-5468/2006/03/P03001.

[252] Max McGinley, Andreas Nunnenkamp, and Johannes Knolle. Slow growth of out-of-time-order correlators and entanglement in integrable disordered systems. *arXiv e-prints*, art. arXiv:1807.06039, Jul 2018.

[253] John Cardy. Thermalization and Revivals after a Quantum Quench in Conformal Field Theory. *Physical Review Letters*, 112(22):220401, Jun 2014. doi: 10.1103/PhysRevLett.112.220401.

[254] Elliott H. Lieb and Derek W. Robinson. The finite group velocity of quantum spin systems. *Comm. Math. Phys.*, 28(3):251–257, 1972. URL `https://projecteuclid.org:443/euclid.cmp/1103858407`.

[255] J. M. Deutsch. Quantum statistical mechanics in a closed system. *Phys. Rev. A*, 43:2046–2049, Feb 1991. doi: 10.1103/PhysRevA.43.2046. URL `https://link.aps.org/doi/10.1103/PhysRevA.43.2046`.

[256] Mark Srednicki. Chaos and quantum thermalization. *Phys. Rev. E*, 50(2):888–901, Aug 1994. doi: 10.1103/PhysRevE.50.888.

[257] Gautam Mandal, Ritam Sinha, and Tomonori Ugajin. Finite size effect on dynamical entanglement entropy: CFT and holography. *arXiv e-prints*, art. arXiv:1604.07830, Apr 2016.

[258] Xiongjie Yu, David Pekker, and Bryan K. Clark. Finding matrix product state representations of highly excited eigenstates of many-body localized hamiltonians. *Phys. Rev. Lett.*, 118: 017201, Jan 2017. doi: 10.1103/PhysRevLett.118.017201. URL `https://link.aps.org/doi/10.1103/PhysRevLett.118.017201`.

[259] J. Z. Imbrie. On Many-Body Localization for Quantum Spin Chains. *Journal of Statistical Physics*, 163:998–1048, June 2016. doi: 10.1007/s10955-016-1508-x.

[260] Giuseppe Di Giulio, Raul Arias, and Erik Tonni. Entanglement hamiltonians in 1D free lattice models after a global quantum quench. *arXiv e-prints*, art. arXiv:1905.01144, May 2019.

[261] Ian Mondragon-Shem, Taylor L. Hughes, Juntao Song, and Emil Prodan. Topological Criticality in the Chiral-Symmetric AIII Class at Strong Disorder. *Phys. Rev. Lett.*, 113(4):046802, Jul 2014. doi: 10.1103/PhysRevLett.113.046802.

[262] Jiahui Bao and Cheng-Yong Zhang. Out-of-time-order correlators in one-dimensional xy model. *arXiv preprint arXiv:1901.09327*, 2019.

[263] Iztok Pižorn and Toma ž Prosen. Operator space entanglement entropy in xy spin chains. *Phys. Rev. B*, 79:184416, May 2009. doi: 10.1103/PhysRevB.79.184416. URL `https://link.aps.org/doi/10.1103/PhysRevB.79.184416`.

[264] J Dubail. Entanglement scaling of operators: a conformal field theory approach, with a glimpse of simulability of long-time dynamics in 1+1d. *Journal of Physics A: Mathematical and Theoretical*, 50(23):234001, may 2017. doi: 10.1088/1751-8121/aa6f38. URL `https://doi.org/10.1088%2F1751-8121%2Faa6f38`.

[265] V. Alba, J. Dubail, and M. Medenjak. Operator entanglement in interacting integrable quantum systems: The case of the rule 54 chain. *Phys. Rev. Lett.*, 122:250603, Jun 2019. doi: 10.1103/PhysRevLett.122.250603. URL `https://link.aps.org/doi/10.1103/PhysRevLett.122.250603`.

[266] Huajia Wang and Tianci Zhou. Barrier from chaos: operator entanglement dynamics of the reduced density matrix. *Journal of High Energy Physics*, 2019(12):20, Dec 2019. ISSN 1029-8479. doi: 10.1007/JHEP12(2019)020. URL `https://doi.org/10.1007/JHEP12(2019)020`.

[267] Shenglong Xu and Brian Swingle. Accessing scrambling using matrix product operators. *Nature Physics*, 2019. ISSN 1745-2481. doi: 10.1038/s41567-019-0712-4. URL `https://doi.org/10.1038/s41567-019-0712-4`.

[268] Christopher J. Turner, Alexios A. Michailidis, Dmitry A. Abanin, Maksym Serbyn, and Zlatko Papic. Quantum many-body scars. *arXiv e-prints*, art. arXiv:1711.03528, November 2017.

[269] William Donnelly and Laurent Freidel. Local subsystems in gauge theory and gravity. *Journal of High Energy Physics*, 2016:102, September 2016. doi: 10.1007/JHEP09(2016)102.

[270] X. Huang and F.-L. Lin. Entanglement renormalization and integral geometry. *Journal of High Energy Physics*, 12:81, December 2015. doi: 10.1007/JHEP12(2015)081.

[271] Luca Bombelli, Rabinder K. Koul, Joohan Lee, and Rafael D. Sorkin. A Quantum Source of Entropy for Black Holes. *Phys. Rev.*, D34:373–383, 1986. doi: 10.1103/PhysRevD.34.373.

[272] E. Witten. Notes on Some Entanglement Properties of Quantum Field Theory. *ArXiv e-prints*, March 2018.

[273] J. Maldacena. Eternal black holes in anti-de Sitter. *Journal of High Energy Physics*, 4:021, April 2003. doi: 10.1088/1126-6708/2003/04/021.

[274] I. MacCormack, A. Liu, M. Nozaki, and S. Ryu. Holographic Duals of Inhomogeneous Systems: The Rainbow Chain and the Sine-Square Deformation Model. *In Preparation*, December 2018.

[275] A. B. Zamolodchikov. Conformal symmetry in two-dimensional space: Recursion representation of conformal block. *Theoretical and Mathematical Physics*, 73:1088–1093, October 1987. doi: 10.1007/BF01022967.

[276] Curtis T. Asplund and Alice Bernamonti. Mutual information after a local quench in conformal field theory. *Phys. Rev. D*, 89:066015, March 2014. doi: 10.1103/PhysRevD.89.066015.

[277] Pasquale Calabrese and John Cardy. Quantum quenches in 1 + 1 dimensional conformal field theories. *Journal of Statistical Mechanics: Theory and Experiment*, 6:064003, June 2016. doi: 10.1088/1742-5468/2016/06/064003.

[278] J. Kudler-Flam, I. MacCormack, M. Nozaki, and S. Ryu. Holographic negativity as a probe of thermality and scrambling in inhomogeneous systems and quantum quenches. *In Preparation*, December 2018.

[279] Matthew Headrick and Tadashi Takayanagi. Holographic proof of the strong subadditivity of entanglement entropy. *Phys. Rev. D*, 76:106013, November 2007. doi: 10.1103/PhysRevD.76.106013.

[280] Vijay Balasubramanian, Borun D. Chowdhury, Bartłomiej Czech, Jan de Boer, and Michal P. Heller. Bulk curves from boundary data in holography. *Phys. Rev. D*, 89:086004, April 2014. doi: 10.1103/PhysRevD.89.086004.

[281] J. Bhattacharya, M. Nozaki, T. Takayanagi, and T. Ugajin. Thermodynamical Property of Entanglement Entropy for Excited States. *Physical Review Letters*, 110(9):091602, March 2013. doi: 10.1103/PhysRevLett.110.091602.

[282] V. Balasubramanian and P. Kraus. A Stress Tensor for Anti-de Sitter Gravity. *Communications in Mathematical Physics*, 208:413–428, 1999. doi: 10.1007/s002200050764.

[283] A. L. Fitzpatrick, J. Kaplan, and M. T. Walters. Virasoro conformal blocks and thermality from classical background fields. *Journal of High Energy Physics*, 11:200, November 2015. doi: 10.1007/JHEP11(2015)200.

[284] C. T. Asplund, A. Bernamonti, F. Galli, and T. Hartman. Entanglement scrambling in 2d conformal field theory. *Journal of High Energy Physics*, 9:110, September 2015. doi: 10.1007/JHEP09(2015)110.

[285] E. Witten. Anti-de Sitter Space, Thermal Phase Transition, And Confinement In Gauge Theories. *ArXiv High Energy Physics - Theory e-prints*, March 1998.

[286] Christoph Holzhey, Finn Larsen, and Frank Wilczek. Geometric and renormalized entropy in conformal field theory. *Nuclear Physics B*, 424:443–467, August 1994. doi: 10.1016/0550-3213(94)90402-2.

[287] G. Vidal and R. F. Werner. Computable measure of entanglement. *Physical Review A*, 65: 032314, March 2002. doi: 10.1103/PhysRevA.65.032314.

[288] Claude E. Shannon. A mathematical theory of communication. *Bell System Technical Journal*, 27(3):379–423, 1948.

[289] C. Fefferman and C.R. Graham. Conformal invariants. *Elie Cartan et les Mathematiques d'Aujourd'hui, Asterisque*, pages 95–116, 1985.

[290] M. Parikh and P. Samantray. Rindler-AdS/CFT. *ArXiv e-prints*, November 2012.

[291] M. Banados, C. Teitelboim, and J. Zanelli. Black hole in three-dimensional spacetime. *Physical Review Letters*, 69:1849–1851, September 1992. doi: 10.1103/PhysRevLett.69.1849.

[292] H. Li and F. D. M. Haldane. Entanglement Spectrum as a Generalization of Entanglement Entropy: Identification of Topological Order in Non-Abelian Fractional Quantum Hall Effect States. *Physical Review Letters*, 101(1):010504, July 2008. doi: 10.1103/PhysRevLett.101.010504.

[293] J. Kudler-Flam, I. MacCormack, M. Nozaki, and S. Ryu. Entanglement negativity on curved manifolds and following local and global quantum quenches. *In Preparation*, October 2018.

[294] Y. Brun and J. Dubail. One-particle density matrix of trapped one-dimensional impenetrable bosons from conformal invariance. *ArXiv e-prints*, January 2017.

[295] A. Milsted and G. Vidal. Extraction of conformal data in critical quantum spin chains using the Koo-Saleur formula. *Phys. Rev. B*, 96(24):245105, December 2017. doi: 10.1103/PhysRevB.96.245105.

[296] M. Flory and N. Miekley. Complexity change under conformal transformations in AdS_3/CFT_2. *ArXiv e-prints*, June 2018.

[297] J. Dubail, J.-M. Stéphan, and P. Calabrese. Emergence of curved light-cones in a class of inhomogeneous Luttinger liquids. *ArXiv e-prints*, May 2017.